The DIRC Particle Identification System for the BABAR Experiment

I. Adam, R. Aleksan, L. Amerman, E. Antokhin, D. Aston, P. Bailly, C. Beigbeder, M. Benkebil, P. Besson, G. Bonneaud, et al.

SLAC−PUB−10516
June 2004

The DIRC Particle Identification System for the *BABAR* Experiment

I. Adam,[1] R. Aleksan,[2] L. Amerman,[3] E. Antokhin,[4] D. Aston,[1] P. Bailly,[5] C. Beigbeder,[6] M. Benkebil,[6] P. Besson,[2] G. Bonneaud,[7] Ph. Bourgeois,[2] D. Breton,[6] H. Briand,[5] F. Brochard,[7] D. N. Brown,[3] A. Buzykaev,[4] J. Chauveau,[5] R. Cizeron,[6] J. Cohen-Tanugi,[7] M. Convery,[1] S. Dardin,[3] P. David,[5] G. De Domenico,[2] C. de la Vaissiere,[5] A. de Lesquen,[2] F. Dohou,[7] M. Doser,[1] S. Emery,[2] S. Ferrag,[7] G. Fouque,[7] A. Gaidot,[2] S. Ganzhur,[4] F. Gastaldi,[7] T. Geld,[8] J.-F. Genat,[5] P.F. Giraud,[2] L. Gosset,[2] Ph. Grenier,[7] T. Haas,[1] T. Hadig,[1] D. Hale,[9] G. Hamel de Monchenault,[2] O. Hamon,[5] B. Hartfiel,[12] C. Hast,[6] A. Hoecker,[6] M. John,[5] R. W. Kadel,[3] J. Kadyk,[3] M. Karolak,[2] H. Kawahara,[1] M. Krishnamurthy,[10,11] H. Lacker,[6] H. Lebbolo,[5] F. Le Diberder,[5] M. Legendre,[2] Ph. Leruste,[5] J. Libby,[1] G. W. London,[2] M. Long,[3] J. Lory,[5] A. Lu,[9] A.-M. Lutz,[6] G. Lynch,[3] R. Malchow,[10] J. Malcles,[5] G. Mancinelli,[8] M. McCulloch,[1] D. McShurley,[1] F. Martinez-Vidal,[5] P. Matricon,[7] B. Mayer,[2] B. T. Meadows,[8] S. Mikhailov,[4] Ll. L. Mir,[3] D. Muller,[1] J.-M. Noppe,[6] J. Ocariz,[5] I. Ofte,[8] A. Onuchin,[4] D. Oshatz,[3] G. Oxoby,[1] T. Petersen,[6] M. Pivk,[5] S. Plaszczynski,[6] W. Pope,[3] M. Pripstein,[3] J. Rasson,[3] B. N. Ratcliff,[1] R. Reif,[1] C. Renard,[7] L. Roos,[5] E. Roussot,[7] A. Salnikov,[2] X. Sarazin,[1] S. Schrenk,[7] M.-H. Schune,[6] J. Schwiening,[1] S. Sen,[6] V. Shelkov,[3] M. D. Sokoloff,[8] S. Spanier,[1,11] H. Staengle,[10] J. Stark,[5] P. Stiles,[1] R. Stone,[3] J. D. Taylor,[3] A. V. Telnov,[3] G. Therin,[5] Ch. Thiebaux,[7] V. Tocut,[6] K. Truong,[6] M.-L. Turluer,[2] A. Vallereau,[5] G. Vasileiadis,[7] G. Vasseur,[2] J. Va'vra,[1] M. Verderi,[7] D. Warner,[10] T. B. Weber,[1] T. F. Weber,[3] W. A. Wenzel,[3] R. J. Wilson,[10,*] G. Wormser,[6] A. Yarritu,[1] Ch. Yéche,[2] S. Yellin,[9] Q. Zeng,[10] B. Zhang,[5] M. Zito[2]

[1]Stanford Linear Accelerator Center, Stanford, CA 94309, USA.
[2]DAPNIA, Commissariat à l'Energie Atomique/Saclay, F-91191 Gif-sur-Yvette, France.
[3]Lawrence Berkeley National Laboratory and University of California, Berkeley, CA 94720, USA.
[4]Budker Institute of Nuclear Physics, Novosibirsk 630090, Russia.
[5]Universités Paris VI et VII, Lab de Physique Nucléaire H. E., F-75252 Paris, France.
[6]Laboratoire de l'Accélérateur Linéaire, F-91898 Orsay, France.
[7]Ecole Polytechnique, LLR, F-91128 Palaiseau, France.
[8]University of Cincinnati, Cincinnati, OH 45221, USA.
[9]University of California at Santa Barbara, Santa Barbara, CA 93106, USA.
[10]Colorado State University, Fort Collins, CO 80523, USA.
[11]University of Tennessee, Tennessee, TN 37996, USA.

A new type of ring-imaging Cherenkov detector is being used for hadronic particle identification in the *BABAR* experiment at the SLAC B Factory (PEP-II). This detector is called DIRC, an acronym for **D**etection of **I**nternally **R**eflected **C**herenkov (Light). This paper will discuss the construction, operation and performance of the *BABAR* DIRC in detail.

Contents

*Corresponding author.
Email address: wilson@lamar.colostate.edu (R. J. Wilson).

Work supported in part by the Department of Energy Contract DE−AC03−76SF00515

1. Introduction

A new type of ring-imaging Cherenkov detector is being used for hadronic particle identification in the *BABAR* experiment at the Stanford Linear Accelerator Center (SLAC) B Factory (PEP-II). This detector is called DIRC, an acronym for **D**etection of **I**nternally **R**eflected **C**herenkov (Light). This paper will discuss the construction, operation and performance of the *BABAR* DIRC in greater detail than presented in an earlier description of the *BABAR* detector [1].

The paper will first motivate the choice of the DIRC design, and its basic integration into the overall *BABAR* detector. This is followed by an overview of *BABAR* DIRC design concepts and specific features of its components before a more extensive presentation of the design, fabrication, materials, operation, and performance of all elements of the detector. In the performance section we provide a sampling of some of the important particle physics measurements that have been enhanced by this technology.

Detailed descriptions of some components of the DIRC have been published previously. These components will be presented in less detail in this

paper, accompanied by appropriate references.

1.1. Physics motivation

The PEP-II B Factory [2] is an asymmetric e^+e^- collider, with beam energies of 3.1 on 9.0 GeV, that operates at a center-of-mass energy of 10.58 GeV, the mass of the Υ(4S) resonance. This resonance decays almost exclusively to $B\overline{B}$ pairs, and provides an excellent environment for the study of B mesons and their decays.

BABAR is the detector dedicated to observing this B meson production at PEP-II, with a primary physics goal of making a systematic study of *CP* violation in the B system [3]. Clean experimental tests of *CP* violation require the ability to reconstruct the decay vertices of the B meson pairs, and to measure the time dependence of their decays. The asymmetric beam configuration in the laboratory provides a boost of $\beta\gamma = 0.56$ to the $\Upsilon(4S)$ that allows determination of the proper decay time difference from the separation of the$B$ mesons along the beam axis. Furthermore, one of the B mesons must be partially or fully reconstructed, and the other must be tagged as either a B or a $\bar{B}$ by its decay products. Both of these tasks require efficient and clean hadronic particle identification over a wide range of track momenta and polar angles.

PEP-II and *BABAR* have been running since 1999 and have produced clear evidence for *CP* violating asymmetries in B decays [4,5]. The original design luminosity of 3×10^{33} has been exceeded by a factor of three, and substantially higher luminosities are expected during the next few years.

1.2. Particle identification at *BABAR* and PEP-II

The study of *CP*-violation using hadronic final states of the $B\overline{B}$ meson system requires the ability to tag the flavor of one of the B mesons while fully reconstructing the other with high acceptance. The main flavor tag in the *BABAR* design involves charged kaons from the cascade decay $b \to c \to s$, where the s ($\overline{s}$) quark from a $\overline{B}$ (B) meson decay appears in a final state K^- (K^+) meson. The momenta of the kaons used for flavor tagging extend up to about 2 GeV/c, with most of them below 1 GeV/c. The momenta of pions from the rare two-body decay $B^0 \to \pi^+\pi^-$, associated with the measurement of the *CP* phase angle α, lie between 1.7 GeV/c and 4.2 GeV/c in the laboratory. This mode must be distinguished from $K^+\pi^-$ or K^+K^- final states. A characteristic of these events is a strong momentum-polar angle correlation: higher momenta occur at the more forward angles because of the boost of the e^+e^- system.

Since the inner drift chamber tracker can provide sufficient π/K separation up to only about 700 MeV/c, the dedicated Particle Identification (PID) system must perform well over a range from about 0.7 to 4.2 GeV/c, where the challenging upper end of this range must be achieved in the forward region of *BABAR*.

The physical placement of a PID system between the charged particle tracking detectors (drift chamber) and the electromagnetic calorimeter, shown in Figure 1, imposes important constraints on its design. To minimize degradation of the high precision CsI(Tl) crystal calorimeter energy resolution immediately beyond the PID system radially, it must be thin and uniform in terms of radiation lengths. It should also be small in the radial dimension to reduce the volume, and hence the cost, of the calorimeter. The drift chamber must provide a high precision measurement of the momentum and direction of a charged particle entering the system down to the lowest possible momentum.

For operation at high luminosity, the PID system needs fast signal response, and should be able to tolerate high instantaneous and integral background rates.

The DIRC detector described here is able to meet these stringent requirements very well. In particular, the DIRC is able to provide π/K separation of greater than 2 σ for all tracks from B meson decays with momentum greater than 0.7 GeV/c. At the highest momenta, the momentum versus angle correlation for two body decays is particularly well matched by the DIRC acceptance. The larger track angles of incidence associated with the higher momenta provides a higher yield of internally reflected Cherenkov photons.

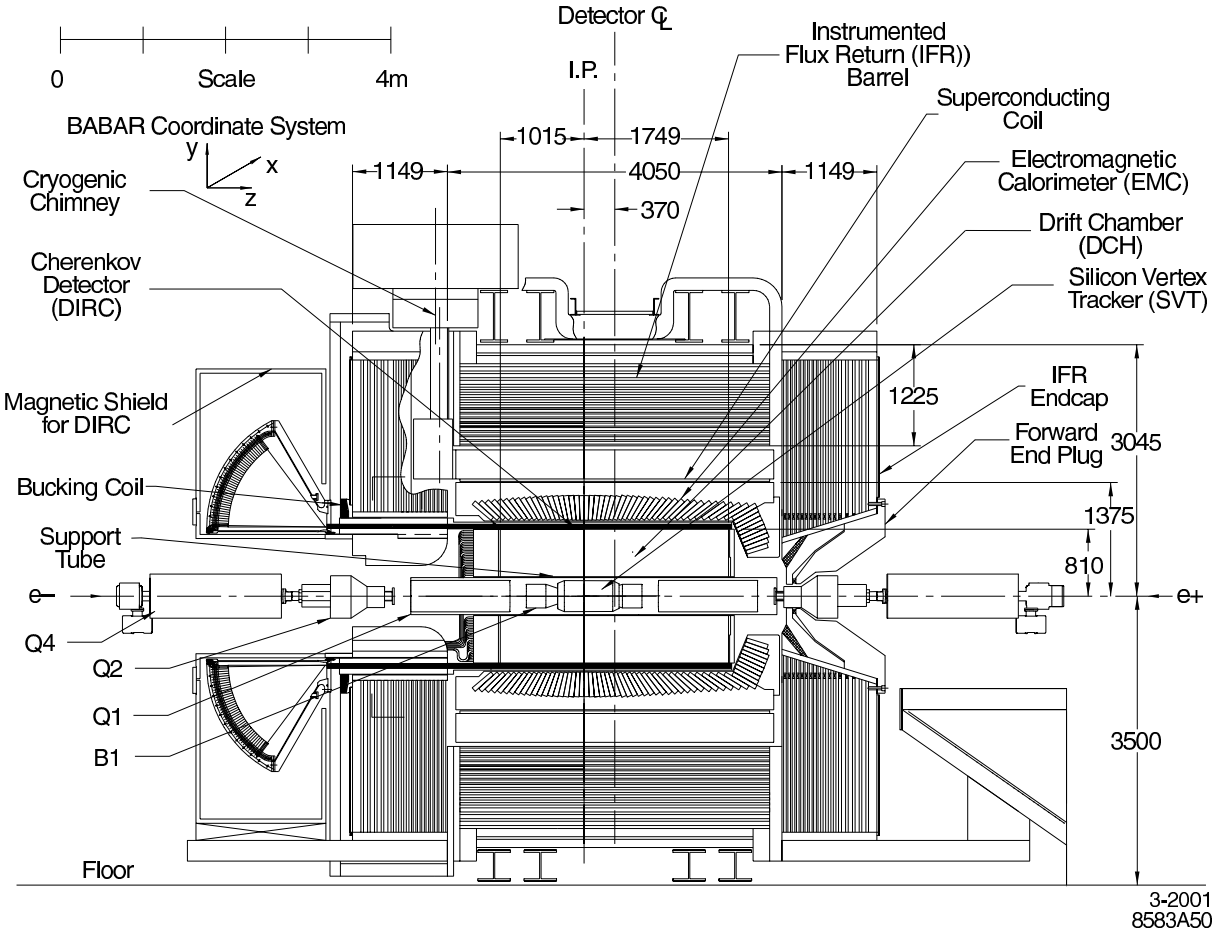

Figure 1. Elevation schematic of the *BABAR* detector. All dimensions are given in millimeters.

2. Overview

The DIRC is a subtype of a Ring Imaging Cherenkov counter (RICH)[6]. It transposes the usual principle for use of light from the radiator of a RICH by collecting and imaging the total internally reflected light, rather than the transmitted light. A DIRC utilizes the optical material of the radiator in two ways, simultaneously: first, as the Cherenkov radiator, and second, as a light guide for the Cherenkov light trapped in the radiator by total internal reflection. Since the magnitudes of angles are preserved during reflection from a flat surface and losses from the total internal reflection process are small, the photons of the ring image can be transported to a detector away from the path of the radiating particle where they may be imaged [7,8].

2.1. Conceptual issues

2.1.1. Fundamental Cherenkov relationships

Cherenkov radiation from a relativistic particle of velocity β is emitted at a well defined Cherenkov polar angle (θ_C), uniformly in azimuthal angle (ϕ_C) with respect to the particle path such that

$$\cos\theta_C = \frac{1}{n\beta},$$

where $n(E)$ is the index of refraction of the material. Since n is a function of the energy E of

the emitted photon, there is intrinsic chromatic dispersion in the Cherenkov angle at production.

The average number of photoelectrons observed (N_{pe}) is given by the Frank-Tamm equation [9],

$$N_{pe} = 370L \int \epsilon \, \sin^2\theta_C \, dE,$$

where L is the path length of the particle through the radiator in centimeters, ϵ is the overall detection efficiency for collecting and observing these photons as photoelectrons, and E is the photon energy in electronvolts.

2.1.2. Principles of photon transport and imaging in DIRC bars

The geometry of a single radiator of the DIRC is shown schematically in Figure 2. Each radiator is a long, thin bar with rectangular cross section (with dimensions t_x, t_y). A track with velocity β passing through the radiator with refractive index n_1 emits Cherenkov radiation in a cone with opening angle θ_C around the particle trajectory. The source length of the light emitting region is the particle trajectory length in the radiating material. The angle, position, momentum and timing of the track are provided by the tracking devices, a drift chamber (DCH) and the silicon vertex tracker (SVT), located in front of the radiator, and by the crossing time of the colliding beams in the machine. Additional information about event timing is provided by averaging over photons from all tracks in each event in the DIRC itself.

Since the index of refraction of the fused silica radiator material ($\langle n_1 \rangle = 1.473$, averaged over photon wavelengths produced, transported and detected in the DIRC) is substantially larger than $\sqrt{2}$, and the index of the surrounding nitrogen gas (n_3) is approximately one, then, for a particle close to $\beta = 1$, some portion of the light will always be transported down the bar to the end. Since the radiator cross section is rectangular, the magnitudes of the angles are maintained by reflections at the surfaces of the bar. Thus, in a perfect bar, the portion of the Cherenkov cone that lies inside the total internal reflection angle is transported undistorted down the bar to the end (except for additional up-down or left-right ambiguities due to loss of information on the sign of the angle, since *a priori* the number of reflections is unknown). At the end of the bar, an image must be formed in order to turn the directly-detectable space position and arrival time of each photon into angular information.

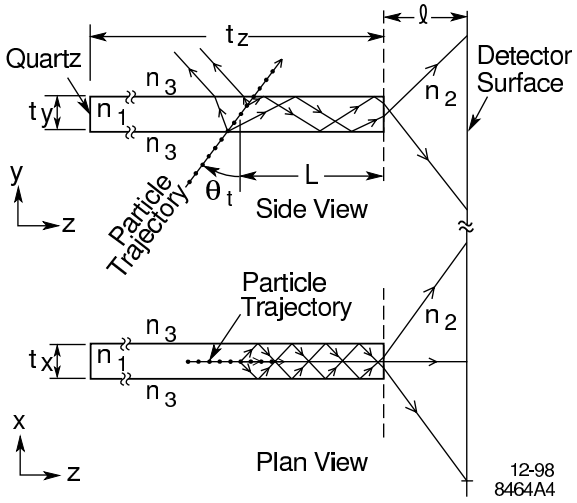

Figure 2. Side and plan views of a single radiator bar of a DIRC, and the coordinate system used in the equations presented in the text. The particle trajectory is shown as a line connected by dots; representative trajectories of Cherenkov photons are shown by lines with arrows. The labeled quantities are described in the text.

Although there are just two Cherenkov emission angles (θ_C, ϕ_C) of interest for particle identification, the DIRC is intrinsically a three-dimensional imaging device. The directly measurable quantities for detected photons are the two-dimensional space position of a *hit* in a detector *pixel* (a photomultiplier tube in the DIRC), and the associated time of the hit. The time measurement provides an additional constraint that, with sufficiently high precision, could be used to improve the measurement accuracy. In the *BABAR* DIRC, the precision achieved contributes to the resolution of ambiguities in the calculated angle

assignment and to reducing the effects of backgrounds.

The *BABAR* DIRC uses the space position of the photon at the detector in combination with the "pinhole" of the bar end to provide a measurement of the two normal angles of photon propagation down the bar (α_x, α_y). In the following equations these are assumed to have been corrected for refraction at the $n_1 - n_2$ interface to give the values in the radiator material.

The time at which the photon arrives at the detector can be related to the photon propagation time down the bar (t_{prop}). This, in turn, is directly related to the direction cosine of the photon angle along the bar z axis (α_z), and, thus, to a combination of (α_x, α_y). Since the track direction in the bar is known, the propagation angles of the photons in the bar can then be related to the Cherenkov production angles $(\theta_C,\ \phi_C)$, as described below. Only one end of the bar is instrumented by a photomultiplier tube (PMT): a mirror at the opposite end of the bar reflects photons back to the detector end. The large propagation time shift makes backward and forward going photons easy to separate.

For pedagogical purposes, the relationship between these measured quantities and the Cherenkov angles will be described below. Consider a frame where the charged particle moves along the (z) axis. The direction cosines of the Cherenkov photon emission in this frame $(\bar{\mathbf{k}}_\mathbf{x}, \bar{\mathbf{k}}_\mathbf{y}, \bar{\mathbf{k}}_\mathbf{z})$, are related to the Cherenkov angles by,

$$\bar{\mathbf{k}}_\mathbf{x} = \cos\phi_\mathbf{C} \sin\theta_\mathbf{C},$$
$$\bar{\mathbf{k}}_\mathbf{y} = \sin\phi_\mathbf{C} \sin\theta_\mathbf{C},$$
$$\bar{\mathbf{k}}_\mathbf{z} = \cos\theta_\mathbf{C}.$$

Now consider the right-handed coordinate system attached to the bar frame as indicated by Figure 2. In this frame, the track polar and azimuthal angles are (θ_t, ϕ_t). The $\bar{\mathbf{k}}$ frame x-axis is then oriented such that the direction cosines of the photon emission in the bar frame (k) can be written as

$$k_x = -\bar{\mathbf{k}}_\mathbf{x} \cos\theta_\mathbf{t} \cos\phi_\mathbf{t} + \bar{\mathbf{k}}_\mathbf{y} \sin\phi_\mathbf{t} + \bar{\mathbf{k}}_\mathbf{z} \sin\theta_\mathbf{t} \cos\phi_\mathbf{t},$$

$$k_y = -\bar{\mathbf{k}}_\mathbf{x} \cos\theta_\mathbf{t} \sin\phi_\mathbf{t} - \bar{\mathbf{k}}_\mathbf{y} \cos\phi_\mathbf{t} + \bar{\mathbf{k}}_\mathbf{z} \sin\theta_\mathbf{t} \sin\phi_\mathbf{t},$$

$$k_z = \bar{\mathbf{k}}_\mathbf{x} \sin\theta_\mathbf{t} + \bar{\mathbf{k}}_\mathbf{z} \cos\theta_\mathbf{t}.$$

The photon propagates a total path length (L_p) in time (t_p) down a bar length (L) as given by

$$t_p = \frac{L_p n_g}{c} = \frac{L n_g}{c k_z},$$

where the group velocity $(v_g = c/n_g)$ must be used rather than the photon phase velocity $(v = c/n)$ since, in a dispersive medium, energy propagates at the photon group velocity. The relationship between group and phase velocities as a function of photon wavelength (λ) is usually derived in a simple one-dimensional picture, which leads to the following relationship [10]:

$$n_g(\lambda) = n(\lambda) - \lambda\ dn(\lambda)/d\lambda.$$

In a fused silica radiator, n_g is several percent larger than n: averaged over the Cherenkov spectrum within the bandwidth of a PMT having a bi-alkali photocathode, $\langle n/n_g \rangle \approx\ 0.97$. This effect predicts a substantially greater dispersion.

2.2. The *BABAR* DIRC

2.2.1. Schematic description

Figure 3 shows a schematic of the DIRC geometry that illustrates more fully how the light production, transport, and imaging components are arranged in the *BABAR* DIRC. The radiator bars are arranged in a 12-sided polygonal barrel. Since particles are produced preferentially forward in the laboratory (the direction of the higher energy electron beam) the DIRC photon detector is placed at the backward end to minimize interference with other detectors (*e.g.,* endcap calorimeter) and accelerator components in the forward region.

The radiator material is synthetic fused silica in the form of long, thin bars with rectangular cross section. Synthetic fused silica is chosen because of its resistance to damage by ionizing radiation, long attenuation length, large index of refraction, low chromatic dispersion within the photon acceptance bandwidth, and because it allows an excellent optical finish on the surfaces of the bars [11]. To avoid instrumenting both ends of the bar with photon detectors, a mirror is placed at the forward end, perpendicular to the

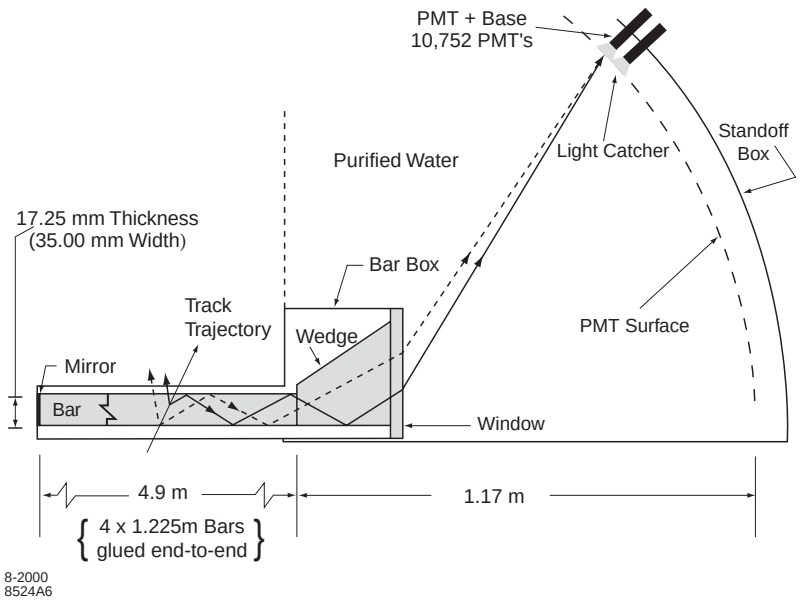

Figure 3. Schematic of the DIRC fused silica radiator bar and imaging region.

bar axis, to reflect incident photons to the backward, instrumented end.

Once photons arrive at the instrumented end, most of them emerge into a water-filled expansion region, called the *Standoff Box* (SOB). A fused silica *wedge* at the exit of the bar reflects photons at large angles relative to the bar axis. It thereby reduces the size of the required detection surface and recovers those photons that would otherwise be lost due to internal reflection at the fused silica-water interface. Not shown in Figure 3 is a small upward slope on the bottom surface of the wedge to reduce the relative displacement of downward reflected photons due to the finite bar thickness. The photons are detected by an array of densely packed photomultiplier tubes (PMTs), each surrounded by hexagonal reflecting *light-catcher* surfaces to capture light which would otherwise miss the active area of the PMT. The expected Cherenkov light pattern at the surface containing the PMT faces is essentially a distorted conic section, where the cone opening-angle is the Cherenkov production angle modified by refraction at the exit from the fused silica window. The image is usually doubled due to the side reflection ambiguity.

2.2.2. Mechanical design and physical description

The principal components of the DIRC are shown schematically in Figure 4. The bars are placed into 12 hermetically sealed containers, called *bar boxes*, made of very thin aluminum-Hexcell panels. Each bar box contains 12 bars, for a total of 144 bars. Within a bar box the 12 bars are optically isolated by an $\approx$ 150 μm air gap between neighboring bars, enforced by custom shims made from aluminum foil.

The bars are nominally 17.25 mm thick (in the radial direction), 35 mm wide (azimuthally), and 4.9 m long. Each bar is assembled from four 1.225 m pieces that are glued end-to-end (a 1.225 m length bar was the longest obtainable with high quality [12]).

The bars are supported at 600 mm intervals by small nylon buttons for optical isolation from the bar box. Each bar has a fused silica wedge glued to it at the readout end. The wedge is made of the same material as the bar; is 91 mm long, is slightly narrower than the bars (33 mm); and has a trapezoidal profile (27 mm high at bar end, and 79 mm at the light exit end). The bottom of the wedge has an upward slope of 6 mrad with

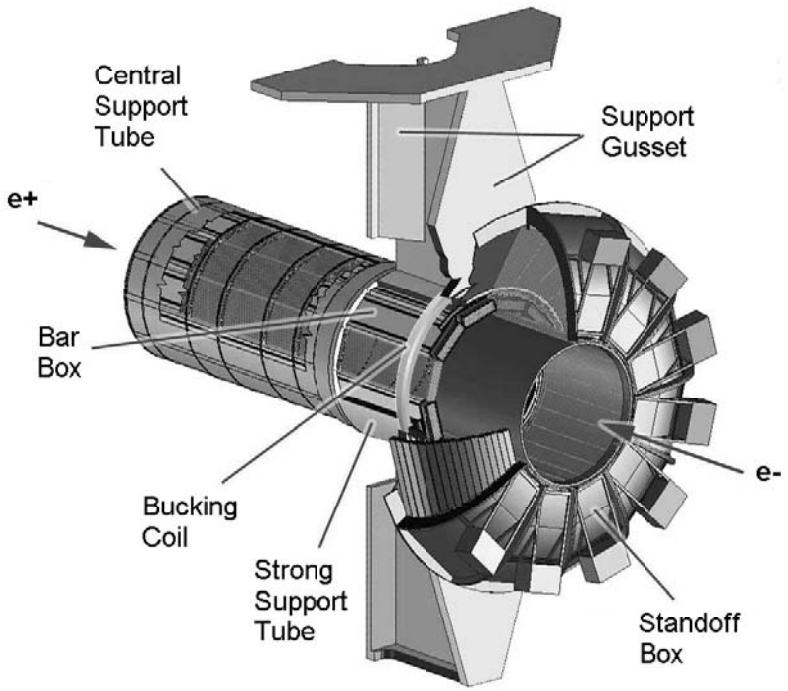

Figure 4. Schematic view of the principal components of the DIRC mechanical support structure. The magnetic shield of the Standoff Box is not shown.

respect to the long axis of the bar. The twelve wedges in a bar box are glued to a common 10 mm thick fused silica window that provides the interface and seal to the purified water in the SOB. Dry nitrogen gas flows through each box, and is measured for humidity levels to monitor that the bar box to water interface remains sealed.

The mechanical support of the DIRC is cantilevered from the iron of the *Instrumented Flux Return* (IFR). The *Strong Support Tube* (SST) (see Figures 4 and 5) is a steel cylinder located inside the end doors of the IFR and provides the basic support for the entire DIRC. In turn, an iron gusset attaches the SST to the barrel magnet iron. It also minimizes the magnetic flux gap caused by the DIRC bars extending through the flux return, and supports the axial load of the inner magnetic plug surrounding the beam in this region.

The bar boxes are supported in the active region by an aluminum tube, the *Central Support Tube* (CST), attached to the SST via an aluminum transition flange. The CST is a thin, double-walled, cylindrical shell, using aircraft-type construction with stressed aluminum skins and bulkheads having riveted or glued joints. The CST also provides the support for the drift chamber.

The SOB is made of stainless steel, consisting of a cone, cylinder, and 10,752 PMTs grouped into 12 sectors. An elevation view of the DIRC in Figure 5 includes the iron magnetic shield surrounding the SOB, which supplements a *bucking coil* to reduce the field in the PMT region to below about 10^{-4}T.

The SOB contains about 6000 liters of purified water. Water is used because it is inexpensive and has an average index of refraction ($n \approx 1.346$) reasonably close to that of fused silica, thus minimizing the total internal reflection at the silica-

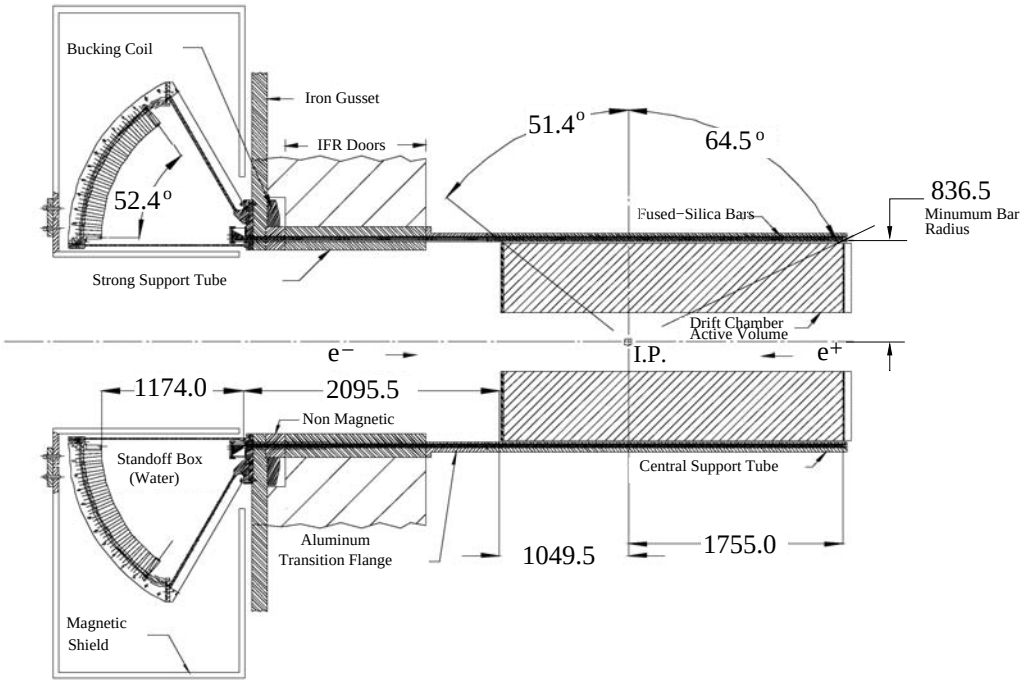

Figure 5. Elevation view of the nominal DIRC system geometry. For clarity, the end plug is not shown. All dimensions are given in millimeters.

water interface. Furthermore, the ratio of the chromaticity of the refractive indices of water and fused silica are essentially independent of wavelength, this effectively eliminates the refractive component of dispersion at the silica-water interface.

The PMTs at the rear of the SOB lie on a surface that is approximately toroidal. Each of the 12 PMT sectors contains 896 PMTs with 29 mm diameter entrance windows, in a closely packed array inside the water volume. A double O-ring water seal is made between the PMTs and the vessel wall. The PMTs are installed from the inside of the SOB and connected via a feedthrough to a base mounted outside. The hexagonal light catcher cone is mounted in front of the photocathode of each PMT, which results in an effective active surface area light collection fraction of about 90 %.

The DIRC occupies 80 mm of radial space in the central detector volume including supports and construction tolerances, with a total of about 19 % radiation length average thickness at normal incidence. The radiator bars subtend a solid angle corresponding to about 94 % of the azimuth, and covers 83 % of the phase space corresponding to the polar angle in the center-of-mass system.

2.2.3. Cherenkov photon detection efficiency and resolution

A design goal for the photon transport in a radiator bar was that no single component should be responsible for more than 10 % to 20 % loss of detection efficiency. Satisfying this criterion requires an extremely high internal reflection coefficient of the bar surfaces; *e.g.,* a requirement of 0.9992 per reflection preserves about 80 % of the light for photons undergoing up to 280 reflections while propagating along the bars. The ultraviolet cut-off is at $\approx$ 300 nm, determined by the epoxy used to glue the fused silica bars together.

The dominant contributor to the overall detection efficiency is the quantum efficiency of the PMT. Taking into account additional wavelength

independent factors, such as the PMT packing fraction and the geometrical efficiency for trapping Cherenkov photons in the fused silica bars due to total internal reflection, the number of expected photoelectrons N_{pe} is approximately 23 for a $\beta = 1$ particle entering normal (radially) to the surface near the center of a bar, and increases by a factor of two in the forward and backward directions. The DIRC detection efficiency is discussed in more detail in Section 10.2.1.

The distance from the end of the bars to the PMTs, together with the size of the bars and PMTs, sets a geometric contribution to the single photon Cherenkov angle resolution. For the *BABAR* DIRC this is about 7 mrad. This is slightly larger than the resolution contribution expected from the photon production (dominated by a chromatic term of about 5.4 mrad) and dispersion during transmission through the optical elements. The overall single photon resolution expected due to these terms is about 10 mrad.

3. Mechanical support structure

Integration of the DIRC into the *BABAR* detector is complicated by the requirement that the fused silica bars must pass through the flux return steel of the solenoid magnet. Complete azimuthal coverage of the active volume of *BABAR* by the DIRC is inconsistent with the support of the iron end-plug it surrounds. Hence, the mechanical design of the DIRC is a compromise that obtains the maximum azimuthal coverage while maintaining a conservative engineering approach to restraining the iron end-plug against gravitational and magnetic forces.

3.1. Requirements overview

A basic design goal for mechanical support of the DIRC is that the material it introduces in the active volume of the detector ($25.5^\circ \leq \theta \leq 141.4^\circ$) should be less than that of the fused silica radiators when measured in radiation lengths (13.8 $\%X_0$ at normal incidence). It should be as uniform as possible to reduce systematic effects in particle identification and the energy response of the electromagnetic calorimeter. The limitation on the radial thickness of the DIRC in this region demands extremely tight mechanical tolerances with little clearance for installation or seismic motion.

The requirement of full coverage of the calorimeter in the forward direction requires that the DIRC support be cantilevered from the backward end of the detector, so that the DIRC must also support the drift chamber (0.68 tonnes). Outside of the *BABAR* magnet flux return, the structure must support the SOB containing 6 tonnes of water. Rails and features on the inside of the DIRC support are provided to allow the support and removal of the flux return endplug. An additional challenge to the design is to ensure access to the drift chamber electronics through a tunnel limited by the 0.8 m inner radius of the DIRC and partially obstructed by accelerator components. To reduce the impact of stray magnetic fields on the photomultiplier tubes and the PEP-II accelerator components, the mechanical structure also incorporates a bucking coil (see Section 4) with special mechanical constraints.

The water contained by the SOB represents a major concern since a leak into the calorimeter structure has the potential to destroy the CsI crystals it holds. The DIRC mechanical design incorporates channels to direct water away from the calorimeter. These also allow the early detection of leaks and the possibility to drain the entire SOB water inventory quickly. Condensation from a water leak or changes in dew point on the surface of the fused silica bars are also considered as this would destroy the total internal reflection necessary to transport the Cherenkov light down the length of the bars. This eventuality is addressed by maintaining a continuous flow of dry nitrogen across the bars.

Only 1 mm of radial clearance is available between the bar boxes and the support structure framework. This is a major challenge for the mechanical design, fabrication and assembly of the roughly 5 m-long bar boxes. To allow staging of the construction, and ease of repair, the bar boxes can roll into the mechanical support, analogous to the drawers in a filing cabinet. They can be installed relatively quickly into *BABAR*, with only the water seal and gas supply and return lines to be completed after they are slid into place.

3.2. Design approach

Mechanically, the DIRC is divided into two major pieces. The SOB, which includes the photomultipliers and related electronics, and magnetic shield comprise one component. All the remaining structures comprise the second; these include the mechanical support of the entire DIRC, the fused silica bar enclosures, and the fused silica windows that provide the interface between the fused silica bar wedges and the water in the SOB. The mechanical interface between the two components is through a single *Assembly Flange* (AF) that incorporates all the mechanical fasteners, precision alignment features, and water interface between the two sub-assemblies.

Within the mechanical support, the DIRC is sub-divided again into three major components: 1) the *Strong Support Assembly* (SSA) that withstands the gravitational, magnetic and earthquake loads of the entire DIRC; 2) the *Central Support Tube* (CST) and the *Transition Flange* (TF), which support the bar boxes in the active region of the detector; and 3) the fused silica bars and their local support in the bar box modules. The design and fabrication of each of these major components is described in the following three subsections.

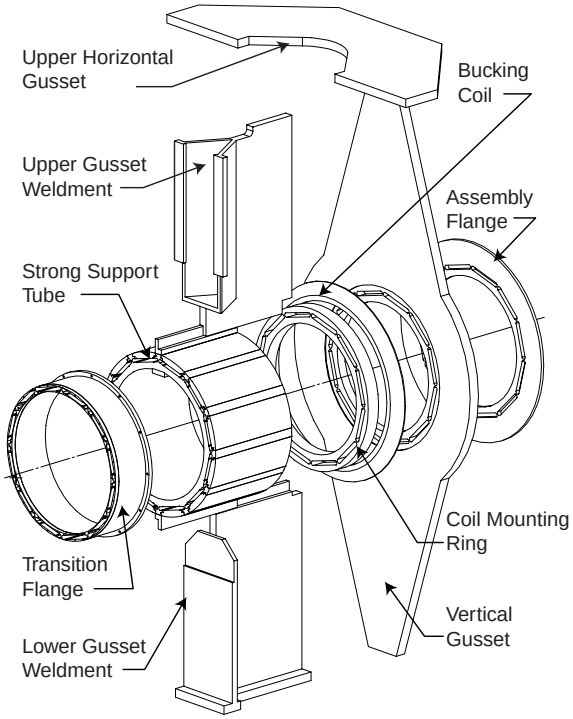

Figure 6. Exploded view of the Strong Support Assembly. Missing from the figure are the Stand-off Box in the rear, and the Central Support Tube in the front.

3.3. Support structure assembly

With an overall height of over 6.7 m, a mass of more than 30 tonnes, and numerous features with fabrication tolerances less than 250 μm, the SSA contains a level of mechanical precision unusual for structures of its considerable size and weight. The design is driven by a diverse set of functional and structural requirements resulting from its support of DIRC and other subsystem components as well as its position within the backward end of the *Flux Return Assembly*. Figure 6 shows an exploded view of the SSA.

3.3.1. Design constraints and requirements

The SSA and CST contain precisely aligned rectangular slots for bar boxes and tracks that guide the boxes during insertion and hold them in their final radial positions. To ensure that adequate clearance for installation is maintained along the length of each slot, the bar box slots are machined and each SSA component is aligned during assembly. Precise machining is required for the tracks in the SST to ensure smooth running of the bar box wheels and cam-followers during installation. The absolute location of the tracks is important to guarantee alignment with the aluminum tracks that extend into the CST.

The 5 mm radial clearance between the outside diameter of the CST and the inside diameter of the electromagnetic calorimeter calibration system imposed stringent stiffness and alignment constraints on the CST and the SSA (which supports the CST as a cantilevered load). Although the total mass of the CST loaded with bar boxes is relatively low, approximately 1.6 tonnes, the small radial gap necessitated detailed structural analysis to ensure that neither static deflection nor a moderate seismic event would cause colli-

sion with surrounding structures.

The SOB is supported as a cantilevered load off the backward end of the SSA. With a total mass of 15 tonnes and lower stiffness than the SSA, the SOB constitutes a significant static load on the SSA. Prior to detailed finite element analyses, there was some concern that the SOB could act as a resonator during seismic events such that it could drive large displacements of the free end of the CST.

The SOB water seals are made to the AF on the SSA. The AF contains twelve O-ring grooves for bar box diaphragm seals as well as two polished O-ring surfaces for the large diameter seals to the outer cone and inner cylinder of the SOB. In the event of a water leak in one of the bar box diaphragm seals, drainage passages plumbed into the *Coil Mounting Ring* (CMR) allow water to escape before hydrostatic pressurization of the CST bar box liners occurs.

To support the bucking coil with respect to the magnetic carbon steel SSA, the stainless steel CMR is incorporated into the assembly. In order to facilitate disassembly of the SSA for repair or replacement of the bucking coil, the upper and lower gussets are bolted, rather than welded, to the large vertical gusset.

3.3.2. Static and magnetic loads

The SSA and the backward end-plug, which it holds in place, are part of the flux return path for the superconducting solenoid. The SSA resists 2.2×10^6 N of magnetic force tending to pull the SST and backward end plug into the central region occupied by the drift chamber. The backward end plug is a cylindrical assembly made from low carbon steel with a total mass of approximately 11.3 tonnes. The assembly consists of two pieces; a semi-circular lower portion and horseshoe-shaped upper portion. The lower portion is bolted into the SST inner cylinder at the five o'clock and seven o'clock locations. The upper portion is removable for service access and is mechanically restrained by the lower portion and a steel plate, referred to as the Plug Stop, bolted to the inside diameter of the SST inner cylinder at the twelve o'clock location.

The drift chamber is supported inside the CST at its forward and backward ends. Its forward end flange is held in position with twelve radial supports, two adjustable struts and ten shims. With a mass of approximately 0.7 tonnes, the Drift Chamber also contributes to the static deflection of the CST due to gravity.

The physical location of the SSA in the *BABAR* detector imposes spatial constraints in addition to those already discussed. The backward doors of the IFR assembly close around the SSA with a nominal clearance of only 10 mm from the SST and gussets. Once these doors are closed, access to the structure is completely blocked. The bucking coil and CMR water plumbing are designed to stay clear of the path of the inner corners of the doors that open and close at a five-degree angle. The triangular chimney for the cryostat of the superconducting solenoid restricts the bolting locations available on the flux return upper mounting plate to two narrow strips on either side of the chimney.

3.3.3. Design and fabrication

The fundamental challenge in designing the SSA proved to be balancing the need for high precision in the bar box slots with the stiffness and strength requirements imposed by magnetic forces, seismic loads, and limited clearances around the structure.

The bar box slots in the SSA pass through five separately machined components made from three different materials, bolted and pinned together. The material between two slots is referred to as a septum. The competing goals of maximizing septum thickness and bar box clearance drives the tolerance requirements for machining of slots and alignment of all components. Twelve septa, each less than 15.2 mm wide, connect the inside of each cylindrical part to the outside. Early in the design process it was recognized that magnetic forces would create high stress in the septa. The requirement to maximize the azimuthal radiator coverage and the need for bar box insertion clearances limits the amount of material that can remain in the septum area. Every effort was made during the design process to maximize the septum thickness and thereby minimize stress. Because failure in one septum could increase the stress

in others catastrophically, the strength of these septa was deemed to be of critical importance to the integrity of the DIRC structure and subsequently the backward end of the *BABAR* detector itself.

The SST consists of a continuous inner cylinder and an outer cylinder comprised of twelve plates. The 1143 mm long septa connecting the inner and outer cylinders are machined into the forged carbon steel inner cylinder and transfer approximately 1.7×10^6 N of magnetic force from the inner cylinder to the outer cylinder. The SST is the primary strength member in the SSA, resisting radial and bending forces that tend to put the forward end of the assembly in tension and the backward end in compression. Figure 7 shows the construction details of the SST.

The bar box slots in the SST contain track features in which the bar box wheels ride during insertion. In order to ensure proper fit and guidance of the wheels, the track features are machined to a unilateral profile tolerance of 0.1 mm. The bar box slots in the SST are machined to a unilateral profile tolerance of 0.25 mm. These tight tolerances, the overall length of the assembly of 1149 mm, and the narrow radial width of the slots of only 41 mm, precludes machining the slots and tracks in a continuous steel ring with conventional or wire EDM (Electrical Discharge Machining) techniques.

The solution is to fabricate the outer cylinder in segments that are bolted and pinned in place on the outside of the inner cylinder. This design allows precise machining of all features inside the slots with conventional machining techniques. Each outer cylinder segment is aligned to its respective inner cylinder slot with tooling that indexes the tracks in both parts. Once the segments are aligned, they are bolted in place and match-drilled and pinned. The use of these bolts and shear pins to hold the segments in place maximizes the radial stiffness of the assembly.

All components of the SST are electroless plated with 25 μm of nickel. This plating provides a tough, corrosion resistant bearing surface in the bar box wheel tracks. The option of selectively plating the track surfaces and painting other exterior surfaces was explored and dismissed because of the availability of plating tanks of adequate size to accommodate the inner cylinder. Given the proximity of deionized water in the SOB, rust resistance was deemed to be of critical importance.

The TF is fabricated as part of the SSA because of the need to achieve precise alignment of bar box tracks in the CST with respect to the tracks in the SST. The TF is a thick wall cylinder about 500 mm long and 1780 mm in diameter, machined from a single piece of a rolled ring forging of aluminum 6061-T6 alloy. The slots are machined from either end of the ring to a unilateral profile tolerance of 0.5 mm. The slot dimensions and profile tolerance are larger than that for the slots in the SST and other SSA components, achieving a clearance fit with the slot liners of the CST. The slot liner assemblies containing the CST bar box tracks are subsequently aligned in the TF slots to match the tracks in the SST.

The CST and SSA were fabricated concurrently, the CST at Lawrence Berkeley National Laboratory (LBNL) and the SSA in Kobe, Japan by Kawasaki Heavy Industries (KHI). The TF was machined with a matching aluminum template as the first component in the SSA. It was then shipped to LBNL so that the CST fabrication could begin while the SSA machining continued in Japan. The aluminum template remained at Kobe and was subsequently used during the acceptance tests to demonstrate proper alignment of the TF slots with respect to slots in the rest of SSA.

The composite portion of the CST, which has a smaller thickness in radiation lengths, is slightly longer than that necessary to meet the physics requirements in order to decrease the length of the TF. With a total length of 505 mm, the TF extends 135 mm short of the active region of the detector. This length is selected to facilitate fabrication of the TF from a single forging with conventional machining techniques. A detailed finite element analysis of the DIRC structure [13] indicates that the additional length of composite structure has an acceptably small affect on stiffness.

Two dowel pins, located in the six and twelve o'clock positions, align each cylindrical component to the next. The bar box slot features in all

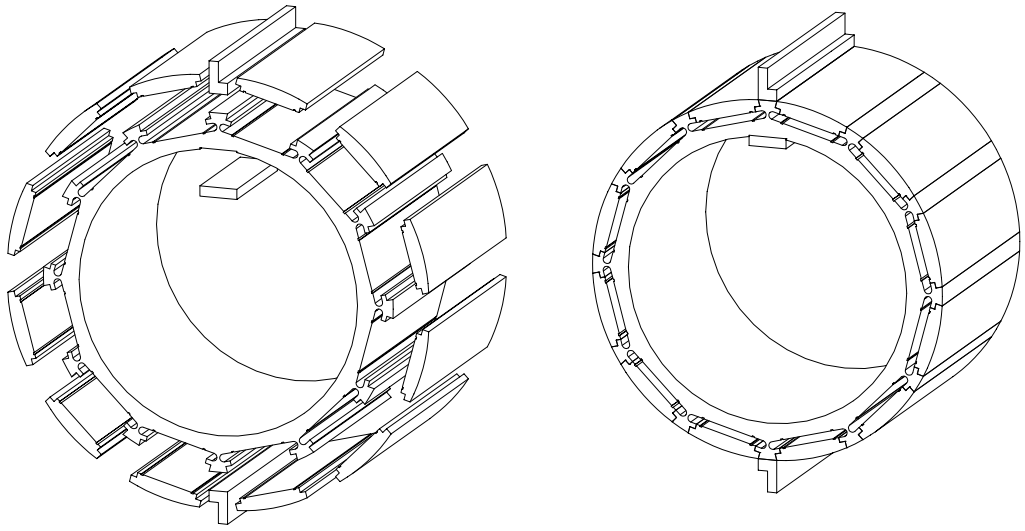

Figure 7. Exploded view showing the construction of the steel of the Strong Support Tube (left) and the assembled part (right).

parts are located with respect to the dowel pin holes. A carbon steel template is used to establish the position of the slots and alignment holes during machining of the steel and stainless steel parts. This template is fabricated with slots having a profile tolerance of 0.05 mm and locating holes with a true position tolerance of 0.1 mm.

The slots in the assembly flange, vertical gusset, and coil mounting ring do not contain bar box track features. The vertical gusset and coil mounting ring slots are machined to a unilateral profile tolerance of 0.5 mm. The assembly flange slots are machined to a tighter tolerance of 0.25 mm in order to assure adequate thickness of the thin wall of material between the O-ring grooves for the bar box diaphragm seals and the slots in the septum area.

The vertical gusset, upper horizontal gusset, upper gusset weldment, and lower gusset weldment, are fabricated from carbon steel plate (ASTM A-36). The interface surfaces between the gussets and the vertical gusset are machined to a tolerance from 0.1 mm to 0.25 mm to ensure continuous contact in bolted connections. In order to achieve these tolerances and the long-term stability of the assembly, all parts are stress relieved prior to final machining.

To facilitate disassembly for access to the bucking coil the upper and lower gusset weldments are bolted and pinned to SST gusset brackets, which are bolted and pinned to the SST inner cylinder. These bolts and shear pins transfer the considerable shear forces caused by magnetic loads on the SST and backward end plug.

The upper portion of the lower gusset weldment mounting flange overlaps the outer radius of the superconducting solenoid. In order to avoid affecting the shape of the magnetic field, a nonmagnetic stainless steel plate forms this portion of the flange.

The DIRC structure is held onto the IFR by bolts passing through custom machined alignment shims and mounting holes in the SSA. The mounting holes in the upper and lower gusset weldments are drilled 5 mm larger than the diameter of the mounting bolts to accommodate alignment clearances and machining tolerances. In order to maximize the amount of clearance available for adjustment of the DIRC structure during installation, the holes are toleranced to a true position of 1.0 mm with respect to datums on the assembled structure. The final location of the thread inserts in the mounting plates on the IFR are measured at SLAC. These measured lo-

cations are used as the nominal locations for the mounting hole drilling in the two weldments while they were at KHI. The high precision of the gusset weldments, the SST mounting brackets, and the vertical gusset, enabled KHI to meet the required tolerance by machining the mounting holes in the gusset weldments prior to final assembly. Because the upper horizontal gusset is designed primarily to brace the DIRC during seismic events, a larger clearance of 10 mm is selected for its mounting holes.

3.3.4. Assembly and acceptance tests

Assembly of the SSA is performed with the axis of the SST vertical. Dowel pins are installed to align each pair of components containing bar box slots. A detailed half-symmetric finite element model of the DIRC structure is used to analyze the stresses and deflections resulting from gravitational, magnetic, and seismic forces. Figure 8 shows the deflection of the structure. This finite element analysis calculation models the effect of the fully loaded SOB as an applied vertical load rigidly attached to the assembly flange on the left side of the figure. The maximum stress is predicted to occur within a septum in the Vertical Gusset at approximately the 8 o'clock position.

The system is designed to withstand approximately 210 tonnes of magnetic loading with the solenoid at a field strength of 1.5 T. Measurements of the stresses in the SST caused by magnetic forces are made that focus on the forward end of the SST in the thinnest regions of the steel at the septa. All measurements were within specified safety tolerances.

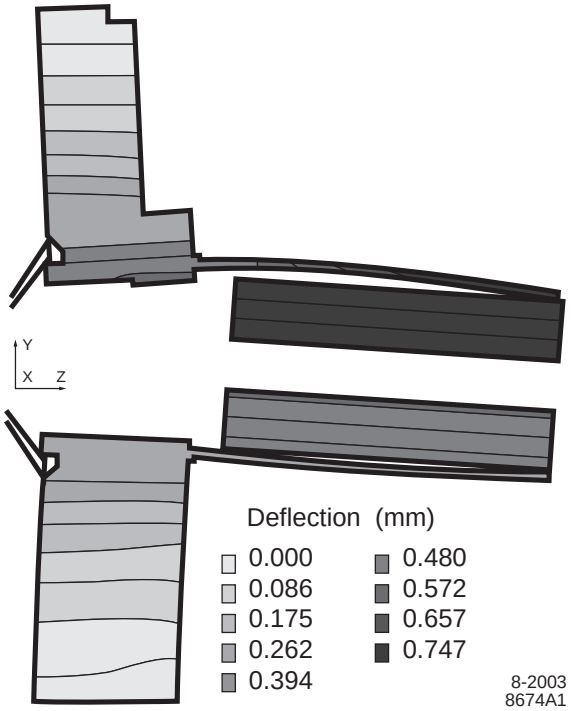

Figure 8. Deflection of the strong support structure and the Central Support Tube under the combined magnetic and static gravitational loads, including the drift chamber. The amount of deflection of the structure has been exaggerated for clarity.

3.4. Central support tube

The CST is a cylindrical assembly of 1790 mm diameter, 3350 mm length, and a radial thickness of 77 mm. It is mounted horizontally within *BABAR*. Its primary function is to support and position the radiator bar boxes accurately within the active region of the detector.

Several components make up the CST as shown in Figure 9: the TF, which is a rigid flange for mounting the CST to the SSA; a lightweight cylinder section attached to the TF made up of 12 I-beams and 12 bar box slot liners; and an aluminum skin bonded to the inside and outside of the CST frame. The slot liners incorporate track details that guide the bar boxes during installation, and are continuous throughout the TF and the CST. More details of the structure at a bulkhead section near the end ring are shown in Figure 10.

The CST must be mechanically rigid while minimizing the number of radiation lengths of material it introduces in front of the calorimeter. Additionally, the bar box liners must be straight and have an accurate profile, as described below. The stiffness requirement comes from the need to stay within the allocated space envelope within the detector. In effect, the CST is a cantilevered beam since it is supported only at the backward

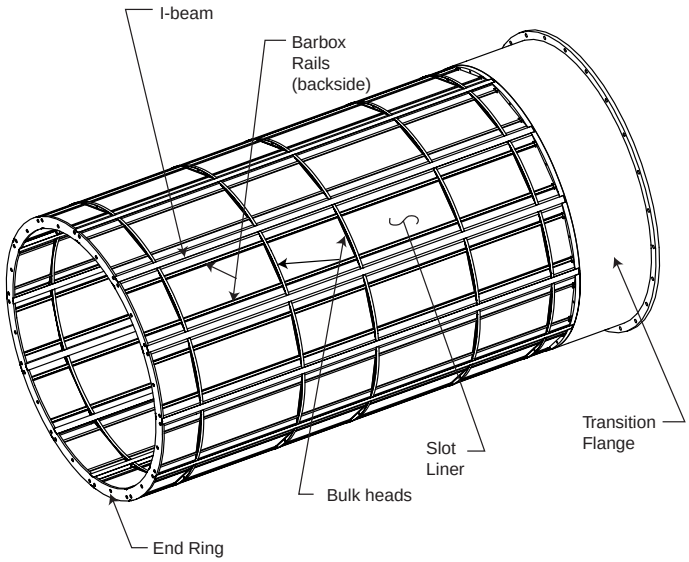

Figure 9. Schematic diagram of the Central Support Tube and Transition Flange. The outer aluminum skin is missing in this view to show the internal construction of I-beams, bulkheads, bar box slot liners.

end of the detector. It supports the mass of the bar boxes (about 1.6 tonnes) and the forward end supports half of the 0.68 tonne mass of the drift chamber. The small radial clearance between the outside diameter of the CST and the inside diameter of the calorimeter calibration system requires that the CST outside surface be within 1 mm of its nominal design surface.

The CST cylinder is constructed with a structure similar to that used in an airplane wing or fuselage. It has internal I-beam stringers and bulkheads against which a thin skin is bonded on both the outside and inside. The final assembly and skinning of the CST is done with the cylinder oriented vertically so that gravity does not cause distortion or complicate the alignment process. The skins provide most of the strength and stiffness of the cylinder.

3.4.1. Fabrication and assembly

Most of the CST elements are bonded together so that mechanical fasteners are not relied upon to carry load. A single type of commercially available 2-part epoxy adhesive is used throughout the CST. The chosen epoxy [14] has a high peel strength ($\geq$ 9000 N/m) and a tensile lap shear strength of 3×10^7 N/m^2, which are excellent strength values for this application. The epoxy is dispensed from cartridges through a mixing nozzle and can be applied to vertical surfaces without sagging due to its low viscosity. A 24-hour room temperature cure produced a 90 % strength bond. Glue line thickness was controlled using 125 μm diameter glass beads introduced into the epoxy components before mixing. All bonded components are aluminum and are cleaned to ultra-high vacuum standards. Clean procedures are used throughout the assembly sequence.

The cylinder skins provide most of the strength and stiffness of the CST. The thickness of the inner and outer skins is 1.27 mm and 0.76 mm, respectively. The I-beams are all inspected for adherence to cross section and straightness tolerances. The one exception to the no fastener approach for the support tube is the I-beam connection to the TF. The end of the TF, into which the I-beam webs are inserted, is slotted about 75 mm deep. The flanges of the beams are screwed and bonded [15] to the TF. During insertion of the bar box liner assemblies between I-beams, alcohol is used as a lubricant. The CST end flange is attached to the I-beam ends. Alignment is achieved

using fixture struts so that the CST forms a true cylinder. The free end (closest to the end-flange) is aligned with the TF base of the CST cylinder, secured by epoxy [15] injected into the I-beam-to-bulkhead joints through injection holes.

The inner and outer CST skins are each divided into six 60° arcs. During assembly, each inner and outer skin section is clamped to the CST frame using "skinning" fixtures that are fabricated by aligning the fixture parts on a surface table and bonding all parts of the frames together. This enables the skins to be bonded while the overall shape is being held as a true cylinder.

The skinning process is repeated for each of the six pairs of skin segments. Prior to bonding each new pair of skin segments, the free end is re-aligned with the TF at the base of the CST cylinder. A consistent glue line thickness of 0.38 mm is maintained between the skins and the frame by burying 0.38 mm diameter wires in the glue line [14]. The critical joint in the CST is that between the lightweight cylinder section and the TF. The I-beams and the skins share the shear load through a lap joint along the full circumference of the TF (approximately 0.85 m^2), which is adequate to support 2.5 tonnes.

After bonding all the skin segments, the alignment of the End Flange with respect to the TF is within 125 μm. When the CST is rotated to the horizontal orientation and cantilevered from the TF, the maximum radial run-out at any position is 1.0 mm.

3.4.2. Bar box liner

The CST contains 12 bar box slots that align with corresponding slots in the SST cylinder. Four tracks in each slot guide wheels embedded in the bar boxes as they are rolled, horizontally, into the slots. There is only 1 mm of clearance between the bar boxes and the slots, so it is important for the slots to be dimensionally accurate and to be located accurately with respect to the SST slots. The goal was to ensure that the bar boxes would slide in without dragging in the slots or hitting a step at the SST/CST interface. To achieve this, the CST tracks were positioned to within a 0.4 mm zone with respect to SST features.

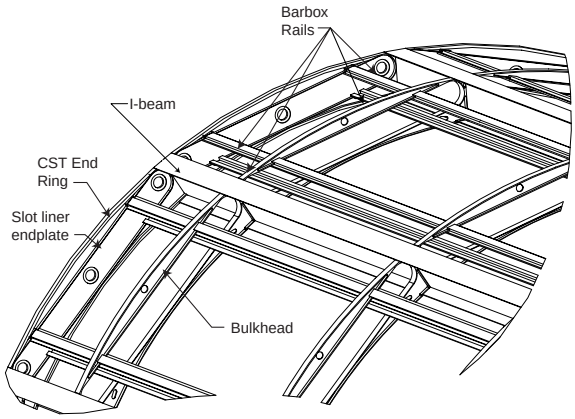

Figure 10. Details of the Central Support Tube assembly near the end opposite the Transition Flange. The inner and outer skins have been removed, as well as the four pieces of stainless steel sheet metal that form the slot liners when bolted to the rails. The rails and slot liners extend all the way through the Transition Flange.

The bar box liners consist of extruded 6063-T6 aluminum track sections screwed and bonded [16] to two flat and two U-shaped sheet metal sections to form the rectangular liner section. During the assembly of the liners, the four tracks were held straight and in accurate position by fixtures while the sheet metal sections were match-drilled and bonded.

To support the bar box liners inside the CST, lightweight bulkheads (170 g) were produced from aluminum plate using a CNC (Computer Numerically Controlled) machine. They were bonded onto the bar box liners while the liner internal fixture is still inside the liners. Each is carefully inspected and required to be of nominal size, within $\pm$ 25 μm. During bonding the bulkheads were positioned and aligned with respect to each other by fixtures mounted on a granite table. Figure 11 is a cross section through the CST that shows the details of a bulkhead support.

3.5. Standoff Box

The main purpose of the SOB is to support the DIRC photodetector array of 10,752 PMTs

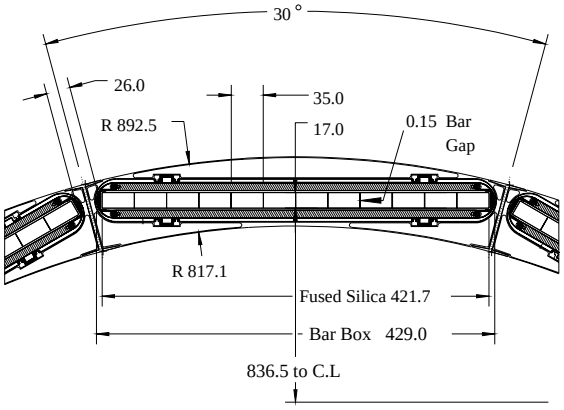

Figure 11. Cross section though the Central Support Tube showing a bulkhead, the slot liner and a bar box. The inner and outer skins are not shown. All dimensions are in millimeters.

to form a surface that is roughly a toroidal section (see Figures 4 and 5). It is fabricated from stainless steel to form a tank containing about 6000 liters of very pure water.

The SOB consists of a cone, a cylinder, and twelve sectors. Each sector has 896 22-mm-diameter drilled holes onto which the PMTs are mounted. The twelve detector sections are grouped into two sets of six detectors, split along a vertical axis to form two doors. The doors open and close in a "clam-shell" arrangement, employing two sets of hinges mounted on the cone section. There are also a small number of additional holes drilled into the cone, as itemized below.

- Two holes, 19 mm in diameter, at the top and the bottom for the water and gas leak test systems. A tube is attached to one of the bottom holes to distribute the water on the bottom half of the SOB.

- One large hole, 100 mm in diameter, at the bottom and top for the emergency water drain and to allow the inside of the SOB to be dried after draining.

- Six closable glass windows, 146 mm in diameter, to allow visual inspection of the inside of the SOB.

- Twelve holes (one for each sector), 40 mm in diameter, to accommodate an optical fiber for the PMT calibration system.

The number and mass of each element of the SOB is given in the Table 1. The fully equipped SOB, without water, weighs a little more than 10 tonnes.

Table 1
Mass of the SOB elements.

component	number	unit mass (kg)
Cone	1	4050
Cylinder	1	700
Sector	12	217
Sector (with PMT)	12	377
Hinge	2	317
Hinge support	4	65
Water pipe	1	85

3.5.1. Construction and installation

The SOB was built by the company Girod Sisa [17] in France. As part of the construction quality assurance procedures, a series of tests were designed to be performed at the factory, concluding with the complete assembly of the structure and leak testing with water. In this test, most of the PMT holes were filled with simple plugs; twelve of the holes were sealed using a set of the final PMT feedthrough assemblies. This procedure proved to be invaluable in optimizing the assembly process, especially ensuring good tightness at the junction between the linear gasket between two sectors and the big O-rings of the cone and the cylinder, the so-called "T-joint".

The cone, central tube and all other material was shipped directly by boat to SLAC. From Girod Sisa the twelve sectors were sent to DAPNIA/Saclay where the PMTs were mounted on the sectors and tested for basic performance under nominal HV conditions. The tested sectors, with the PMTs still mounted, were then shipped by air to SLAC.

The assembly was performed in a large dust-free tent. It began with bolting together the

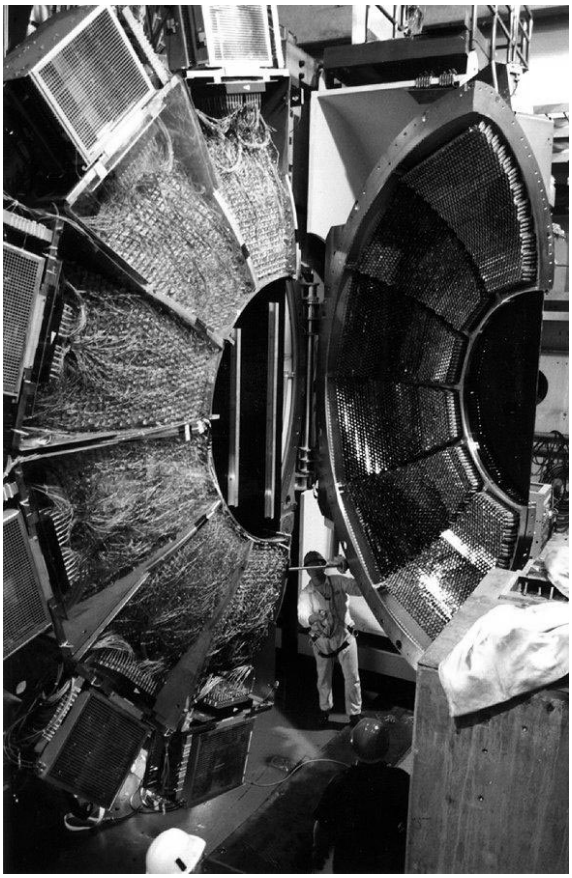

Figure 12. Photograph of the open DIRC SOB with all 10,752 photomultiplier tubes installed.

twelve sectors horizontally. They were then lifted as a unit and lowered onto the cone and cylinder assembly, still in a horizontal position. The two assemblies were bolted together and the hinges attached. Finally, the whole SOB was rotated into the final vertical position. After careful reviews of the procedures for opening and closing the clamshell doors (manually), the device was ready for leak tightness tests and electronic tests of the PMTs. A photograph of the fully instrumented SOB is shown in Figure 12.

3.5.2. Leak tightness test

Due to the large number of gaskets in the SOB design, the possibility of water leakage is a major concern. The filling and draining of the SOB with

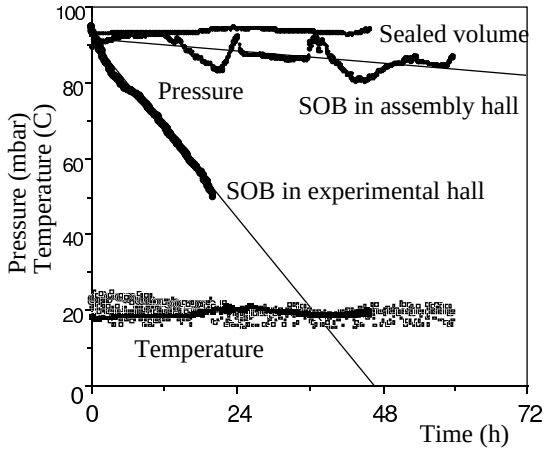

Figure 13. Graph of the pressure and temperature versus time obtained with the gas leak tightness test bench in 3 cases: 1) a small sealed-volume vessel; 2) in the assembly hall with an observed water leak of 1 L/h; and 3) in the experimental hall with a slight water leak of 0.01 L/h.

ultra pure water is a delicate and time-consuming task, so a relatively fast and safe leak tightness test using gas was developed. This test is used whenever the SOB doors are opened and closed.

The gas-based leak tightness test is based on the use of a differential pressure gauge. One input is connected to a small buffer volume, used as reference, and the second input is connected to the SOB. The gas used in this test is argon. The procedure is to apply an initial overpressure between 80 mbar and 120 mbar and to follow the evolution of this overpressure with time. Since this test is sensitive to temperature changes, the temperature is monitored during the test.

Figure 13 shows the sensitivity of the apparatus when tested on a small well-sealed vessel (8 L) and when used on the SOB. When the gas leak test was performed in the assembly hall a gaseous leak of about 200 Pa/h was detected, corresponding to a water leak of about 1 L/h.

The first time the SOB was filled with water in the assembly tent, numerous small leaks were observed around the PMT feedthrough ports. These were fixed easily by tightening the external mounting nut that is screwed onto the threaded

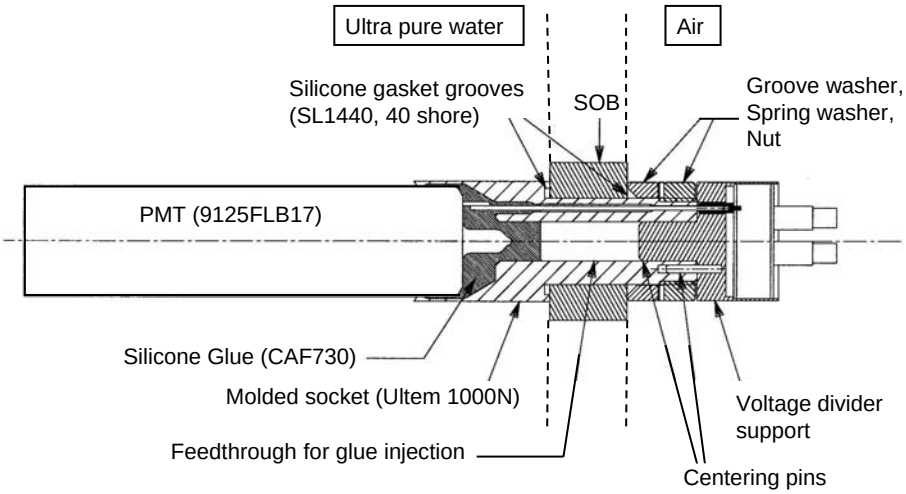

Figure 14. Cross section of the PMT feedthrough assembly mounted to the sector bulkhead.

PMT socket (the seal is formed by silicone O-rings, secured in gasket grooves, inside and outside of the sector bulkhead – Figure 14). During the second test leaks were found around several of the T-joints. Most were fixed by tightening nearby bolts, but a leak of about 1 L/h persisted at the T-joint between sectors 5 and 6, and the cone. When the doors were opened it was discovered that the custom-molded gasket had a fabrication flaw, which was repaired simply using a silicone resin.

After SOB installation on *BABAR* in the experimental hall, the gas leak measurement was 0.12 mbar/h, which corresponds to a low-level leak of about 0.01 L/h. These leaks were easily fixed by re-tightening a few bolts close to the leak.

3.6. Installation and alignment of the DIRC in *BABAR*

The installation of the DIRC radiator structure into *BABAR* is complicated by the small clearances between the DIRC and the other *BABAR* sub-systems and the large physical dimensions and weight of the entire device. To install the DIRC, a large fixture was constructed that could rotate the DIRC around three axes or translate the DIRC in two transverse dimensions within comfortable limits anticipated for the initial alignment.

In the z direction, motion of the DIRC is obtained by rollers on a custom track; its position in this coordinate is controlled by hydraulic jacks. The fixture is designed so that it can also support the SOB. If necessary, the entire DIRC can be removed from *BABAR* on this platform, though this would require the removal of several accelerator components and the Drift Chamber.

Based on optical survey measurements, the DIRC has been installed to within 1 mm of its expected position. Measurements of the bending and strains of the DIRC structure under combined gravitational and magnetic loads, taken without the Drift Chamber and SOB present, are consistent with expectations.

3.7. Material inventory in the experiment fiducial region

Table 2 lists the materials used in the construction of the DIRC support structure and the bar boxes (see Section 5). The distribution of material as a function of the angle ϕ from the center to one edge of a bar box is shown in Figure 15. The two curves in the plot correspond to the amount of material in front of the radiator bars due to the mechanical structure of the DIRC only: the lower curve ends at an angle of 14° corresponding to the edge of the bars; the upper curve is the ma-

terial in front of the calorimeter due to the DIRC only and stops at 15°, corresponding to the symmetry of each bar box about its long axis and the 12-fold symmetry axis of the DIRC.

The structures in the plot between $8° - 11°$ are the rails for wheels of the bar boxes. The structure between $12.5° - 14.5°$ is the aluminum extrusion of the side rail. The sharp peak at $\phi = 14.1°$ (upper curve only) is the end of the radiator, followed by another, similar peak due to the vertical wall (24 mm high) of the side rail of the bar box. Finally, the big peak (0.87 radiation lengths) at the right edge of the plot is due to the "lattice" of solid aluminum I-beams in the CST plus the inner and outer skins.

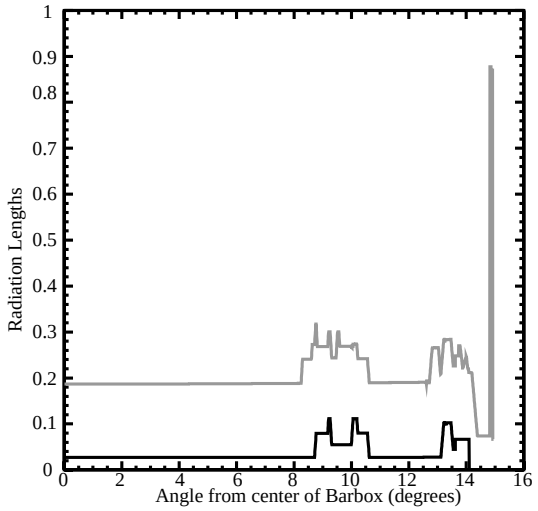

Figure 15. The amount of material in the DIRC as a function of the azimuthal angle from the center of a bar box for an infinite momentum track from the interaction point. The lower curve is the material in front of the fused silica bars due to the mechanical structure of the DIRC. The upper curve is the amount of material in front of the electromagnetic calorimeter due to the DIRC.

In Table 2 and Figure 15, only components of the DIRC that are continuous in z are included. Listed in Table 3 are the "lumped items" such as bulkheads, wheel supports, mirrors, bar box endplate, endplate to the slot liner, and the CST end flange. These discrete items add another $0.016\ X_0$ to the average thickness of the DIRC mechanical structure; about half this material is in front of the bars.

The minimum amount of material in front of the fused silica bars and the calorimeter occurs at $\phi = 0$ and is 2.7 % X_0 and 18.7 % X_0, respectively. The average amount of material in front of the bars and the CST is 3.7 % X_0 and 20.7 % X_0, respectively, including the distributed items of Table 3. An infinite momentum particle from the interaction point that passes through the most forward, end-ring, region of the DIRC would traverse 0.35 of a radiation length.

4. Magnetic shielding

Due to the asymmetric beam energies, the detector is not symmetrical about the interaction point, as can be seen in Figure 1. Potentially, this places crucial final focus elements in a very strong fringe field of the *BABAR* flux return. Such a field would degrade the performance of the quadrupoles, reducing the luminosity significantly. The solution in the backward (negative z) region, as indicated in the figure, is to mount a bucking coil on the flux return steel encircling quadrupole Q2. This reduces the B_Z component field at Q2 to less than 100 G.

In addition to the potential affect on the accelerator, the operation of the DIRC PMTs is also challenged by these fringe fields. Even though they are mounted more than a meter from the outside surface of the flux return they could not operate in the ambient magnetic fields, which far exceed the few Gauss limit for efficient operation. Although it would have been possible to shield each PMT with mu-metal individually, this approach would have reduced the overall photon detection efficiency, as will be discussed in Section 6.2. An alternative method is to surround the entire SOB with an iron enclosure to shield against stray fields.

Due to the lack of simple symmetries and the superposition of the fringe fields of the *BABAR* flux return and the bucking coil field, the design of

Table 2
Design dimensions of components used to construct the Central Support Tube (CST) and bar boxes (BB), with dimensions and thickness given in radiation lengths. Glue and plastic parts are not included. The coordinate system is measured in the bar box reference frame (Figure 2), with y parallel to *BABAR* radial direction r, at $z = 0$. Dimensions are in millimeters, and brackets ($\langle\ \rangle$) indicate average values for complicated shapes. The number of radiation lengths is the average for each component as traversed by an infinite momentum track originating at the interaction point over the range $0° \leq \phi \leq 15°$ and at normal incidence to the long dimension of the bars.

Component	z_1	z_2	y	Δy	Material	X_0
CST Inner skin	0.00	218.59	815.79	1.27	Al	0.0143
Rigid Foam[1]	0.00	214.50	817.10	37.50	Urethane	0.0002
Slot Inner Liner	0.00	126.71	821.30	0.40	Al	0.0045
BB Skin1	0.00	195.00	825.60	0.25	Al	0.0029
BB Honeycomb[2]	0.00	195.00	825.80	8.40	Al	0.0024
BB Skin2	0.00	195.00	834.20	0.25	Al	0.0029
Fused Silica	0.00	210.07	836.50	17.25	SiO_2	0.1403
BB Skin3	0.00	195.00	855.70	0.25	Al	0.0029
BB Honeycomb	0.00	195.00	856.00	8.40	Al	0.0024
BB Skin4	0.00	195.00	864.40	0.25	Al	0.0029
Slot Outer Liner	0.00	126.71	868.00	0.40	Al	0.0045
Rigid Foam	0.00	214.50	868.70	37.50	Urethane	0.0002
CST Outer Skin	0.00	239.14	892.50	0.76	Al	0.0085
Rail Inner	126.71	154.04	818.80	$\langle 4.55 \rangle$	Al	0.0500
Rail Outer	126.71	154.04	866.20	$\langle 4.55 \rangle$	Al	0.0500
CST Beam	198.64	238.62	817.10	$\langle 8.92 \rangle$	Al	0.1003
Side Beam	195.00	214.27	827.50	$\langle 6.95 \rangle$	Al	0.0781

[1] density = 0.0687 g/cm^3; [2] density = 0.0478 g/cm^3

Table 3
List of discrete items in the DIRC mechanical structure not included in Table 2. They are divided into two classes: 1) bulkheads and wheel supports in 5 rings distributed along the entire DIRC coverage, and 2) items at the forward (uninstrumented) end of the DIRC at $\theta \approx 25°$. The average radius of all items is 845 mm. The mean radiation length is for an infinite momentum track from the interaction point. Dimensions with brackets ($\langle\ \rangle$) indicate average values for complicated shapes.

Component	Material	Δz	Δr	$r\Delta\phi$	ϕ Coverage	Mean X_0
Distributed items						
Bulkheads	Al	8	75.4	442	1.0	0.0042
Wheel supports	Al	25	16.4	390	0.881	0.0103
Forward Items						
Mirrors	SiO_2	3	17	414	0.935	0.0253
HC Termination	Al	20	15.0	390	0.881	0.0015
BB-Rear Cover	Al	$\langle 8.72 \rangle$	38	432	0.976	0.1060
SL-endplate	Al	$\langle 3.6 \rangle$	51	435	0.983	0.0441
CST end Ring	Al	$\langle 5.02 \rangle$	75.41	-	1	0.0625

an optimal shielding configuration was a considerable challenge. Nevertheless, the solution described here reduces the fringe field at the photomultipliers to an acceptable level of less than 1 G.

4.1. Simulation of the *BABAR* magnetic circuit

In order to satisfy the PMT and Q2 requirements, it was soon recognized that a combination of active (bucking coil) and passive elements (iron) was necessary.

The *BABAR* magnetic circuit consists of two active elements: a thin cryogenic solenoidal magnet, generating a 1.5 T magnetic field, and the bucking coil in the backward direction. The passive elements are also grouped into two parts. The first are those elements with a geometry determined by the central apparatus of *BABAR* such as the barrel and endcaps (forward and backward) of the IFR, the flux return plugs (forward and backward), along with part of the DIRC support structure. The second part is the DIRC magnetic shield (Figure 1), whose design had to accommodate the existing geometry and magnetic fields due to the other elements. The shield geometry is most strongly determined by the position and shape of the SOB, which is cantilevered from the Support Gusset. In the backward plug region, the DIRC support structure is part of the magnetic circuit, but the fused silica bars and bar boxes require holes in this part of the circuit, increasing the fringe field in the backward direction significantly. This ensemble of elements makes calculation of the resulting magnetic field extremely complicated, even if an axisymmetric (or 2D) approximation is used.

The primary mechanical constraints considered during the design of the DIRC shield were:

- that the beam elements must be contained within the shield cylinder;
- that access to the drift chamber is made inside the shield cylinder;
- that the magnetic shield and its support, resting on the skid plates, should also provide a counterweight for the *BABAR* IFR backward doors, when opened;

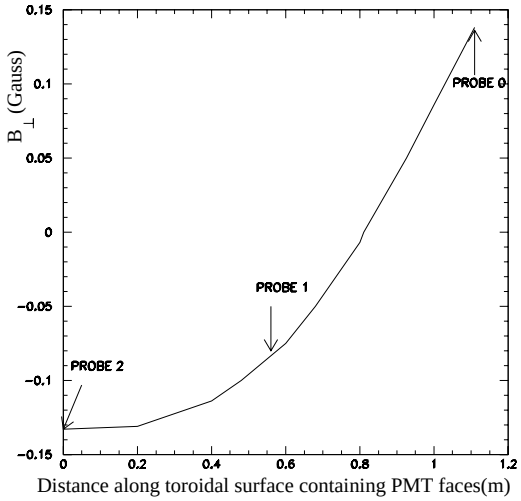

Figure 16. Results of the 2D model of *BABAR* using the measured permeability. The figure displays the $B_\perp$ along a surface containing the PMT faces from probe 2 to probe 0.

- that the shield should provide a stop for the backward plug against movements in the -z direction due to a seismic event.

To minimize the maximum transverse field at the photomultipliers an iterative series of axisymmetric studies of the structure were performed to determine optimum bucking coil current that would allow accelerator Q2 magnet operation. The principle parameters investigated were: the position of the bucking coil; the thickness, shape and permeability of the iron shield; the size of the magnetic gap between the shield iron, and the plug and SST; the dimensions of the support gusset; and the radius at which the shield inner cylinder connects to the outer shield.

A set of shield design parameters was derived from this exercise that predict that the magnetic field transverse to the PMT axis $B_\perp$at the PMT faces would be less than 0.2 G, as seen in Figure 16 (the three probe positions are defined in Section 4.3). This configuration requires a bucking coil current of about 30.7 kA-turns. The optimum to produce the lowest field at Q2 is higher by about 15 %, requiring a modest compromise.

Three-dimensional studies were made to exam-

ine the effects of the different non-axisymmetric aspects of the *BABAR* iron [18]. Due to the complexity of the *BABAR* magnetic circuit, it was not possible to make a 360° model within the computer memory limitations. Therefore, two models are considered, one with left-right symmetry and another with top-bottom symmetry.

The results of the 3D simulations show that the expected $B_\perp$ inside the DIRC shield is less than 1 G with angular variations of about ± 0.2 G. The $B_\perp$ for the left-right symmetric model varies between 0.3 G and 0.7 G as seen in Figure 17. Since a possible residual field was not included in the model, the measured azimuthal dependence can be different in detail from the prediction.

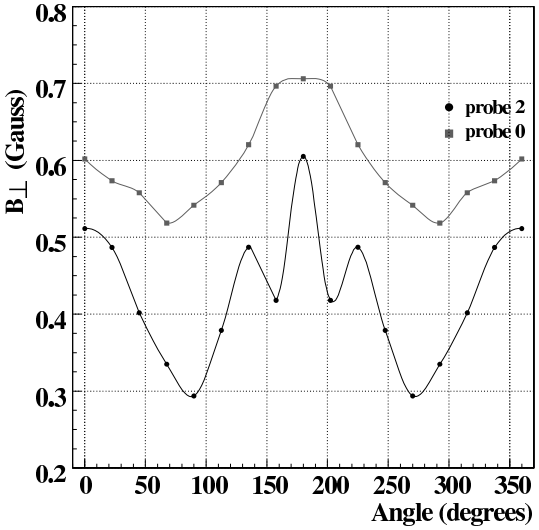

Figure 17. $B_\perp$ *vs.* azimuthal angle calculated in the left-right symmetry model of *BABAR*. The coordinate system has the downward direction at 0°.

In addition, the calculations show that in the case of a quench of the main solenoid or if power to the bucking coil is lost, the field in the shield iron can reach 7000 G instead of 500 G when both coils are on. The resulting coercive force is about 1 Oe for the very pure iron used in the shield construction. Therefore, the residual field of the iron would give an additional contribution to the fringe field in the PMT region.

The residual field distribution inside the shield was estimated using a simplified simulation. The value of the maximum perpendicular component at the PMT reaches about 3 G on the uppermost PMT and about 2 G on the lowermost PMT. In this model, the residual field due to the coercive force exceeded the expected fringe field inside the shield. This result led to a special effort to consider the use of the bucking coil to demagnetize the shield. In this method, the amplitude of the bucking coil current should vary about zero. It was predicted that about ten cycles of bucking coil current would be enough to decrease the residual fields to acceptable levels in a reasonable time.

4.2. Design and construction of the shield

The design of the shield is based on the following considerations:

- All connections are welded including the support structure, except for the cover plate and the flange on the fixed part of the inner cylinder to allow the opening of the SOB;
- since bending of the iron (required for some components) strongly affects permeability, especially at low H, the entire structure must be annealed after construction; the best results were obtained by using a temperature of 850 °C for 4 hours.

The construction of the shield was the responsibility of KHI. The ultra low carbon steel used was the proprietary material EFE, manufactured at Kawasaki Steel Corporation (KSC). The permeability and coercive force of the completed structure were measured at KSC and exceeded the specifications. Figure 18 shows the shield as it is being aligned and mounted, before mounting the SOB.

4.3. Design and construction of the magnetic field mapper

The DIRC mapper measured the field components inside the shield at positions corresponding to the faces of the PMTs [19]. It consisted of a rigid support structure, mounted on the SSA,

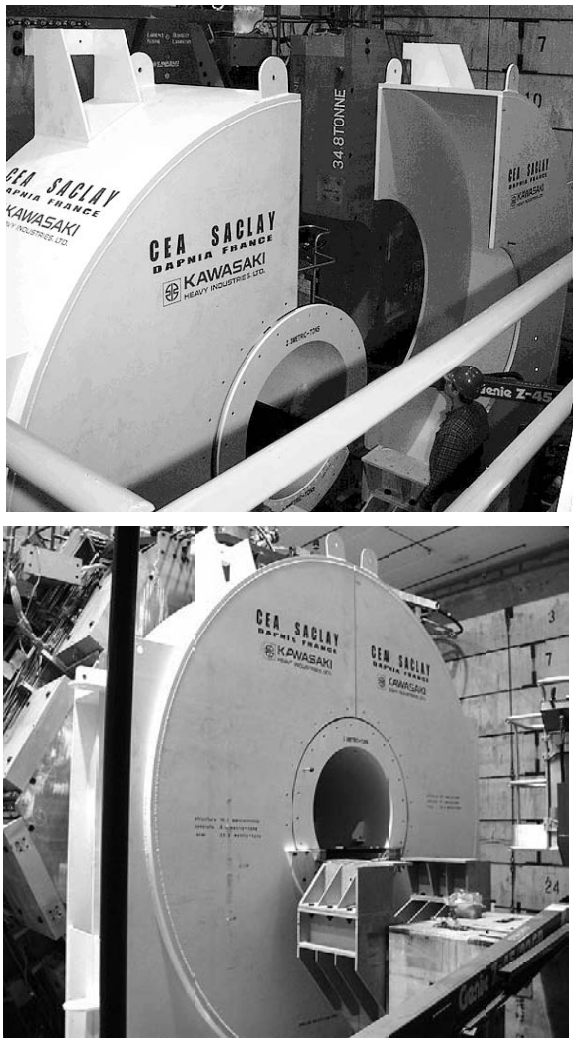

Figure 18. DIRC shield in the process of being adjusted (top). Shield fully mounted, except for the top of cover plate (bottom).

which can rotate about the beam axis. Three-dimensional probes were placed at three positions along the PMT rows, at the two extremes and in the middle.

Both ferro-probes (magnetically modulated permalloy probes) and Hall probes were used. Each set of 3D probes consisted of one 3D ferro-probe and one 3D Hall probe located next to each other. Ferro-probes were used to measure relatively low fields up to about 10 G. The long-term zero drift is less than 0.02 G within a 20 °C–30 °C temperature range. Hall probes were used to measure relatively high fields exceeding 5 G, thus overlapping the ferro-probe sensitive region. To measure the zero offset and sensitivities of the probes, a calibration was performed with the help of Helmholtz coils. The estimated error was 0.1 %.

4.4. Magnetic field measurements

To establish a baseline, mapper measurements were made with no solenoid field. The maximum remnant field in the *BABAR* doors, support gusset and skid plates was about 0.9 G. The mounting of the shield greatly reduced the influence of the remnant field at the PMT positions due to the *BABAR* doors. More importantly, a very low measured field (less than 0.2 G) demonstrated that the iron used in the shield construction had a very low residual field.

The solenoid and bucking coils were ramped together in 5 steps to the nominal operating currents. Measurements were made at each step.

At the nominal currents, the maximum component of the field at the PMT perpendicular to its long axis is 0.8 G, which is acceptable for PMT operation. The bucking coil current was varied to determine the optimum currents for PMT and quadrupole operation. It was increased to 230 A in 10 A steps and then was reduced back to 200 A. The current was then reduced to 170 A in 10 A steps. The optimum current for Q2 operation is near 200 A, and this value was chosen for the operating point.

The maximum value of $B_\perp$ at the PMTs differed in the two 200 A measurements due to hysteresis effects; in fact, it was reduced from 0.8 G to 0.6 G. At 170 A, the three probes had the same

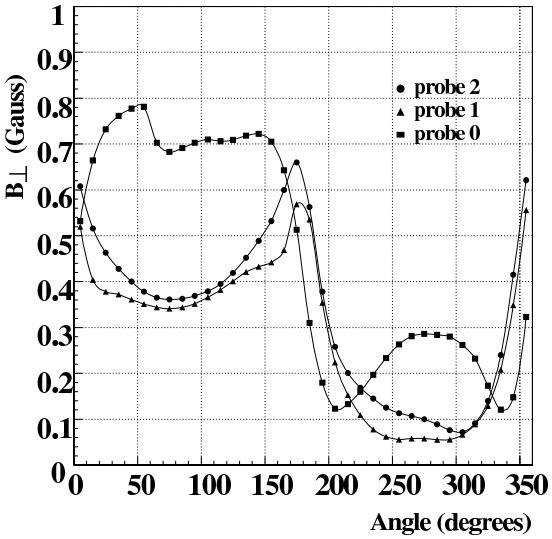

Figure 19. $B_\perp$ *vs.* azimuthal angle with the solenoid at its nominal current and the bucking coil at the optimum current for Q2, 200 A.

maximum value of 0.5 G, which is the optimum for the PMT. This value is about 15 % lower than that at 200 A, in good agreement with the calculation.

The bucking coil current was cycled back to 200 A as follows: 170 A → 230 A → 180 A → 220 A → 190 A → 210 A → 200 A at which point a reduction in the hysteresis was observed. Figure 19 shows the scan at the final 200 A current. The maximum $B_\perp$ is about 0.8 G and a left-right asymmetry is observed, probably due to residual shield magnetization. Various demagnetization schemes were developed successfully for the cases when either the main solenoid quenches or the bucking coil power is lost.

During normal *BABAR* operation the magnetic field in the SOB is monitored continuously by 12 probes in 4 locations.

5. Radiators

The radiator material of the DIRC is synthetic fused silica in the form of long, thin bars with a nominal rectangular cross section (17.25 mm × 35.0 mm). These bars serve both as radiators and as light guides for the portion of the light trapped in the radiator by total internal reflection. The individual 4.9 m-long bars, referred to as "long-bars" during the production process, are each made up of four shorter 1.225 m-long pieces, referred to as "short-bars", glued end-to-end. To each is attached a mirror on the forward end and a fused silica wedge on the backward (readout) end, shown schematically in Figure 20. The bars are placed into 12 hermetically sealed containers, called bar boxes. Each bar box contains 12 bars, for a total of 144 bars. A detailed description of bar boxes and the mechanical properties of the bars and their assembly is given in Section 5.4. This section describes some important properties of the component parts of the radiator, including material selection, fabrication, and quality assurance (QA) measurements.

5.1. Material selection

The primary requirements in the selection of the raw material for the DIRC radiators are radiation hardness, attenuation length, small chromatic dispersion, and the ability to allow an excellent optical finish.

The crystalline form of silicon dioxide (SiO_2), called quartz, is the second most abundant mineral on earth. However, quartz crystals are birefringent and thus are not suitable for use in the DIRC. An amorphous form of SiO_2, referred to here as natural fused silica, may be formed by crushing and melting natural quartz. This material possesses many of the properties required by the DIRC, such as long transmission length and good polishability. Unfortunately, the high level of impurities typically found in the natural quartz limits its usefulness due to the potential radiation damage. A third material, referred to here as synthetic fused silica, is formed artificially by burning silicon tetra-chloride ($SiCl_4$), or other feedstock, in an oxygen atmosphere. This material, which has been available for decades, can be made very pure and is widely used in the fiber optics industry. All of these forms of SiO_2 are colloquially called quartz, but, strictly speaking, this term only applies to the crystalline form.

Both natural fused silica and synthetic fused silica may be obtained from a variety of manu-

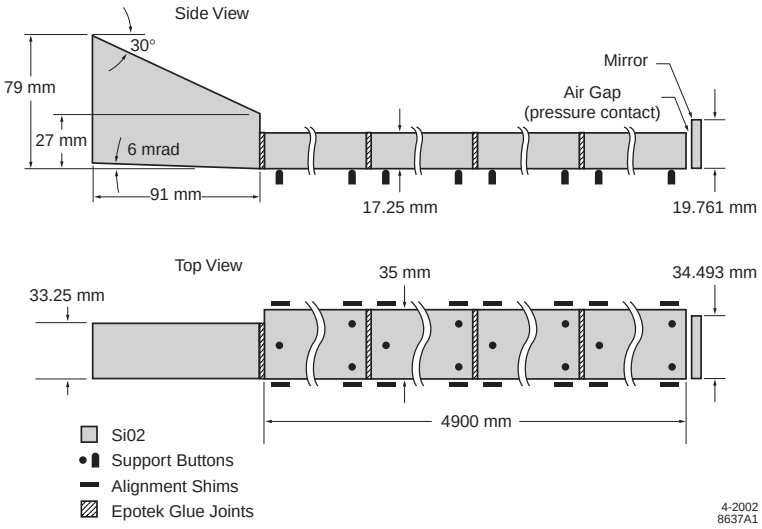

Figure 20. Schematics of a DIRC radiator bar in side and top view.

facturers. Tests were performed on several brands of natural fused silica, including Vitreosil-F [20], and synthetic fused silica, including Suprasil [21], Spectrosil 2000 and Spectrosil B [20].
The tests are described in detail in reference [11]: In the following list we summarize the main results.

- Tests using a Co^{60} source showed that natural fused silica materials can suffer from serious radiation damage to the transmission properties in the blue and UV regions after exposure to a radiation dose of 5 krad to 10 krad. It is expected that the DIRC will be exposed to 0.5 krad/year to 1 krad/year for the anticipated 10 years of *BABAR* operation.

  Although partial transmission recovery is possible using photo-bleaching and/or heating treatments, such "curing procedures" are not practical for *BABAR*. In addition, some of the natural fused silica materials tested exhibited radio-luminescence at room temperature. All synthetic fused silica samples were found to be sufficiently radiation hard for *BABAR*.

- The typical bulk transmission of both natural and synthetic fused silica material was found to be 98 %/meter or better over the entire wavelength acceptance of the DIRC.

- Some of the synthetic fused silica samples, made in the form of ingots, had periodic optical inhomogeneities. These inhomogeneities caused light that is transmitted down the length of the bar through a series of internal reflections from the sides, to produce a diffraction-like pattern that severely deteriorates the angular resolution. This was an extremely important discovery, since in some regions of photon phase space a DIRC made from such material would provide essentially no useful information.

Based on these tests, QPC Spectrosil 2000 was chosen as the material for the DIRC bars, wedges and windows. However, during the process in which Spectrosil 2000 was formed into cylindrical ingots, there was a tendency for large bubbles to occur, limiting availability on occasion. To compensate, ingots of Spectrosil B were used as a backup material.

Many other materials used in bar box construction were also subjected to a wide variety of tests; in the following list we summarize the most significant of them.

- All optical glue candidates tested were radiation hard at the level of at least 5-10 krads, thus sufficiently radiation hard for *BABAR*. In addition, no "yellowing" effects of the candidate glues under a strong flux of photons were observed. EPO-TEK 301-2 optical epoxy [22] was selected for the long-bar assembly.
- The reflectivity of the aluminum-plated mirrors was measured to be 92 % or better above 300 nm.
- An important requirement for the DIRC is that the bars must be held fixed within the bar box. This is done with a number of "buttons" that support the bars and shims that keep the bars separated from each other. The materials used for these supports should ideally have high reflectivity. Furthermore, since there can be relative motion between the bars and the bar box, the button material should not scratch the surface of the fused silica. Detailed tests showed that aluminum foil shims and nylon support buttons were suitable.
- All materials used in the construction of the bar boxes, including different candidate glues, O-rings, gaskets, shims and support buttons, were tested for outgassing. Each material was placed in a container both at room and at elevated temperatures, with and without added humidity, and dry nitrogen was flowed across the material and a test radiator bar. The bar reflection coefficient was measured continuously for several months. None of the materials tested caused a significant reduction of the surface reflectivity.

5.2. Component manufacturing

5.2.1. Production tolerances

The fused silica bars were produced by Boeing [12], the wedges by Cosmo [23], the windows by United Lens [24], and the mirrors by Custom Optical Elements [25].

The production tolerances, summarized in Table 4, were defined primarily by the physics performance goals of the DIRC system, specifically the Cherenkov angle resolution and the number of signal photons per track. The single photon Cherenkov angle resolution, for instance, is limited by such irreducible terms as size of PMTs, size of expansion region, and chromatic dispersion in the radiator material. Non-flatness and non-squareness of the bars cause the true Cherenkov angle to be smeared at every internal reflection. The magnitude of the resulting smearing term, and thus a limit of acceptable non-flatness and non-squareness, were determined from simulation. Early prototype bars for the DIRC were made of Vitreosil-F natural fused silica and manufactured by Zygo [26] with a surface roughness of about 3 Å rms. The coefficient of total internal reflection of those bars were measured to be 0.9996 ± 0.0001 at 442 nm wavelength [27]. Scalar scattering theory for smooth surfaces [28] predicts that the light loss due to surface scattering is proportional to the square of the surface roughness. With the selected bar size most Cherenkov photons will be internally reflected 200-400 times. Thus, relaxing the production tolerance to 5 Å was deemed acceptable while a surface polish of 10 Å instead of 5 Å rms would have led to a loss of half of the detectable photons.

5.2.2. Component production

The bars used in the DIRC were made from Spectrosil 2000 and Spectrosil B, two types of synthetic fused silica. The raw material was supplied in ingot form by TSL Group PLC [29] in England. The approximate ingot dimensions were 127 cm in length and 20 cm in diameter and the approximate weight was 90 kg. An ingot on the inspection bench is shown Figure 21.

The fabrication procedure is quite complex and was modified in a number of important ways as production proceeded and experience was gained. Though the basic geometrical requirements on surface figure are modest by optical standards, the required combination of elements, taken together, is very challenging to maintain in a production scale environment at modest cost. Some essential elements of good bars that provide particular challenges are (1) sharp edges, (2) excellent surface polish (< 5 Å rms), and (3) good side-to-face orthogonality (a goal of < 0.25 mrad).

Table 4
Production tolerances of DIRC radiator components.

Quantity	Specification	Primary Issue
	Bar Production	
Width	$35.000\ ^{+0.000}_{-0.500}$ mm	Mechanical
Thickness	$17.250\ ^{+0.000}_{-0.500}$ mm	Mechanical
Length	$1225.000\ ^{+0.000}_{-0.500}$ mm	Mechanical
Surface Roughness	better than 5 Å rms on sides and faces better than 20 Å rms on ends	Surface reflectivity Photon loss
Surface Flatness	flat to 0.1 mm over entire length	Angle smearing
Edge Sharpness	total area of chips less than 6 mm^2 per side	Photon loss
Squareness	0.25 mrad; rms of side-to-face angles better than 0.4 mrad	 Angle smearing
Parallelism	parallel to 25 μm across the bar length	Angle smearing
	Mirror Production	
Width	$34.493\ ^{+0.000}_{-0.254}$ mm	Mechanical
Height	$19.761\ ^{+0.000}_{-0.254}$ mm	Mechanical
Thickness	$3.000\ ^{+0.000}_{-0.254}$ mm	Mechanical
Reflectivity	better than 92 % above 300 nm	Photon loss
	Window Production	
Length	437.00 ± 0.01 mm	Mechanical
Width	124.00 ± 0.01 mm	Mechanical
Thickness	9.576 ± 0.005 mm	Mechanical
Flatness	flat to 2.5 μm	Mechanical, gluing
Parallelism	parallel to 2.5 μm	Mechanical, gluing
	Wedge Production	
Length	91.00 ± 0.2 mm	Mechanical
Height	79.00 ± 0.01 mm 27.00 mm (reference)	Mechanical Mechanical
Width	$33.25\ ^{+0.00}_{-0.45}$ mm	Mechanical
Surface Roughness	20 Å	Surface reflectivity
Angles	60 degrees ± 1 minute of arc 90 degrees ± 1 minute of arc 6 mrad ± 1 minute of arc	Angle bias Angle bias Angle bias
Bevel	1 mm on 60 degree edge	Gluing

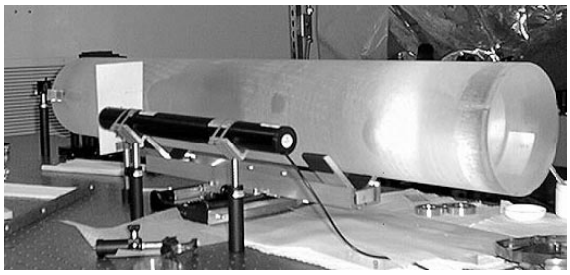

Figure 21. Spectrosil 2000 fused silica ingot.

In general terms, to obtain these basic elements in a production scale process, all large surfaces are ground on numerically controlled machines, lapped on a soft iron wheel, and then pitch polished on a 4 meter planetary pitch polisher. To avoid edge chips, all edges are processed either while protected by a neighboring bar, or with a glass plate glued onto the end of the bar temporarily. Constant attention to detail in measurement and quality assurance (QA) is an essential element of the process. Full QA measurements were made throughout the process, and production units were reprocessed if they failed the specifications. Final QA measurement results are available for all the bars produced. The following description highlights some of the basic methodology of the process used for the majority of the bars.

After ingot QA, the ingots were sliced into 2-bar planks (units 1.95 cm $\times$ 7.8 cm $\times$ 124 cm) using a band saw for the long dimension and a chop saw for the ends [30]. The two large face surfaces of these planks then passed through the surfacing process (grind, lap, and polish) described above. At the end of this process the planks had two high quality parallel faces with excellent surface polish. Four planks were then held by fixtures and glued together using a heat setting wax. The surfaces of the outer two planks were covered with glass planks for protection of the polished faces and edges. The two sides of these 8 bar units passed through the surfacing process again. Then, they were sliced on a band saw, and the final side surface of each of the 4 bar sub-units produced was passed through the surfacing process. Great care was taken to maintain the required face-to-face (side-to-side) parallelism and side-to-face orthogonality at each of these stages. At the end of this stage, all of the long surfaces had been completed. Finally, eight of the 4 bar units were glued into a 32 bar unit for the end processing. The complete unit was ground to length on a custom grinder, and then placed upright on an over-arm custom built lapping-and-polishing machine to finish the ends to better than the required 2 nm rms surface finish. After disassembly, and final QA, the bars were carefully cleaned, and packed in specially designed units for shipping. A total of over 600 high quality fused silica bars were manufactured to our specifications (the DIRC contains 576).

The fused silica wedges and windows were produced from the half-moon shaped pieces that were cut from the ingots in the first stage when the planks for the bar pieces were sawed. The basic issues for the production of the wedges and windows are similar to those of the bar fabrication process. However, the surface figure, polish, and edge quality requirements are substantially less severe allowing a wider choice of vendors. The pieces are first cut to rough size, ground to specifications, and polished.

5.3. Quality assurance (QA) and component testing

5.3.1. Fused silica ingots

Most Spectrosil 2000 ingots contained gas inclusions in the form of typically one or two large bubbles with diameters of 5-15 mm. To determine the potential yield for bar production, we mapped the location of every bubble and provided the bar manufacturer with a template to show how the ingot was to be cut. The presence of the periodic optical inhomogeneities was checked for each ingot with a He-Cd laser. In order for the laser beam to traverse the ingot at angles that are interesting for the propagation of Cherenkov photons in the bar, it was necessary to send it first through a fused silica wedge, coupled with optical coupling gel to the ingot, and have the beam exit through a fused silica window, similarly attached to the ingot. None of the ingots showed any periodic optical inhomogeneities at angles that are internally reflected in DIRC bars.

5.3.2. Radiator bars

The primary quality assurance was performed by the bar manufacturer, Boeing [12], who made all QA results available to us. When a shipment of bars was received, a sample of bars was selected and measured to crosscheck the data provided by the manufacturer.

Boeing measured all bar angles using a micrometer-based fixture (occasionally calibrated with an autocollimator) with a precision of about 0.02 mrad. Acceptance of bars for use in the DIRC was determined by the following statistical procedure: a bar was accepted if all face-to-side angles were square to 0.25 mrad. If one of the angles failed that criterion all four face-to-side angles on both sides of the bar were used to calculate the rms of the eight values. The production tolerance was 0.4 mrad for the rms of the eight values, with a goal of 0.25 mrad in each angle.

To determine the mean surface roughness, Boeing used an interferometer on each side across an area of about 1 cm^2 with an error of less than 0.1 nm. Figure 22 summarizes the QA data obtained by Boeing: it shows the surface roughness on the faces, sides and ends as well as the rms of the eight orthogonality angles. Bars with a surface roughness of less than 7.5 Å on the sides were accepted.

Edge damage and bar orthogonality angles were measured using a digital microscope; software was used to analyze the digital image [11]. A comparison of the differences in side-to-end and face-to-end angle measurements, using our method and the Boeing method, yielded a fitted error of less than 0.15 mrad; this demonstrated that the two methods were consistent. The accuracy of the manufacturer's data was verified further by measuring all bar dimensions and angles for several bars on a precision coordinate measurement machine (CMM). The values of our microscope data, the CMM values and the measurement from Boeing were found to be in good agreement; which provided confidence in the measurements from the company for the rest of the bars.

Figure 23 shows an example of a good and bad bar edge as seen by the microscope and the corresponding edge analysis result. Once bar production began, all of the bars easily passed the requirement that the total area of edge chips be less than 6 mm^2. The primary control used at Boeing for this specification was visual inspection and comparison to a bar of good quality.

Although the production surface polish and QA at Boeing was specified in terms of rms surface roughness, the corresponding quantity of importance to DIRC is the surface reflectivity. Thus, instead of measuring the surface roughness directly, the transmission and surface reflectivity of finished radiator bars were measured at SLAC by scanning the bar with a laser beam at 325 nm and 442 nm. While the transmission was measured with the laser beam parallel to the long axis of the bar, the reflection coefficient was determined by allowing many internal reflections of the beam within the bar. Figure 24 shows an example of measurement results for 30 bars at 442 nm [11]; the average relative internal reflection coefficient was 0.9997 ± 0.0001, the average transmission was 99.9 ± 0.1 %/meter. At 325 nm the average transmission was 98.9 ± 0.2 %.

Due to the modifications to the fabrication procedure discussed in Section 5.2.2, bars were accepted even when the width and thickness were outside the production tolerances listed in Table 4. The width and thickness of each bar were measured with calibrated calipers immediately prior to the bar box assembly stage. The average thickness and width of the accepted bars was 16.88 mm and 34.54 mm, respectively.

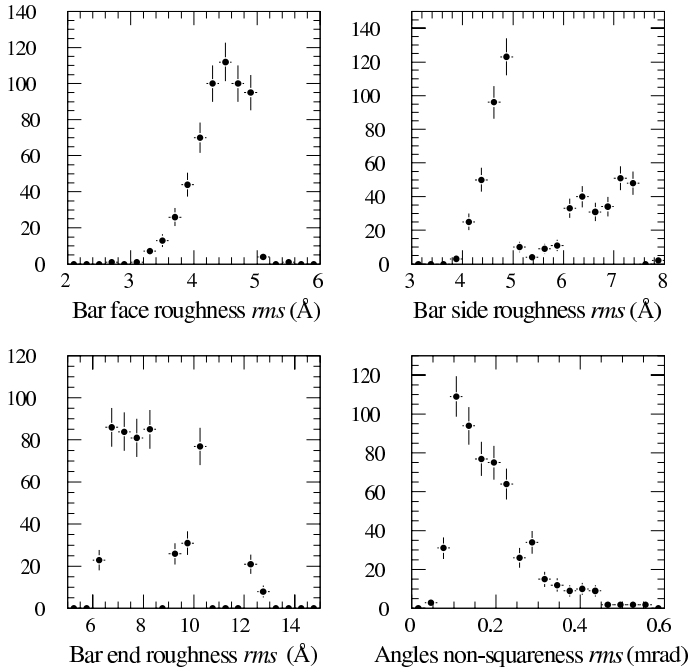

Figure 22. The surface roughness and angle measurements made by Boeing for all 576 bars used for the construction of the DIRC.

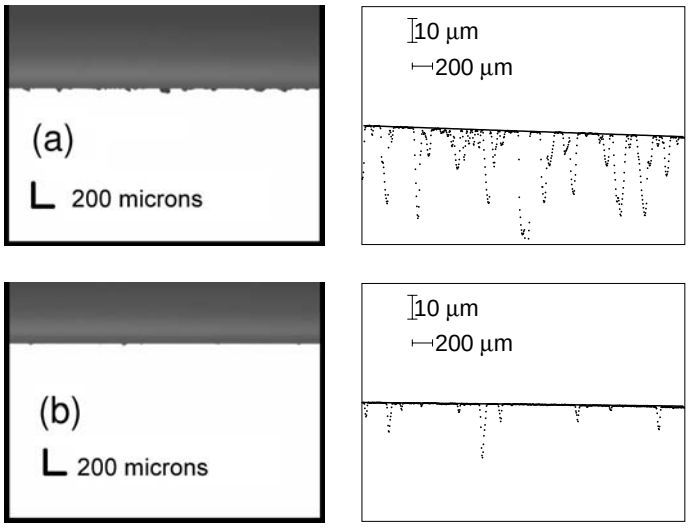

Figure 23. Example of (a) bad bar edge, as it appears on the computer screen used for the microscope readout (left side), and the digitized version of the same edge displayed by the off-line software analysis (right side), and (b) the same for the good bar edge, which was typical. The digitized plots have been greatly magnified in the y-direction.

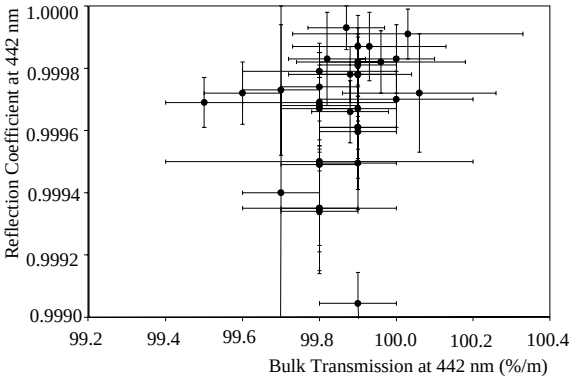

Figure 24. Measurements of transmission and internal reflection coefficient at a wavelength of 442 nm.

5.3.3. Wedge and window QA

The primary concern in the QA of the wedges and windows was to verify that the mechanical dimensions of the pieces were within tolerances so that the long-bar assembly could proceed. The width, thickness and height of each piece were measured with calibrated calipers. Some wedges and windows were tested by shining a He-Cd laser through the pieces at steep angles. No diffraction patterns due to the periodic optical inhomogeneities were observed. For several wedges, all dimensions and angles were measured using a precision coordinate measurement machine. In all cases, the measurements agreed well with the manufacturer's data. Finally, the quality of the surface polish on the wedges was verified by measuring the coefficient of total internal reflection using a He-Cd laser setup similar to the one described in the previous section.

5.3.4. Pre-assembly QA

Before the 1.225 m-long short-bars were glued, the width and thickness of each piece was measured using calibrated calipers to ensure that the lengths of resulting long-bars were as uniform as possible. After the bars were glued and installed in the bar box, the bars were visually inspected and a He-Ne laser beam was used to verify that all glue bonds were intact. Low intensity reflections from the glue joints were observed. The intensity of these reflections was dependent on the incident angle of the beam since EPO-TEK 301-2 optical epoxy has a refractive index that is a good but not perfect match to that of the synthetic fused silica. This causes a small loss of Cherenkov photons in the DIRC, particularly at large incident angles [31].

5.4. Bar box assembly design

A bar box is a mechanical assembly that must provide a clean, mechanically stable support for a group of 12 bars, which is as thin as possible when measured in radiation lengths. It provides the seal between the water of the SOB and interior of the box at the backward end of the detector, and must be reasonably gas tight to prevent water vapor condensation on the bars that would destroy the total internal reflection of the Cherenkov light.

Ideally, the long-bars would be supported solely by kinematic mounts within the bar boxes. However, because of their extreme length to width ratio, the long-bars must be supported at multiple points along their length. These supports are arranged to keep each long-bar in a straight line, minimizing any torque that might bend the bars or put stress on the glue joints between the short-bars. This is accomplished within the bar box by spring loaded buttons to push the bars against precisely aligned, fixed bumpers on the bottom, side and end. This support mechanism allows for differential expansion between the silica and the mostly aluminum support structure under a temperature change of $\pm$ 20°C, the maximum anticipated variation during transportation and installation. The spring loading also insures that glue joints are generally kept in compression during normal handling, operation or earthquakes and that the bars do not move around inside the bar box during transportation.

A schematic diagram of a bar box is shown in Figure 25. The bar box consists of three sections: a) the active region, b) the mirror end, and c) the window end, including the water seal. These regions are built mostly of aluminum honeycomb materials and thin extrusions, or, in the case of the mirror end, solid aluminum pieces that have been machined to remove as much material as

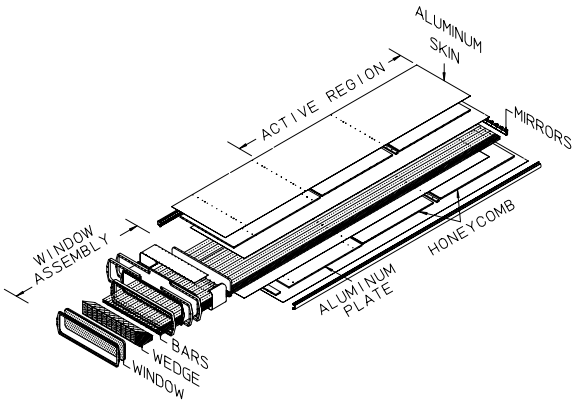

Figure 25. 3D schematic drawing of a bar box showing the active region, mirror end and window ends

possible.

During installation a bar box may be rotated at any angle about its long dimension with respect to the direction of gravity, consequently it must be supported under a variety of load conditions. Within the CST and SSA the bar boxes slide into their slots on 16 wheels (or cam-followers) that align with the four tracks of the CST and SSA (see Section 3.3). There are eight pairs of wheels built into one cover of the bar box, and eight pairs of cam-followers on the opposite cover. The wheels and cam-followers are similar, but the cam-followers rotate about an axis perpendicular to the axis of the wheel rotation, to locate the box with respect to the broader width dimension (azimuthally).

For bar boxes where the broad dimension (429 mm) is nearly horizontal, most of the weight is carried by the wheels, and the cam-followers just help to guide the bar box into their slots. For the bar boxes where the broad dimension is nearly vertical, the role of the wheels and cam-followers is reversed, with the cam-followers carrying most of the weight. Since the wedges at the backward, instrumented, end always point radially outward, the bar boxes are *almost* identical, with the exception that the cover with the wheels (or cam-followers) changes sides of the bar box with respect to the direction of the wedge depending on whether it is in the lower half (bar boxes 3–8) or upper half (bar boxes 0–2 and 9–11) of the DIRC. A further mechanical complication due to the gas supply and return lines breaks the symmetry of the boxes in the vertical plane. To accommodate these conditions requires four distinct types of bar boxes in the full detector.

To ensure that the bars are kept free from condensation, nitrogen gas is introduced through a small 3 mm diameter tube that runs from the window end, along the outside of the bar box to the mirror end, where it is introduced into the bar box. From there it flows along the bars back to the window end and exhausts into a return line for analysis (the gas system is described below). To avoid excess pressure inside the bar box, the gas pressure is set to less than 20 mm water equivalent. Each bar box is equipped with a custom pressure relief value that will open fully at a pressure of 250 mm water equivalent.

The details of the active region, the mirror end and the window end of the bar box are discussed below.

5.4.1. Active region

A cross section through a bar box in the active region of the detector is shown in Figure 26. The support of the short-bars within the bar box assembly is designed to minimize the force on the glue joints of the long-bar assemblies. The force is minimized when the short-bars are supported such that under their own weight their ends would be in a vertical plane. This condition is satisfied when the supports are located at a distance $z = 0.211L$ from each end of a bar of length L. The sections of the load buttons and bumpers in contact with the bars are made from nylon or teflon, and were tested extensively to assure that they do not damage the surface of the bars.

In the azimuthal direction (perpendicular to the 429 mm $r\Delta\phi$ dimension of the bar box), the bars are pressed against two fixed nylon buttons by a spring-loaded bumper on the opposite side of the bar. This combination of a bumper plus two opposing buttons is repeated at eight locations along the length of the long-bar. The height of the fixed bumpers was set to $\pm$ 25 μm by suspending the cover a known distance above a flat,

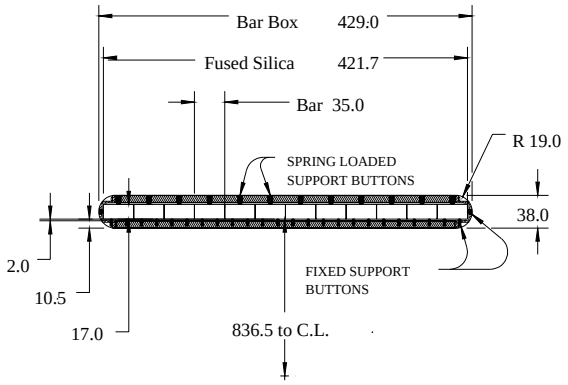

Figure 26. Cross section of a bar box in the active region of the detector. All dimensions are in millimeters.

granite table and pressing the bumpers against the surface of the table. The bumpers were then glued [32] into place under vertical load to keep them in contact with the granite surface as the glue cured. The fixed bumpers are threaded on their circumference to provide a good mechanical joint between the plastic bumper and the aluminum cover.

Threaded nylon bumpers are used also to support the bars from the extruded aluminum side rails (*i.e.,* forces parallel to the azimuthal direction). Flexing of the side rails due to the load applied through the bumpers is large enough to supply the spring load for the bars in this ($r\Delta\phi$) direction.

Maximizing the geometrical acceptance of the bars implies minimizing the separation between the bars within a bar box. The bars must lie as close as possible, but not touch each other. Loads applied perpendicular to the length of the bars must align with supports, since the bending of the bars under an applied torque as small as 1.5 N·m, offset by 10 mm from the nominal support point in the z direction, will cause neighboring bars to touch between the support points. The bars are separated from each other by shims made of folded 50 μm aluminum foil (described below).

5.4.2. Mirror end

To reflect the forward going Cherenkov light to the backward, instrumented, end requires a mirror at the forward end of the long-bars (Figure 25). At the front surface of the bar a spring-loaded, front-surface mirror (aluminum coating on glass) is placed against the end of the bar, without glue or coupling compound, to reflect the Cherenkov light back to the instrumented end. The reflectivity of the mirror is about 93 % in the wavelength region of interest for the DIRC (see Section 10.2.1). The mirror assembly is shown in Figure 27.

The load applied to keep the mirror next to the end of the bar must satisfy two additional requirements. The load must be high enough to resist earthquake loads (up to 1.6 times the weight of the bars), and to keep the glue joints in compression. Additionally, this spring load, transmitted from the mirror end to the window end via the bars, helps to support the window against the pressure of the water in the SOB. This is about 1500 N for boxes 5 and 6 at the bottom of the detector. The assembly procedure for installing the mirror is described below.

5.4.3. Window end

At the window end of the bar box (Figure 25), inside the volume defined by the SOB, the bar

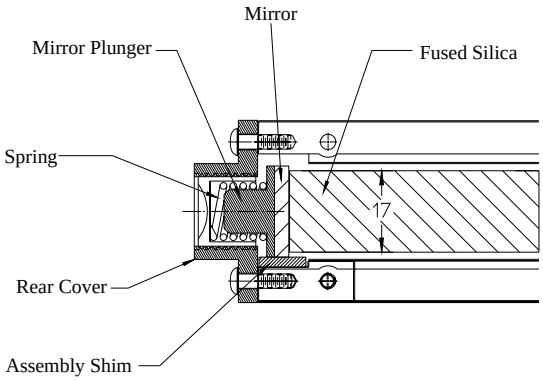

Figure 27. Cross section through the mirror end of a bar box. It shows the end of a radiator bar, an aluminum-on-quartz mirror, and a spring-loaded plunger.

box expands outward in the radial dimension to create an enclosed volume for the wedges. All 12 wedges are glued to a common 10 mm thick fused-silica window that forms the interface between the silica bars and the water of the SOB. The window itself is captured in a stainless steel window frame and made water tight by rubber gaskets that are compressed on both its forward and backward surfaces. All fasteners exposed to the de-ionized water inside the SOB are gold-plated stainless steel.

The window frame is attached to the bar box via a stainless steel "wedge cover". This is a sheet metal assembly fabricated from six parts joined with epoxy glue backed-up by metal screws. These parts are added to the bar box assembly after the window has been glued to the wedges (see below). The wedge cover, and hence the bar box and the slot in which the bar box rests, is kept water tight by a custom made, EPDM rubber diaphragm [33] that seals to grooves cut in the window frame and the AF of the SSA. A photograph of the assembled window end of the bar box is shown in Figure 28.

All bar boxes were pre-assembled without bars, and the pieces match-marked. The two aluminum extrusion side rails were glued [32] to the lower cover, as well as the fixed bumpers and wheel/cam assemblies. The entire bar box package was shipped from the box assembly site to the radiator installation site in one of two special containers, each capable of holding four bar boxes.

Figure 28. End view of the window of a bar box showing the window-frame, fused-silica window and twelve wedges.

5.5. Radiator bar gluing and bar box assembly

5.5.1. Radiator bar gluing alignment fixtures

As information about the emission angle of the Cherenkov light must be preserved as it reflects down the bars, angular misalignments of the bars must be minimized. To avoid unacceptable biases in the angle reconstruction, the bars must be parallel in the z direction to less than 20 μrad. The long-bar assemblies must lie next to each other inside the bar box with only $\approx$ 150 μm separating the long-bars over their 4.9 m length. This means that the five components of a long-bar, a wedge and four short-bars, must be aligned precisely during gluing.

The gluing process is complicated by the fact that the epoxy glue [22] chosen takes 48 hours to cure, so the bars must be held securely at nearly constant temperature and orientation for two days for each gluing cycle (three gluing cycles are required per long-bar, see below). The glue joint between two short-bars or short-bar to wedges is set to be 25 μm thick. Tension tests of sample glue joints indicated that at this thickness the glue joint was stronger than the fused silica ($\geq$ 6.8 MPa). In all glue joints between bars (or bar to wedge joints) the glue is introduced into the joint by applying a few drops on top of the joint and allowing capillary action to draw the glue into the void between parts. Typically it takes about one hour for the glue to flow completely into the joint. After 8–10 hours, the excess glue is removed. The joints are cleaned after 24 hours of curing, and the glue is completely cured after 48 hours. During this 48 hour process, it is imperative that the space between the bars be held at 25 μm. Although the clean room temperature is typically held to $\pm$ 2°C, even this temperature variation could open the joints by 50 μm due to the differential expansion of the fused silica bars and the gluing table. Hence, in

Figure 29. A bar assembly station showing a set of six bars with wedges already attached.

any set (or sub-set) of bars being assembled there is only one "active" glue joint at a time, and the bars are only clamped longitudinally directly next to the "active" joint.

It is critical that the bar surfaces not be damaged by contact with metal parts, consequently the fixtures used to align the bars were manufactured so that only plastic bumpers (typically nylon or teflon) came into contact with the bar surfaces.

The first glue step involves gluing the wedge to the end of a short-bar. This is done in a set of six specialized glue fixtures, so two glue-cycles are necessary to produce twelve wedge/short-bar assemblies. The next two glue-cycles involve gluing the short-bars together to form long-bars. During these two glue-cycles the short-bars are clamped in two duplicate sets of gluing fixtures, each set capable of holding simultaneously seven long-bars. Within each set of glue fixtures, there is an array of 2×7 clamps at each of the three joints necessary to glue 28 short-bars into seven long-bars.

All gluing fixtures are mounted on a six meter long optical table and all 12 long-bars per bar box can be glued during the same gluing period, with room for two spares.

Figure 29 shows an example of several bars clamped into a gluing station. The vertical heights of the fused silica bars at the glue joint are defined by plastic bumpers that are glued into the fixture, then ground to a common height to a precision of $\pm$ 3 μm. The bars are clamped vertically at the joint during gluing. Small ($\approx$ 25 μm) misalignments can be tolerated if they are common to all bars and as long as the bars "nest" together inside the bar box. Hence, the following two step strategy was developed to fabricate the glue fixtures: 1) the plastic bumpers that locate the bars transverse to their length were glued into the fixtures by pressing them against a template manufactured to $\pm$ 2.5 μm. All glue stations were manufactured using the same template, so any small, residual errors in the template are common to all joints. A solid joint between the nylon bumpers and the aluminum substrate of the fixtures was guaranteed by using threaded nylon rod for the bumpers, the latter rounded at the end in contact with the fused silica.

Once these bumpers are glued into the individual clamping fixtures, the second step is to align the clamping fixtures on the gluing table. These fixtures are aligned over the 4.9 m length of the long-bar assemblies by positioning them under a microscope with a 100 μm diameter tungsten wire stretched the length of the table to act as a straight edge. A subsequent survey of the fixtures using traditional optical survey equipment found no deviation from straightness to the $\approx$ 25 μm level of precision of the survey.

5.5.2. Installation of long-bars into the bar box

Once 12 long-bars were glued together, the next step was to insert them into the bar box following a well-defined procedure. Critical as-built dimensions were recorded for later input into the detector geometry database and comparison with results obtained from colliding beam data.

The bar box was prepared by adjusting it on a transport frame resting on a granite table. The bar box was leveled to $\approx$ 25 μm precision at a matrix of eight locations along its length and two locations across its width (16 points in total) with respect to the surface of the granite assembly table. Next the eight side-load buttons were adjusted to the appropriate depth, based on the

measured total width of the fused silica bars intended for that box. These buttons were brought into alignment with each other by adjusting them with respect to a tungsten wire stretched the full length of the bar box. At the wedge end of the bar box a set of 12 dial indicators were positioned. These were used to measure the longitudinal position of the bars. The bar box was then ready to accept bars.

The first operation was to transfer the individual long-bars about three meters from the gluing table to the assembly table. This was accomplished by a custom, light weight crane that ran on two trollies suspended from the ceiling. The crane was attached to the long-bar with the 4×2 plastic holders that had been attached to each individual short-bar as part of their initial quality control procedure. Once the bar was transferred to the assembly table, these plastic holders were removed. The bars were lifted by hand (4 persons working together) cradling the bar with eight mylar strips as it was lifted from the table and into the bar box. This bar was then pushed ≈ 40 mm laterally against the eight fixed side-load buttons, where it is trapped above and below by the side extrusion of the bar box. Finally, the long-bar was adjusted by hand in longitudinal position so the 32 mm $\times$ 91 mm face of the wedge was in the correct location to $\pm$ 12 μm.

The second bar was inserted into the bar box in a fashion similar to that for the first bar, except that prior to pushing it against the first bar, it was equipped with the eight custom shims to establish the gaps between itself and its two nearest neighbors. These shims were located at the same point along the bar length as the fixed side supports, so that there were no bending moments due to offset supports. The nominal shim thickness was 150 μm, made from a piece of 50 μm thick aluminum foil cut in the shape of an "H", where the cross bar of the "H" was slightly larger than the 35 mm width of the bar. The two legs on each side of the "H" were each folded over to form a 150 μm shim, while the cross bar of the "H" supported the shim across the top of the bar. Thicker shims could be made by using thicker aluminum foil, or by inserting discrete shims into the folded aluminum shim package.

Ideally, all four bars used to construct a single long-bar were to have the same 35 mm transverse dimensions to $\pm$ 25 μm. Operationally, however, these tolerances were not held by the manufacturer, and the width of each bar had to be measured and a custom shim fabricated to fit. The widest bars were used in the fiducial volume of the detector, and the narrower bars were used close to the readout end. This approach maintained the full fiducial coverage of the detector, at the cost of slightly reduced ($\approx$ 3 %) light yield due to the mismatched sizes. To allow for variable width short-bars in the same long-bar assembly, the width of each short-bar was measured and stacks of spacers, up to 1 mm thick, were added to nominal 150 μm aluminum shims between bars to account for the missing material.

The bars were inserted into the bar box in the following order from the reference edge: 1–9, then 12, 11, 10. The order of the last three bars is inverted because the 12th is trapped by side extrusions and cannot be installed from above. There was adequate space in the bar box to insert the last bar (10, from the reference edge), and still remove the mylar strips used to support it as it is moved from the table top into the bar box without disturbing the shims already installed on bar 11.

After all twelve bars were inserted into the bar box, the side load buttons opposite the reference edge were slightly tightened. At this stage, a 75 μm shim was passed in the gaps between all the bars to insure they were not touching.

Next, the front surface mirrors were applied to the ends of the bar opposite the wedges. Each mirror was temporarily held with two drops of UV curing glue [34] at the top edge. After all twelve mirrors had been "tacked" to the bars in this fashion, the end cover of the bar box was installed, and the spring-loaded end plungers were lightly tightened against the mirrors to hold them in place.

The top cover was then applied. A final check of the longitudinal position of the wedge faces was made; bars out of position by more than $\pm$ 12 μm were adjusted. With the top cover installed, the side load buttons were tightened to their final load (1.5 times the weight of the bars in each

direction). If any bar moved more than ± 12 μm during this process, the side load buttons were loosened, and the bar repositioned. This procedure never had to be repeated more than three times, and was successful on the first try about half the time. After tightening the side load buttons, the top load buttons were tightened equalizing the vertical load on the bars according to an algorithm that included the bending of the cover. Typically tightening these top-load buttons did not cause the bars to shift longitudinally.

Twelve bars could be inserted into the bar box in about seven hours, including one hour to install the mirrors and two hours to install the top of the bar box and adjust the top load buttons.

5.5.3. Window gluing

The most difficult task in the assembly of the bar box was to glue the fused silica window simultaneously to the twelve wedges at the readout end of the bars. The procedure was developed over three months of testing with glass and natural quartz substitutes, and success depended critically on the cleanliness of the window. Dust or residue on the window or wedge surfaces would prevent the glue from flowing properly and would lead to bubbles in the glue joint.

Using a custom fixture, the wedges were pushed up or down so that their front surface was perpendicular to the surface of the granite table, as measured by a pair of dial indicators, separated by about 6.4 cm, that had been adjusted previously using a precision square. The tolerance on the perpendicularity of the wedge faces to the table was ± 12 μm from zero indicated on each dial indicator.

After the wedges had been adjusted for perpendicularity, the indicator fixture was removed, and the window frame components installed. The window frame components were leveled with respect to the bar box, and became part of the fixture for gluing the window to the wedges.

The cleaned window was positioned next to the faces of the wedges using extension rods that supported the window from the frame. The window was spring loaded against the twelve wedges with a set of six 75 μm shims separating them (two shims on each end, and a pair at the edge near the center of the window). The window was placed at a known height with respect to the exterior of the window frame, and centered horizontally on the frame with shims whose thickness was calculated from the "as-built" dimensions of the window.

Using the same epoxy glue and a technique similar to that for the bar-to-bar joints, drops of glue were applied to the top of the twelve wedges, and the glue allowed to flow down between the wedge faces and the common window via capillary action. During this process it was imperative that the glue not form a joint between neighboring wedges, since this might allow light to leak from one wedge into a neighbor. For this reason, the wedges were made typically 2 mm narrower than the bars to avoid the glue being drawn between the wedges by capillary action.

After the glue had flowed from the top to the bottom of the wedges (about 1.5 hours), the 75 μm shims between the window and wedges were removed. Subsequently, the window was drawn by the surface tension of the glue to within 25 μm of the wedges, a separation that was maintained by clamps until the glue had cured. Tests of the strength of the glue joint formed using this procedure indicate it is as strong as the bar-to-bar joints. After the shims were removed, the excess glue was removed about 8 hours later, and the glue was allowed to cure for a total of 48 hours. Typically, each wedge glue joint would have zero to three small bubbles, 10 μm to 15 μm in diameter, over the 32 mm × 91 mm surface.

After a final visual inspection, the window frame was clamped to the window, and the covers that surround the wedges were screwed and glued into place, connecting the window frame to the rest of the bar box.

5.5.4. Bar loading and gas sealing

After the epoxy holding the window frame elements had cured, the spring plungers on the mirror end of the bars were tightened to a load of 1470 N. Next, the gas connections to the bar box were installed; a 3 mm diameter supply line from the wedge-end to the mirror-end was glued into pre-machined holes in the forward and rear assemblies.

All screw adjustments penetrating the bar box

were covered with aluminium strips and sealed with epoxy glue [35] to prevent gas leaks. The gaps between the cover and the body of the bar box were sealed from the outside with epoxy. The integrity of the bar box was tested by filling it with gas, and requiring that it held a pressure of 12 mm water column equivalent.

Opening a fully sealed bar box is considered a destructive operation, and it is unlikely the mechanical parts from an opened bar box could be salvaged. Parts for two spare bar boxes were constructed.

It took about 13 working days for the complete assembly process for one bar box, from gluing the bars together to final gas sealing of a bar box. The majority of this time was eight days to make up the wedge-to-bar and bar-to-bar joints. Since gluing the wedges and bar-to-bar joints of one bar box could proceed partially in parallel with the assembly of another it was possible to assemble about one bar box per week. In practice, the construction of the bar boxes was limited by the supply of the short-bars from the vendor.

5.6. Bar box installation into *BABAR*

Once the bar boxes had been fully assembled, they were stored on racks in a temperature controlled environment until they were needed for installation. Transfer of the bar boxes from the clean room to the storage facility was accomplished with a specially constructed A-frame crane, using a custom lifting fixture that encircled the bar boxes and supported it at an array of 2×5 points along its length.

Bar boxes in the lowest section of the detector (numbered 4–7) had to be installed before the detector was moved onto the beam line, because their installation conflicted with the fixed concrete supports of the accelerator components. The other bar boxes could be installed on beam line, and this was done for the upper eight bar boxes.

Once a bar box was identified for installation it was removed from the storage facility using a fixture that would eventually double as the installation fixture for the bar boxes into the *BABAR* detector. This fixture allowed the bar box to be rotated to the same plane as the slot in the support structure, incorporated a rail system to support the bar box as it was slid into the slot, and a laser alignment system (described below).

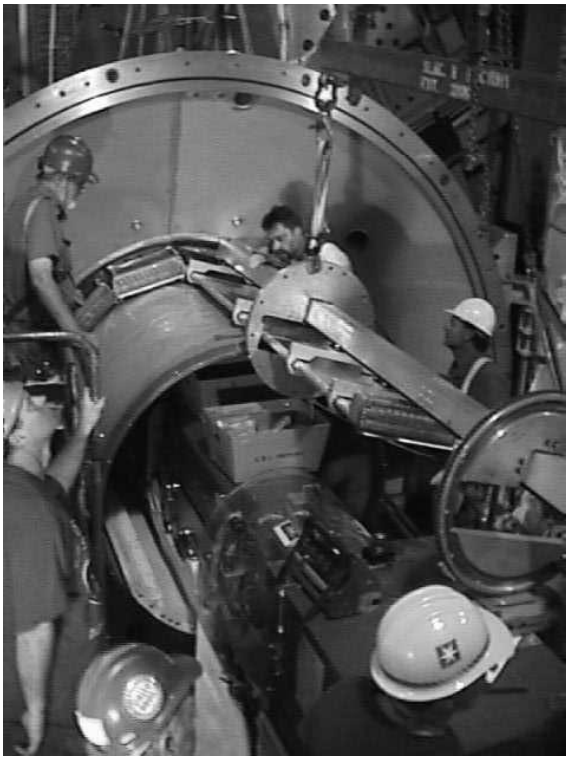

Figure 30. Installation of a bar box into the *BABAR* detector. Not seen in the figure is the cantilevered support arm which supports the installation fixture above the accelerator components.

Installation of the upper eight bar boxes into *BABAR* was complicated by the presence of the accelerator components, which for some bar boxes came within 1 cm of the path of the bar box. The installation fixture was held above the accelerator components using a cantilevered support arm. The installation arm could move transversely to the beam, raise or lower the bar box, and provide a point of support about which the bar box could be rotated to match the azimuthal angle of the bar box slot. Figure 30 shows the installation of one of the upper boxes.

Prior to installation, the beam from a He-Ne laser mounted at the back of the installation fix-

ture (the end furthest from the interaction point) was aligned with the rails on the installation fixture using a target that moved along these rails. A mirror was mounted on the face of the AF (see Figure 6) and was used to align the tracks of the installation fixture perpendicular to the face of the AF as follows: a) the bar box was rotated in ϕ, and adjusted in x–y until its forward end was centered with and parallel to the bar box slot into which it was to be inserted, and b) the height and transverse location of the rear of the bar box was adjusted until the beam from the laser mounted at the rear of the installation fixture reflected from the mirror mounted on the AF came straight back to the laser.

At this point the bar box could be slid from the rails of the installation fixture into the bar box slot, the load being taken up by the bar box wheels that ride on tracks of the support structure.

During installation, the z location of the bar box inside the support structure was determined by a temporary stop that fastened to the bar box at the gas inlet. As described above, the pressure of the SOB water on the window corresponds to a force of about 1500 N for each of the lower bar boxes, and this force must be resisted via a connection between the back of the wedge cover and the AF of the support structure. Due to fabrication tolerances the gap between the wedge cover and the AF could vary by several millimeters, so the two surfaces are not perfectly parallel.

To create a solid joint between the AF and the wedge cover, a 6 mm-high (Δr) by roughly 400 mm-wide ($r\Delta\phi$) "putty-like" epoxy [36] was applied to the back of the wedge cover, and then this material was compressed as the bar box was pushed into its slot against the stop just described.

Once the bar box was installed into its slot and the epoxy support allowed to cure (approximately 1 hour), the water seal was made and the gas system connected. About two bar boxes per day were inserted into the detector.

6. Photomultiplier tubes

In the DIRC, the Cherenkov photons are detected by 10,752 PMTs, covering the toroidal surface of the SOB. The PMTs are arranged in a closely packed array and equipped with hexagonal reflective "light-catchers" in order to maximize the detection area (see Section 6.6). The PMTs and light-catchers are submerged in the water, which fills the SOB.

As Cherenkov radiation is a weak source of photons, the PMTs work in single photoelectron detection mode. A high quantum efficiency and sufficient gain are desired to detect photons efficiently in the visible and near-UV range. Furthermore, to reduce backgrounds the PMT should have good timing resolution and a low dark noise rate.

The ETL 9125FLB17 PMT [37] was chosen from several types of PMTs [38,39]. It is a cylindrical PMT with a diameter of 28.2 mm and an active photocathode diameter of about 26 mm. It has eleven stages of amplification with a linear dynode structure. It has a planar bialkali photocathode with a mean sensitivity in the blue, measured using a standard Corning CS5-58 filter, of 11.5 μA/lm-blue. The envelope is made out of a special borosilicate glass that is resistant to the corrosive action of very pure water (Table 5).

6.1. PMT performance

As part of the quality control procedure, a set of mechanical tests were performed on all PMTs including: visual inspection of the photocathode, measurement of the PMT glass envelope length and diameter, and the pin concentricity. About 1 % of the PMTs failed the mechanical tests, these were then exchanged or repaired by the vendor.

The basic operational characteristics of 12 % of the total order of 10,880 PMTs were checked before installation in the DIRC [40]. Five parameters were measured: the working voltage, the peak-to-valley ratio of the single photoelectron spectrum, the timing resolution, the dark noise rate and the usable size of the photocathode. Two light sources are used for the measurements [41]. Both were blue diodes with a wavelength of 450 nm pulsed with a time resolution

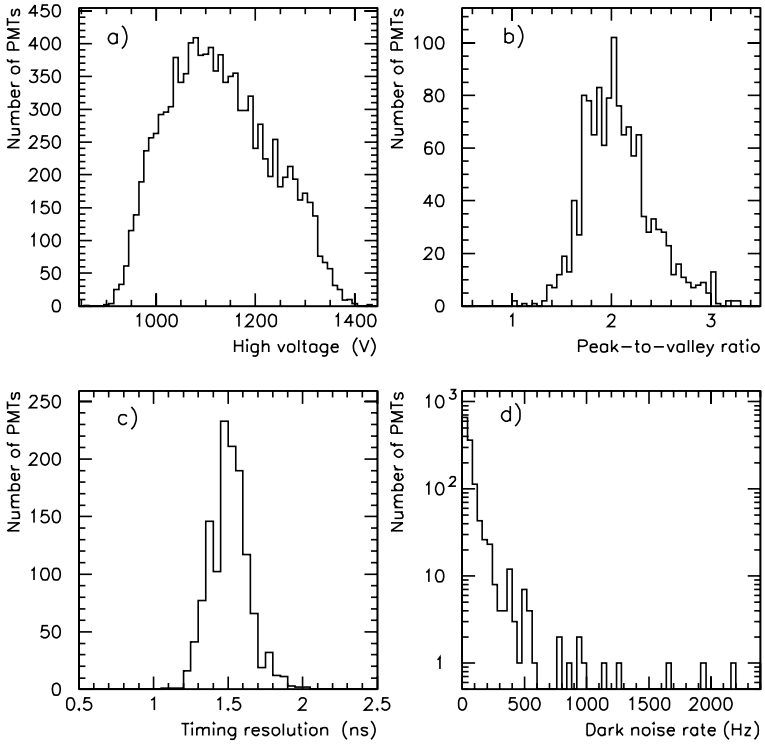

Figure 31. Distributions of the working voltage for all (10880) PMTs (a) and, for the sample of 1283 tested PMTs, the peak-to-valley ratio of the single photoelectron spectrum (b), the timing resolution (FWHM/2.35) (c), and the rate of dark noise (d).

of about 0.7 ns [42]. The intensity of the first was set at 0.3 photoelectron per pulse, in order to work in single photoelectron detection mode. A diffuser ensured illumination of the whole photocathode. The second diode was used only for the scan of the photocathode and had a greater intensity, about 100 photoelectrons per pulse. A collimator with a diameter of 0.5 mm allowed the illumination of a small region of the photocathode.

The working HV, used in all subsequent measurements, was defined as the one which gave a mean amplitude for the single photoelectron signal of 20 mV (measured with a digital oscilloscope). A correction was applied for the small fraction of pulses with two or more photoelectrons and the effect of the threshold, which was set at 3 mV (15 % of the signal). Since the pulse shape was the same for all tested PMTs, the single photoelectron amplitude in each PMT was equivalent to a charge gain of about 1.7×10^7. As shown on Figure 31a, the working HV of all PMTs is in the range from 900 V to 1400 V. It was well below the 1600 V maximum guaranteed by the manufacturer for our operating conditions.

To have good detection efficiency for a single photoelectron, the signal peak should be well separated from the pedestal peak, which results from electronic noise. A useful measure of this is the *peak-to-valley ratio*, which is the ratio of the peak of the single photoelectron charge distribution to the minimum of the distribution situated between this peak and the pedestal peak. The measured distribution of the peak-to-valley ratio is shown in Figure 31b; the average peak-to-valley ratio was 2.07, indicating that good single photon efficiency was achievable.

Good timing resolution is necessary to remove

random backgrounds. The timing distribution in the DIRC PMTs is non-Gaussian, because the transit time depends on the impact point of photons on the planar photocathode [38], and of the photoelectrons on the first dynode. We extract a timing resolution from the full width at half maximum (FWHM) of the distribution recorded in the TDC. Figure 31c shows the distribution of the timing resolution, defined as σ = FWHM/2.35 and corrected for the timing resolution of the light source. The average resolution was 1.5 ns.

The dark noise rate was defined as the number of counts above threshold per second while the PMT has been in the dark with the HV on for several hours. Figure 31d shows this distribution, measured with a threshold of 4 mV. The mean value was 72 Hz. All PMTs have an intrinsic noise rate well below the roughly 100 kHz rate of random photons originating from the sources in or near the accelerator.

A scan of the photocathode allows quality control for the effective size. The PMTs were scanned, with a step of 0.5 mm, along the most favorable direction, parallel to the dynodes, since the useful area was not absolutely circular. With a light intensity of about 100 photoelectrons per pulse, the ADC spectrum was Gaussian. The spectrum mean value, after subtraction of the pedestal, measured the photon detection efficiency. The useful diameter was defined as the length over which the photon detection efficiency exceeded 75 % of its central value, calculated using the points within 5 mm of the center. Furthermore, the rms of the measured efficiencies within the useful diameter provided an estimate of the inhomogeneity of the photocathode. As shown in Figure 32, there was an average useful diameter of 25.8 mm and an inhomogeneity of 4 %.

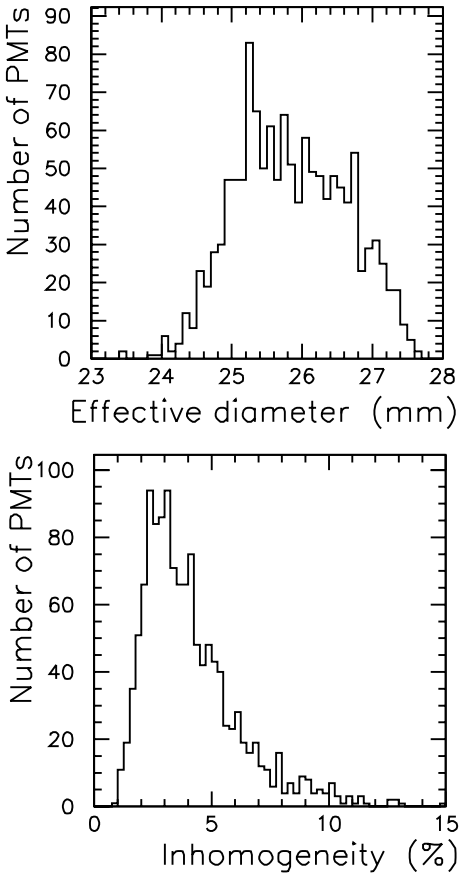

Figure 32. Distributions of the useful diameter (top) and inhomogeneity (bottom) of the photocathode for all tested PMTs.

6.2. Effect of a magnetic field

In order to investigate the effect of an external magnetic field on PMT operation, a field is created around the PMT by two Helmholtz coils with a diameter of 30 cm, which provides a maximum field strength of 20 G [43]. The field is measured by a Hall effect magnetometer with an accuracy of 0.2 G. The PMT is illuminated by a pulsed blue light whose intensity is chosen to work in single photoelectron detection mode, as described in Section 6.1. The measurements are performed using the operating conditions in the DIRC: A single photoelectron signal at ≈20 mV and the electronic threshold at 3 mV.

The relative detection efficiency of the PMT is defined as the number of counts above threshold and in time with the pulsed light, normalized to the value in a null magnetic field. Figure 33a shows the relative detection efficiencies of the PMT in magnetic fields of varying strength with three different orientations with respect to the PMT axis, transverse and across the dynodes (X), transverse and along the dynodes (Y) and longitudinal (Z) (see Figure 34b).

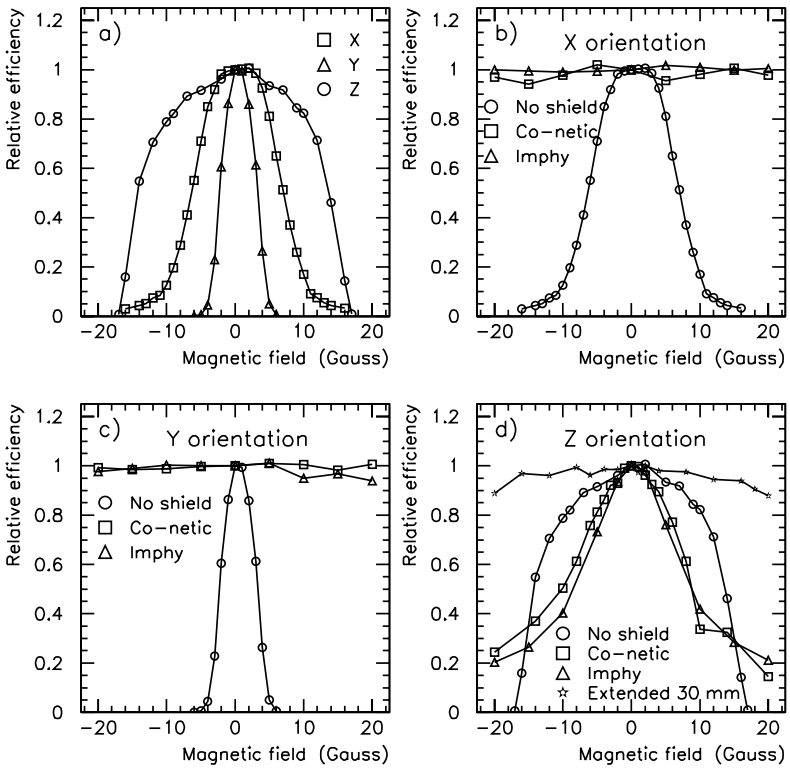

Figure 33. Relative efficiencies of the PMT as a function of the magnetic field: (a) the effect of orientation and of shielding in the three orientations (b) X, (c) Y, and (d) Z. "Co-netic" and "Imphy" are high permeability shields, described further in the text.

Orientation Y is found to be the most sensitive orientation. Furthermore, the performance of the PMT is less degraded in a longitudinal field than in a transverse field. This is in agreement with measurements from the manufacturer. For a random transverse orientation, the detection efficiency lies between those observed for the X and Y orientations. In fact, there is not much difference in the detection efficiencies obtained with a magnetic field oriented along either X or Z if the intensity of the field is smaller than 3 G. However, for the Z direction, the detection efficiency decreases more slowly with increasing magnetic field strength. The relative detection efficiency remains higher than 95 % for magnetic fields up to about 1 G, 3 G and 3.5 G in the Y, X and Z directions, respectively. It is still at 90 % at 7 G for longitudinal fields, while it no longer exceeds this value beyond 4 G in the X direction and 1.5 G in the Y direction.

Each PMT was marked such that during installation in the SOB it could be rotated to orient the most sensitive axis aligned with the field component that had been calculated to be the lowest (see Section 4). To a good approximation the smallest component of the magnetic field is in the azimuthal direction with respect to the *BABAR* axis.

The cause of the PMT efficiency deterioration with magnetic field has two main contributions:

- A decrease in the efficiency of photoelectron collection: The magnetic field causes some of the photoelectrons created at the photocathode to be deviated from the trajectories determined by the inter-electrode electric field so they do not reach the first

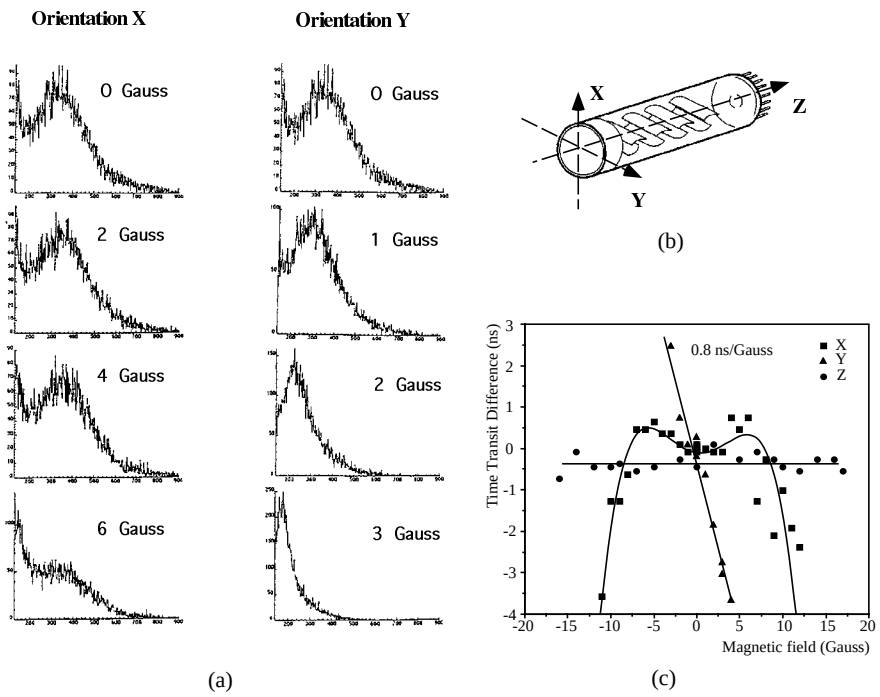

Figure 34. (a) ADC spectra for increasing intensities of the magnetic field, oriented along either the X (left) or Y (right) direction, (b) the geometry of the dynodes, and (c) the effect on the transit time.

dynode.

- Perturbation of the electron multiplication process: The magnetic field also deflects secondary electrons as they traverse from one dynode to the next one. Some fraction of them are lost, causing a drop in the photomultiplier gain.

Figure 34a shows that the loss of efficiency is mainly due to a lower photoelectron collection in the favorable orientation (X) and to a drop of the gain in the unfavorable orientation (Y) [44]. A magnetic field oriented along Y deviates the electrons in the X direction such that some may miss the dynode whose size is designed to match the spread of the multiplication shower in the absence of a magnetic field. The effect of the magnetic field on the transit time in the PMT is represented on Figure 34c.

To minimize the effect of magnetic fields a well-known solution is to place the PMTs inside individual mu-metal shields. Two kinds of mu-metal, Co-netic and Imphy, were investigated; the former is manufactured by Perfection Mica Company (Illinois), the latter by Imphy S.A. (France). Both products appear as a metallic foil that is rolled around the PMT. They do not need rebaking after rolling. Several thicknesses were tried and a 0.1 mm thick foil was found to be sufficient.

Figures 33b, 33c and 33d show the relative efficiencies of the PMT with and without the shield when the magnetic field is increased up to 20 G. The two shielding materials give approximatively the same results. The efficiency of the PMT remains practically unchanged even in a transverse magnetic field of 20 G, for both X and Y orientations. For longitudinal fields a loss of efficiency is observed when introducing the shielding since the lines of magnetic field are disturbed by the presence of the shield and as a result a transverse field is created near the photocathode. The standard solution to this problem is to extend the shielding beyond the front window of the phototube. With

an extension of 30 mm the PMT becomes nearly insensitive to longitudinal magnetic fields up to 16 G. The relative efficiency exceeds 95 % over that range, as shown in Figure 33d for the Imphy material; we see essentially the same result with a Co-netic shield. However this solution is not appropriate for the DIRC since it would lower the collection efficiency of Cherenkov light due to shadowing of adjacent PMTs. It would also prevent the installation of light-catchers in the inactive areas between PMTs, which provide a 20 % increase in photon detection efficiency.

The magnetic shielding solution is described in Section 4: a magnetic shield of soft iron is placed around the entire region of the PMTs, and a bucking coil, whose current is adjustable, reduces the magnetic field at the PMTs to values smaller than 1 G.

6.3. Effect of helium

The DIRC PMTs may spend up to 10 years in an environment that could be exposed to helium from leaks in the accelerator magnet cooling system, or that might be used for checking for vacuum leaks. An investigation was performed to determine the exposure to helium they could sustain before suffering an unacceptable loss in performance.

Helium pressure, P, inside a PMT placed in a constant atmosphere with a partial pressure of helium, P_0, will gradually increase with time up to P_0. The time dependence of P can be parameterized by $\frac{P}{P_0} = \frac{t}{\tau}$, where the time constant τ depends on the composition and thickness of the PMT glass, and on the temperature and total pressure outside the PMT [45]. For the DIRC PMTs, the value of τ is $\simeq 1.9 \times 10^{10}$ s.

This formula is only valid for $P << P_0$, as P approaches P_0, the dependence is no longer linear due to saturation. Helium is present in the air at a partial pressure of 0.53 Pa ($5.2 \times 10^{-6} P_{atm}$, where P_{atm} is the standard atmospheric pressure). Therefore with no extra source of helium, it will take nearly 600 years for the pressure of helium inside the PMT to reach this value. Furthermore, at this level operation of the PMT is not in jeopardy [45].

If this pressure is used as a safe benchmark, it would require an average external helium partial pressure of about 31 Pa ($3.1 \times 10^{-4} P_{atm}$) to reach this value within the expected 10 year lifetime of the experiment. This is about 60 times greater than normal. With this parametrization the same outcome would be expected to occur in about one day (27 hours) in pure helium.

To test this estimate experimentally, the evolution of eight PMTs was studied over a period from 2 weeks to 14 months [46]. Two PMTs were measured in a mixture of helium and air for 15 days. Another was exposed to pure helium for 32 days. Four PMTs remained in pure helium for 1 day, 3 days, 5 days and 12 days respectively then were left in the air and their performance monitored for 7 months. One PMT was kept away from helium as a reference and was measured over a period of 14 months.

It was not possible to use the same experimental setup for all the PMTs. The first two PMTs, with their bases, were put entirely in the gas container filled with a mixture consisting of 90 % of helium and 10 % of air. However, the PMT base experiences arcing in pure helium at the operating voltage; so to measure the third PMT in pure helium, a structure was built to allow the base to remain outside of the helium container. Four PMTs were left, unpowered, in a small container filled with pure helium. Measurements of the PMTs performance were taken before and after exposure to helium.

As a measure of the effect of the helium exposure, we looked at the position of the pedestal-corrected peak corresponding to a single photoelectron in the charge distribution. This quantity is directly related to the gain of the PMT. The evolution of dark noise of the PMT was also measured, but no significant effect was observed with a threshold at 3 mV. As expected, the gain of the reference PMT was quite constant, as were the two PMTs kept in the helium-air mixture for 15 days.

Figure 35 shows the evolution of the position of the ADC peak, measured in arbitrary units, for the six PMTs observed over an extended period. The gain of the PMT kept in pure helium for 32 days remained stable for nearly 20 days, then decreased quite rapidly. This indicates that

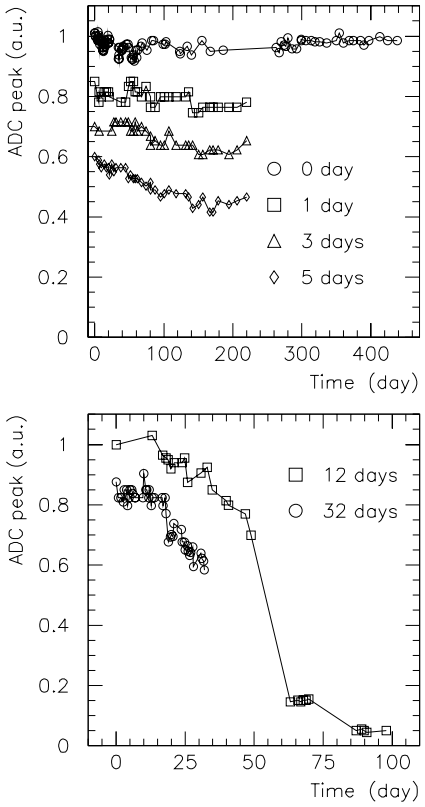

Figure 35. Evolution of the PMT gain with time during and after helium exposure. The ADC peak for each data series is normalized to the value at the beginning of the period; for illustration purposes the scale is adjusted by an arbitrary amount for each series.

it takes approximately this time for helium to migrate through the glass in sufficient quantity to affect the PMT performance. This explains the stability of the two PMTs studied for only the first 15 days of exposure.

This behavior was also observed with the PMT that stayed for 12 days in pure helium. The gain did not appear much affected immediately after these 12 days but began to decrease significantly after about 25 days. It appears that the helium that has entered the glass continues to move inside after the PMT is in the air since it is repelled from the outside by the atmospheric pressure and not from the vacuum inside. After 50 days, the PMT gain becomes very low, less than 20 % of its initial value.

After 7 months, only an insignificantly small additional gain decrease was seen for the PMT that remained in pure helium for 1 day. There was a 10 % drop in the gain for those that stayed for 3 days, and 25 % for the 5 day sample. In each case the gain seems to reach a stable value, probably at the point when all the helium in the glass has entered the PMT.

In summary, the borosilicate glass, recommended to us by ETL because of the pure water corrosion resistance, seems to be quite resistant to helium diffusion as well. In practice, the worst danger probably would come from a helium leakage while the detector is open. In this case, big fans could be used to blow the helium away from the PMTs well within the danger period indicated by these results. Helium monitoring and active purging of the SOB have been added to provide an additional safety margin during normal operations.

6.4. Glass corrosion

It is well-known that ultra-pure water may corrode silicate glasses, though the extent to which this occurs is strongly dependent on the detailed composition of the material. Table 5 summarizes the composition of glasses used in PMTs from several manufacturers that were subjected to a series of tests (identified by an index number) performed to investigate the effect of ultrapure water on that material. Several of the tests were performed at elevated water temperatures to accelerate the aging process. An aging acceleration factor of 2–2.5 for every 10 °C observed was observed, consistent with that used in industry. The column entitled "notes" in Table 5 provides a qualitative summary of the outcome of the corrosion tests described in more detail in reference [47].

The DIRC detector has about 50 PMTs that have a "frosty" appearance, out of 10,752 in the system. An example of such a tube can be seen for the topmost PMT in Figure 36. Measurement of samples of these PMTs suggest that the glass is being corroded to such an extent that there may be a danger of implosion or vacuum loss over a

Table 5
PMT glass composition (% by weight) in various experiments or tests by the PMT manufacturers.

Index	Company	Experiment	Glass name	PMT part	Notes
1	Hamamatsu	Super-K	Pyrex	face	A,B
2	Hamamatsu	Internal Test			A,B
3	Hamamatsu	Internal Test			C
4	Hamamatsu	Internal Test			C
5	Philips Photonics	Special PMT	ZK(N)7	face	D
6	Electron Tubes Ltd.	*BABAR* DIRC	Borosilicate (B53)	face	B,E
7	Electron Tubes Ltd.	*BABAR* DIRC	Borosilicate	side body	A
8	Electron Tubes Ltd.	*BABAR* DIRC	Borosilicate	pin region	A
9	Electron Tubes Ltd.	Internal PMT	X glass	window	D

Index	$Si0_2$	Al_20_3	B_20_3	Li_20	Na_20	K_20	Ba0	Ca0	As_20_3	Sb_20_3	Zn0
1	80	2.1	14.1	0.1	3.7	0.12	-	-	-	-	-
2	-	-	-	-	5.5	-	-	-	-	-	-
3	67.5	3	19	0	0.4	9	-	-	-	-	-
4	65	0	14	0	0.1	0.06	-	-	-	-	-
5	60.8	5.6	14	-	7.4	0.003	-	-	0.1	0	11.2
6	65	6	15	-	6	-	3	1	-	-	4
7	71	7	11	-	6	1	2	1	-	-	-
8	73	5	13	-	8	0.1	-	-	-	-	1
9	69.6	4.2	17.2	-	8.7	-	0	0	-	-	0

Notes
A: No corrosion observed
B: No transmission loss
C: Significant loss of transmission
D: Significant corrosion
E: Slight corrosion

10-year period.

After reporting these observations to the PMT manufacturer, they discovered that during production the wrong type of glass had been inadvertently included for the windows in one batch; *i.e.,* this so-called X-glass was used instead of the specified B53 glass. A notable difference between the two is that X-glass does not contain zinc, a fact which, according to ETL, makes it more susceptible to rapid leaching of sodium and boron, resulting in the observed "frosty" appearance. Our own extensive tests [47] support this hypothesis.

Even in the PMTs containing B53 glass there is evidence of a low-level of corrosion that might penetrate as much as $30\,\mu$m to $50\,\mu$m depth in 10 years of operation. Nevertheless, the amount of mechanical weakening of the glass is not expected to pose a significant danger of implosion. Prompted by the Super Kamiokande disaster [48], tests were performed to verify that the corroded PMTs in the DIRC would not break due to the pressure shock wave from the rupture of the front window of a neighboring tube.

Some of the B53 tubes display evidence of a more diffuse surface corrosion and were designated as "milky". An example can be seen in the lower right PMT of Figure 36. It is probable that this form of corrosion has a small effect on photon transmission from the water to the photocathode because of good optical matching between the water and glass (see Section 11.2).

The classification of the PMT glass corrosion

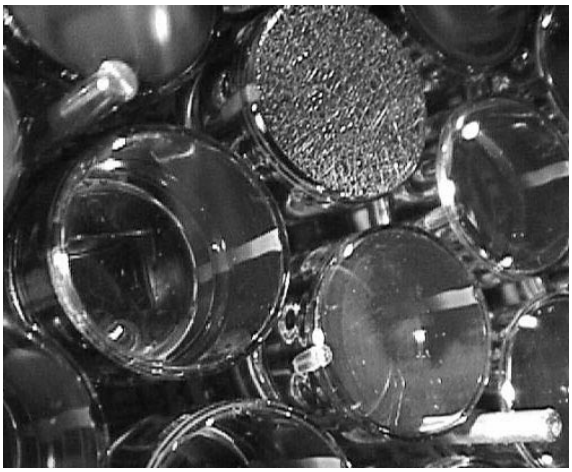

Figure 36. Example of an undamaged PMT (left), a "frosty" PMT (top), and a "milky" PMT (bottom), observed in the drained SOB roughly one year after it was first filled with ultra-pure water.

in the DIRC was based on visual observations, X-ray ESCA (Electron Spectroscopy for Chemical Analysis) surface analysis, careful weighing, and light transmission measurement. In addition, analysis of trace elements in the water allowed us to make a quantitative prediction of the sodium removal rate (see Section 7.2 and Table 7).

Although it is clearly a significant factor in our case, the explanation that glass corrosion depends upon zinc content may not be the complete answer. Most likely a more detailed understanding of the chemistry of each particular glass is required. For example, Table 5 shows that in the Pyrex type of glass, such as used in Super Kamiokande, there is no zinc, yet there is no apparent corrosion of the PMT glass window [49] even though DIRC and Super Kamiokande have a comparable water purity. Apparently, zinc is necessary only in *some* borosilicate glass formulations.

Further evidence that the absence of zinc is not a reliable indicator of corrosion susceptibility is the lack of sodium leaching or corrosion on the sides of the glass body of the DIRC milky-faced PMTs. These sides are not made of B53 but another form of borosilicate glass containing no significant amount of zinc. However, the side glass is produced as a tube and goes through a completely different production process.

A dramatic counterexample for the effect of zinc is the experience of Philips Photonics with the ZK(N)7 glass. This glass contains a very large amount of zinc (see Table 5) and suffers from an extremely large rate of corrosion in just humid air [50]. Therefore, it appears that glass corrosion is dependent on a delicate balance of various glass ingredients, in which zinc may play a significant protection role only if present in the correct proportion.

Based on our empirical observations the front window glass of the DIRC PMTs requires a few percent of zinc in order to limit the corrosion rate. However, the apparent complexity of corrosion susceptibility suggests that an exhaustive set of corrosion tests should be performed for any particular choice of glass formulation.

6.5. PMT base and HV system

A low-cost, compact, high reliability PMT base and HV distribution system was developed to power the DIRC PMTs (Figure 37). The use of injection molding significantly reduced the cost of the project without compromising quality.

To meet specifications for single photon detection efficiency, the PMT/base system was designed to operate at a charge gain of $(1-2)\times10^7$. During the design stage it was expected that the normal operating single-tube maximum rate would be of the order 100 kHz, resulting in a maximum anode current of approximately 300 nA per PMT. The base was designed and tested to accommodate operation at several MHz without significant performance degradation. Measurements of gain [51] in a large number of PMT samples indicated that it was necessary to allow for an operational voltage range from 800 V to 1400 V to meet these requirements. To provide a safety margin and allow potential operating voltage increases due to tube aging effects, the base was designed to allow operation up to 1600 V. The base noise pickup level was specified to be below 2 mV, and the signal was required to return to baseline within 40 ns of a signal start [52].

A traditional resistor divider chain design was

selected for the base; a schematic of the base is shown in Figure 38. A Cockcroft-Walton type voltage multiplier was investigated but rejected due to the cost of the more involved circuit development, and a higher component count, which would have resulted in difficulties fitting within the available space and reduced long-term base reliability.

Figure 37. Photograph of a group of DIRC PMT bases with signal and HV cables attached.

6.5.1. Electrical requirements

For resistor-divider type bases, it is recommended to design a divider chain that can withstand an current draw of at least 100 times the maximum expected anode current; this protects against rate-related changes in the accelerating voltages across the dynodes. In our case, this criterion indicates a lower bound of 30 μA. Maintaining a low current draw in the chain has several beneficial effects: Less power required from the power supplies; less thermal power dissipation in the base; and improved component reliability. A resistor divider chain with a total resistance of 10.8 MΩ was chosen. This gives a current draw of 74 μA at 800 V and 148 μA at 1600 V, allowing a comfortable safety margin for unexpected operation outside of the normal mode.

To reduce costs for the supplies and HV cable system, groups of 16 tubes of similar gain were operated at a common voltage provided by a single distribution board.

The HV is provided by a programmable CAEN SY-527 HV distribution system [53]. Each of the 12 sectors receives HV through 56 channels distributed in a single cable bundle. A total of 672 HV channels are needed for the entire DIRC system. Each voltage can be set between 0 kV and 1.6 kV.

In order to maximize single photon detection efficiency, the voltage between the photocathode and the first dynode should be close to the maximum allowed for the tube. The resistor divider was designed to provide 3.6 times the potential between the cathode and the first dynode as that between the other eleven dynode stages. Zener diode stabilization of this voltage was considered but rejected due to reliability concerns, and an insufficient current flow to ensure the diode would function properly.

Each base has a grounding connection to the SOB, which acts as the common ground for the system. This ground is connected directly to the signal cable ground, and through a 1.5 kΩ resistor to the HV ground return. The ground connection to the SOB is interruptible as a precaution since the electrical noise environment of the DIRC after installation in *BABAR* was unclear.

6.5.2. Mechanical requirements

The photomultiplier tubes are positioned in a close-packed array at the back of the SOB, and the PMT faces are directly in contact with the water inside the SOB. The photomultiplier tubes are housed in custom-molded plastic housings, which penetrate the SOB rear bulkhead (see Figure 14). These housings contain the wire leads that were soldered to the standard PMT pins by the manufacturer. The leads are on an 18 mm diameter circle, and the bases were required to connect to these wires. The placement of these tube housings limit the space available for the base to a 31 mm diameter circle. To preserve maximum flexibility for replacing tubes and to allow for independent orientation of the PMTs,

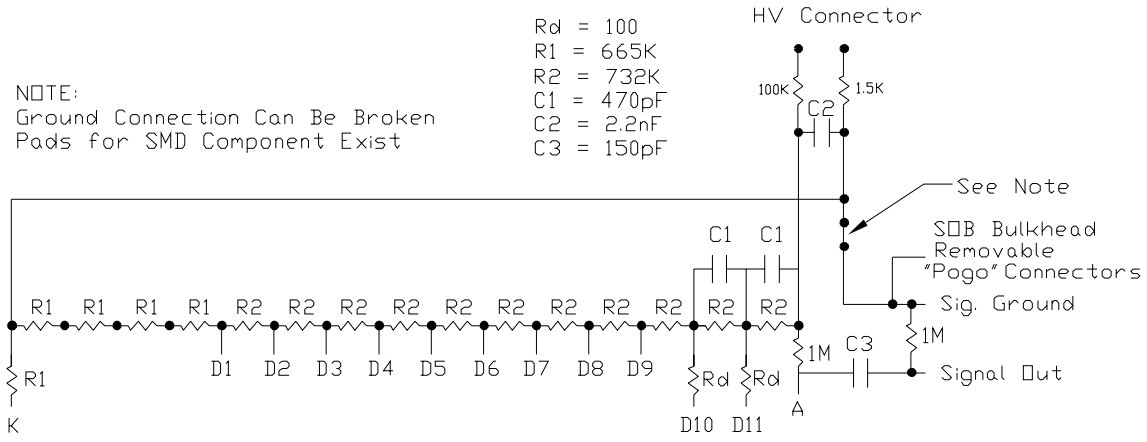

Figure 38. Schematic diagram of the DIRC PMT base. All resistance values are in ohms.

it was decided to build the bases as individual units, rather than supply multiple tubes from a monolithic unit.

6.5.3. Electronic design implementation

The bases were designed to fit on a double-sided 29 mm diameter circular printed circuit board. The criteria for separation of traces carrying HV and other components on the board were determined using the standards published by the Institute for Interconnecting and Packaging Electronic Circuits (IPC-D-275). A permanent polymer conformal coating for all exposed conductors was also required by these standards. The spacing requirements on the PCB led to component placement position tolerances of 0.25 mm and small solder pad sizes.

Surface mount components were used to minimize space requirements and to allow for automated assembly of the boards. All components were standard, commercially available items except for the HV decoupling and filter capacitors, which were custom manufactured for the project [54]. The component values, particularly the HV decoupling capacitor, were chosen to prevent a failure resulting in a dead short damaging the front end electronics.

6.5.4. Electrical reliability calculations

Reliability was an important consideration in the design of the bases since they must operate in a closed region, which is inaccessible for repair or replacement for long periods. Concerns about reliability are enhanced by the possibility that certain failure modes for a single base will disable all 16 bases powered by the same HV channel. In this design, the power dissipated by each resistor in the voltage divider chain is quite low (< 0.02 W), and the maximum ambient operating temperature of the base is 40 °C. Under these conditions, satisfactory reliability estimates were obtained for the bases by using resistors meeting the specification MIL-R-55342D for the HV resistor chain. The HV decoupling and filter capacitors operate closer to their performance limits, and a military reliability rating of *S* (space rated) was specified. All capacitors were tested by the manufacturer to 1.5 times maximum rated voltage at maximum operating temperature for 72 hours.

During the design process an evaluation of the expected reliability of the components and circuit design was conducted following the guidelines given in the military specifications handbook (MIL-HDBK-217F). The results for the main components are given in Table 6. The calculations assume an ambient temperature of less than 40 °C inside the SOB, and an environmental classification of *standard workplace environment*. The combination of the individual component rates leads to an expected annual failure rate of 12.1 bases per year (8760 hours). Since some failure modes result in the loss of all 16 tubes connected to the same HV power supply, the an-

ticipated total number of PMT channels lost due to base failures is 15.2 per year; in practice the failure rate attributable to bases failures has been at least a factor of ten lower during several years of operation.

6.5.5. Mechanical design implementation

The PMT bases used a custom-designed injection molded housing [55] and HV connector, which significantly reduced costs. The PMT housing was molded from Celenex 3312-2P [56], a PBT (Polybutylene terephthalate) plastic with bromine-based fire retardant and 30 % silica glass fiber fill for dimensional stability. This material is widely used by industry in electrical connectors and housings. The connection between the PMT and the base PCB was made by 13 individual pin sockets [57]. A ground connection is made to the SOB bulkhead via a "pogo" connector, a removable spring-loaded pin [58]. The base housing is covered with a molded lid, through which protrude the HV and signal connectors [59] and a post for an alternative external ground connection. The temperature inside a covered base housing with a base operating at 2000 V was measured to be less than 40 °C.

The HV connectors were molded out of the same material as the housings (Celenex 3312-2P), and used the same Mill-Max pin sockets along with a Mill-Max solder pin [60]. The pins were glued into the male connector bodies using an epoxy [61]. The connectors were tested for leakage current and micro-discharging, and found to have less than 0.1 nA leakage current at 4000 V, and a micro-discharge rate of < 0.1 Hz at a 2 mV threshold.

6.5.6. Assembly and testing

Panels of 42 PMT base printed circuit boards were produced, and the surface mount components placed and soldered by Circle Circuits Inc. [62].

Following an initial visual inspection for component placement and a measurement of electrical conductivity of vias, HV and signal connectors were soldered to the PCB and the bottom side of the bases painted with conformal coating [63]. The PCBs were then soldered into the base housings, and the top side of the PCB was also painted with the conformal coating. The serial number was written on the side of the housing in indelible ink. Housing covers were then attached to the housing using cyanoacrylate adhesive. Quality control and tracking records were kept for each batch of 42 bases during assembly.

Following assembly, the bases passed through a battery of quality assurance tests. The initial test consisted of a 12-hour burn-in at 1800 V, which is 200 V above the expected maximum operating voltage. For this test, the bases were connected together in parallel using the production HV distribution harnesses, providing a simultaneous test of both systems. Following this, the bases were run through a computer controlled [64] battery of tests to check the values of the voltage divider chain resistors, the current draw of the base, and the values of the HV decoupling and filter capacitors. Finally, the base was connected to a reference PMT and a single photoelectron spectrum was collected, providing a check on both the gain and noise performance of the base. QA records were maintained for each base.

Finally, the pogo pin ground connector was installed into the base and the electrical contact to the base was checked with an ohmmeter. The bases were then sealed into individual bags and packaged in expanded polystyrene panels for shipping to SLAC.

6.5.7. HV distribution

HV for the bases is supplied from modules, located approximately 30 m from the SOB, on shielded 60-cable bundles (56 active plus 4 spares). The cables penetrate the DIRC magnetic shielding via feedthroughs that terminate the outermost RF shield braid. Once inside the SOB, the individual cables connect to HV distribution patch panels, one per sector, mounted on the SOB with the front end electronics racks. From there, a local cable harness, 1.3 m-long, distributes the HV from one supply cable to 16 individual bases through a daisy-chain of custom HV connectors, visible in Figure 37. The signal cables from these 16 tubes are bundled together with this harness.

The HV distribution patch panel PCBs were

Table 6
PMT base failure rate calculation.

Component	Mil. Spec Rating	Number of failures per year (10,752 bases)	Number of Bases affected per failure	Total Channels lost per year (10,752 bases)
HV Decoupling Capacitor	S	0.07	16	1.1
HV Filter Capacitor	S	0.13	16	2.1
Dynode Reservoir Capacitor	Commercial	5.28	1	5.3
SMD Resistors	M	3.46	1	3.5
Printed Circuit Boards	Commercial	2.2	1	2.2
HV Connectors	Commercial	0.96	1	1
Totals:		12.1		15.2

produced at Circle Circuits Inc. Each PCB was visually inspected, and the SHV bulkhead and custom female connectors soldered to the board. All exposed HV conductors were then coated with conformal coating [63], and the distribution board mounted into a sheet metal enclosure. A 3.2 mm Delrin template sheet was placed between the PCB and the sheet metal box for additional support for the connectors and to provide electrical insulation. The HV ground return was connected to the SOB ground via a removable 100 Ω resistor. Following assembly, each channel was tested at 3000 V and required to have less than 1 nA leakage current. Records were kept for all HV testing.

Each HV distribution harness consists of 17 male custom HV connectors in parallel. Sixteen of the connectors are joined by 15 cm lengths of hookup wire, while the 17th connector, which attaches to the HV patch panel, is connected by a 130 cm length of twisted pair hookup wire. The ground return wire is 22 AWG FEP Teflon wire [65], and the HV leg is 22 AWG HV rated FEP Teflon wire [66].

During harness assembly, short lengths of the hookup wire were soldered to male Mill-Max pins, which were glued into male HV connector bodies with epoxy. The cable assemblies were then tested for continuity and operated in the HV burn-in portion of the base testing to check for short circuits or excessive current draw. Each of the harnesses was then numbered and color-coded to assist installation in the DIRC.

6.6. Light-catchers

The effective active surface area of the PMTs is increased to 90 % of the detection surface by the addition of hexagonal "light-catchers" [67]. These reflectors, which surround the PMT windows, have a 20° half angle slope, are 8 mm high, and have a 25 mm diameter opening corresponding to the size of the PMT photocathode (Figure 39).

Figure 39. PMTs and rhodium-plated light-catchers in the SOB.

The light-catchers are made of thermoplastic ULTEM 1010 [68] metallized with rhodium on a TiW layer in a process developed by Innovations Couches Minces (ICMC) [69]. A light-catcher test sample was subjected to an aging process

by submersion in hot deionized water (70 °C) for 45 days, corresponding to roughly 5 years at the nominal SOB water temperature. No degradation was observed in the measured reflectivity of about 80 %.

The improvement in the number of photons collected in the the DIRC due to the light-catchers was measured to be 20 ± 0.1 % using LED light at 450 nm.

7. Utility systems

7.1. Gas system

To ensure that the bars are maintained in a low moisture environment, dry nitrogen gas from liquid nitrogen boil-off flows through each box at the rate of 9 L/h and is monitored for humidity. The gas is filtered through a molecular sieve and three mechanical filters to remove particulates (7 μm, 0.5 μm and 0.01 μm). Typical dew points on the gas exhausted from the bar boxes are on the order of –60 °C, although one bar box has a consistently higher dew-point around –30 °C with an enhanced N_2 flow rate. About one third of the input N_2 gas leaks from the bar boxes and keeps the bar box slots in the mechanical support structure free of condensation.

Potential leaks from the water seals between the bar boxes and the SOB are detected by an extensive water leak detection system. There are 20 custom water sensors in and around the bar box slots and two commercial ultrasonic flow sensors are used to monitor water flow in two (normally dry) drain lines. In addition, there are humidity sensors on each of the twelve N_2 gas output lines.

The custom water sensors consist of a pattern of interdigitated copper lines printed on Kapton [70] foil, shorted by a 3 MΩ resistor at the end of 15 m of cable. The nominal loop current of 1 μA is monitored, higher currents indicate the presence of water and lower currents are indicative of a fault condition.

Each bar box is monitored by four different water sensors (some water sensors are shared between bar boxes for mechanical reasons). A majority-logic system based on the input from the 34 water and humidity sensors determines if the water in the SOB should be released. A water dump is initiated if 2 out of 4 sensors corresponding to the same bar box indicate the presence of water. The system is connected to the *BABAR* Uninterruptible Power Supply (UPS); in the event that this fails, no dump occurs.

7.2. Water system

The DIRC water system is designed to maintain good transparency at wavelengths as short as 300 nm. One way to achieve this is to use ultra-pure, de-ionized water, close to the theoretical limit of 18 MΩ·cm resistivity. In addition, the water must be degassed and the entire system kept free of bacteria. Purified water is aggressive in attacking many materials, and those in the contact with the water were selected based on known compatibility with purified water. To maintain the necessary level of water quality, most plumbing components are made of stainless steel or polyvinylidene fluoride (Kynar [71]).

Figure 40 shows the DIRC water system. The input line contains five mechanical filters (three 10 μm, one 5 μm, and one 1 μm), a charcoal filter, and a reverse osmosis unit with a 5 μm prefilter. This line supplies a water holding tank, parallel pumps and de-ionization beds with 1 μm exit filters. A single UV lamp (254 nm wavelength) irradiates the water to prevent growth of bacteria. The irradiated water then goes to parallel 0.2 μm filters whose outputs merge into a single Teflon microtube degasser to prevent bubble formation on the face of photomultipliers. This parallelism permits the serviceable items to be replaced without interrupting flow to the SOB. Sampling ports are provided to check the water quality and to monitor resistivity, pH-value, temperature, and flow. A gravity feed return system prevents overpressure. The entire SOB water volume recirculates roughly 2.5 times a day.

The operating experience with the water system so far has been very good. The resistivity of the water is typically 18 MΩ·cm in the supply line and 8 MΩ·cm to 10 MΩ·cm in the return line at a temperature of about 23 °C to 26 °C. The pH-value of the supply water was typically close to 6.5. The difference between pH-value of the supply and return water is less than 1.0. Figure 41 shows a time history of the DIRC water return

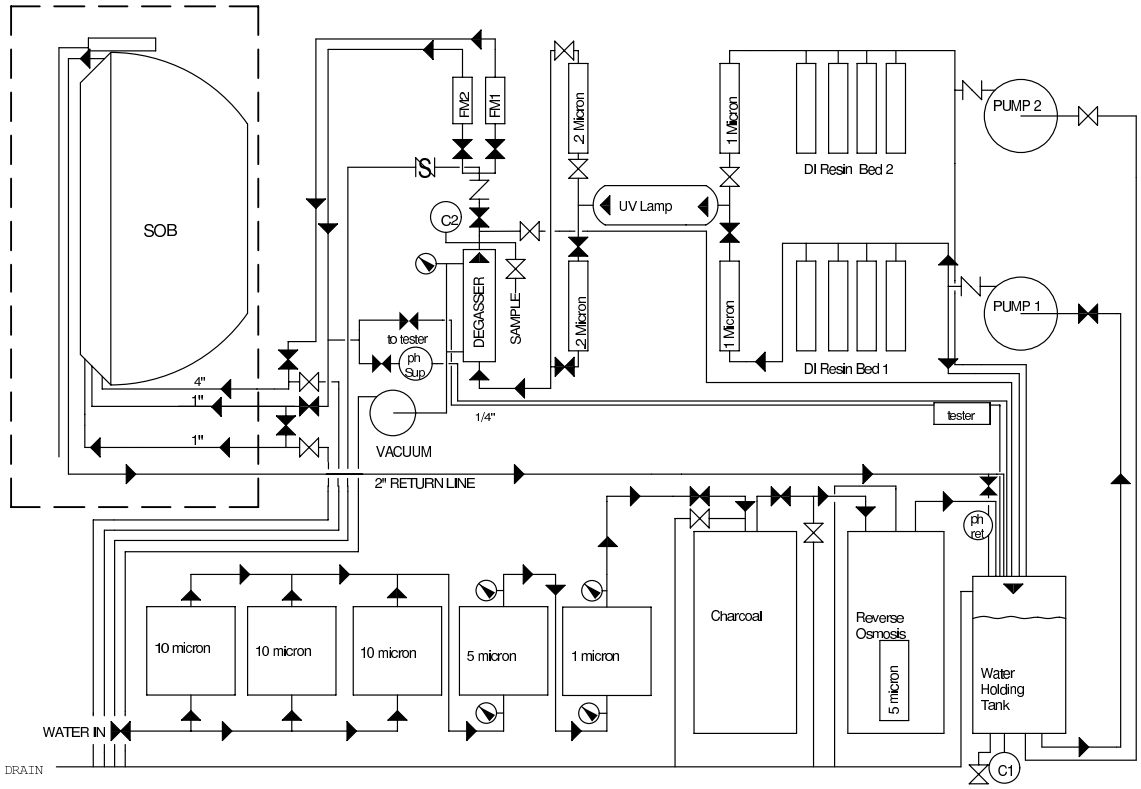

Figure 40. DIRC water purification system.

resistivity and the pH-factor difference between return and supply water. Occasional dips in the return water resistivity are due to the reverse osmosis unit switching on. Normally, it is sufficient to monitor the water resistivity and pH factor as signatures of good long-term water quality.

The water transparency is routinely measured using lasers of three different wavelengths. An aperture-restricted laser photodiode with a diffuser was used to limit multiple light reflections between various surfaces in the setup, which could adversely affect the result through interference effects. Furthermore, the water cell used for this measurement is 1 m long, which is close to the actual photon path length in the SOB. In this way no extrapolation is necessary, which reduces the systematic errors. Figure 42 shows an example of such measurements at 266 nm, 325 nm, and 442 nm. The transmission is better than 92 % per meter at 266 nm and exceeds 98 % per meter at 325 nm and 442 nm.

Bacteria levels and water elemental analysis (using the Inductively Coupled Plasma-Mass Spectrometry, ICP-MS, method) is performed periodically by Balazs Analytical Services Company [72]. Table 7 shows typical levels of major elements among 67 tested. Sodium, which is easy to detect, is a major component of PMT glass and so is used to monitor the leaching rate from the front glass by comparing the sodium level in the water return and supply. The typical difference is (0.2–0.3) ppb. Assuming that the leaching occurs mainly from the front glass surface, this corresponds to a rate of material removal from front glass of about (2–4) μm/PMT/year. Such a rate is unlikely to lead to a PMT glass implosion during the lifetime of the experiment.

Leaks from the water seals between the bar boxes and the SOB are detected by the system described in Section 7.1, and by the water height

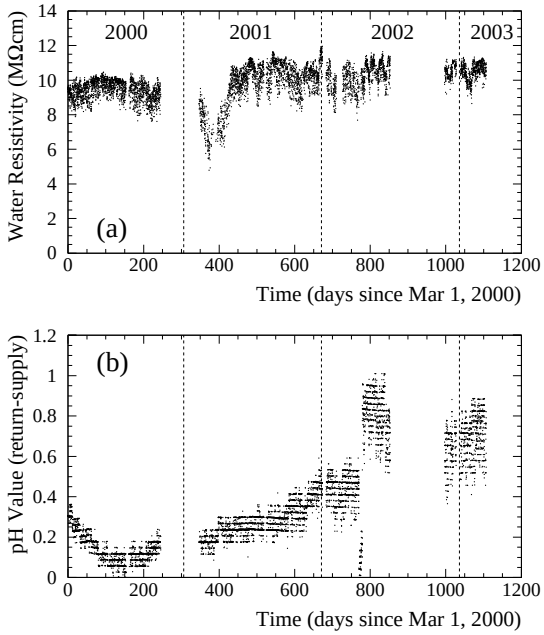

Figure 41. Time history of the DIRC return water resistivity (a) and pH factor difference between the return and supply water (b). The dashed vertical lines indicate the start of a calendar year.

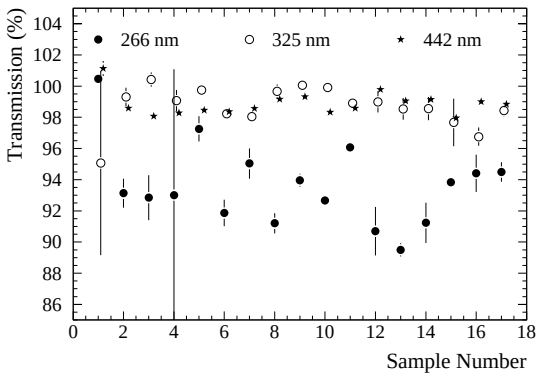

Figure 42. Transmission of the DIRC return water measured at three laser wavelengths over the period of one year.

Table 7
Water analysis of DIRC water as measured by Balazs Analytical Services.

Element	Supply water [ppb]	Return water [ppb]
Boron (B)	2.9	3.2
Silicon (Si)	2.8	3.1
Sodium (Na)	0.014	0.29
Rhodium (Rh)	< 0.001*	< 0.001*
Nickel (Ni)	< 0.004*	< 0.004*

* below the measurement limit

in the SOB, which is monitored by measuring the hydrostatic pressure. Should a water leak be detected, a valve in a 100 mm diameter drain line is opened, and the entire water content of the SOB is drained in about 12 minutes.

All elements inside the SOB (PMT, plastic PMT housing, gaskets, light-catchers) were tested at normal and elevated temperatures for their ability to withstand the highly corrosive action of ultra-pure water and to not cause pollution.

7.3. Environmental monitoring system

The DIRC environmental monitoring system is divided into three parts, corresponding to three separate tasks. The first deals with the control and monitoring of the HV system for the PMTs. The second is devoted to monitoring low voltages related to the Front-End Electronics (FEE), described in Section 8. The third controls a variety of other detector parameter settings.

An interlock system is based on the VME Summary Interlock and Alarm Module (SIAM). This is a standard unit throughout the *BABAR* monitoring system. Three dedicated VME CPUs run the application code for the DIRC.

Communication between the HV mainframes and the monitoring crate is achieved by a CAENET controller (V288). The HV monitor task sets the CAEN units ramping step size parameters and current limits, and provides communication of alarm conditions and the current draw values of each channel.

The purpose of FEE monitoring is to control and monitor parameters related to the FEE.

For each DIRC sector, a custom multi-purpose board, the DIRC Crate Controller (DCC), equipped with a micro-controller [73] incorporating the appropriate communication protocol (CANbus), is situated in the same crate as the DIRC Front-end Boards (DFB). All monitoring and control tasks are implemented on this card. The primary parameters monitored are the low voltages for the DFBs and DCCs, the status of the optical link, the temperature of supply boards, and the VME crate status. An ensemble of 12 beam monitoring scalers is read out by a scaler readout board.

The third part of the monitoring system is based on a custom ADC VME board, VME Smart Analogue Monitor (VSAM), used to monitor various types of sensors: magnetic field sensors, 16 CsI radiation monitors, and the level, pH-value, resistivity, and temperature of the water in the SOB.

8. Electronics

The DIRC FEE [74] are designed to measure the arrival time of each Cherenkov photon detected by the PMT array, to an accuracy limited only by the intrinsic 1.5 ns transit time spread of the PMTs. In addition, the pulse height spectra can be measured to ensure that the PMTs operate at full efficiency. However, because the ADC information is not needed to reconstruct events, 64 PMTs are multiplexed onto a single ADC, which is used only for the slower monitoring and calibration tasks. The design contains a pipeline to deal with the L1 trigger latency of 12 μs, and can handle random background rates of up to 2.5 MHz/PMT with less than 1 % dead time.

8.1. System overview

The DIRC FEE are mounted on the outside of the SOB; the FEE are highly integrated in order to minimize cable lengths and to retain the required single photoelectron sensitivity. The FEE consist of a 64-channel DIRC Front-end Board (DFB), fourteen per sector, and a DIRC Crate Controller (DCC) that serializes the data onto a 1.2 Gb/s optical link. On the other end of the link, a Power PC-604 custom board, called the Readout Module (ROM), processes the data for data-block building, detector calibration, error detection and configuration.

8.2. DIRC **Front-end Board**

Each of the 168 DFB processes 64 PMT inputs. A block diagram of the board is shown in Figure 43. It houses eight analog chips which provide the discrimination of the PMT pulses and their associated logic voltage level translators, four TDC chips which code the PM pulse arrival time on 16 bits with a precision of 500 ps, one 8-bit flash ADC to measure the pulse height, two digitally controlled calibration generators feeding respectively odd and even channels, multi-event buffers, and test hardware. It is connected to a custom crate backplane, the Protocol Distribution Board (PDB), through one VME-like 96-pin connector. The backplane distributes the system clocks, the serial data input and output lines and the power supplies. The gain of each ADC channel is set on-board with 5 % precision. The 64 shaped outputs of the analog chips are multiplexed onto a single flash ADC, which is used mainly for calibration purpose.

A double common-ground plane is used as a voltage reference for all input signals, as well as for digital signals. Such a ground scheme, combined with a copper shield housing the analog chip and input circuitry, and a tight connection between the detector's and electronics' grounds, allows operation with thresholds as small as 1 mV. From the DAQ side, the DFB receives runtime commands on a serial 60 MHz link such as trigger L1, readout calibration strobes, clear multi-event buffers, and synchronization. It also accepts subsystem commands used for initialization such as calibration control, threshold register loading or hardware tests. The board's digital logic is implemented on E2PROM FPGAs[2], which allows its designers to modify it as requirements change.

[2]Electrically Erasable Programmable Read-Only Memory Field Programmable Gate Arrays

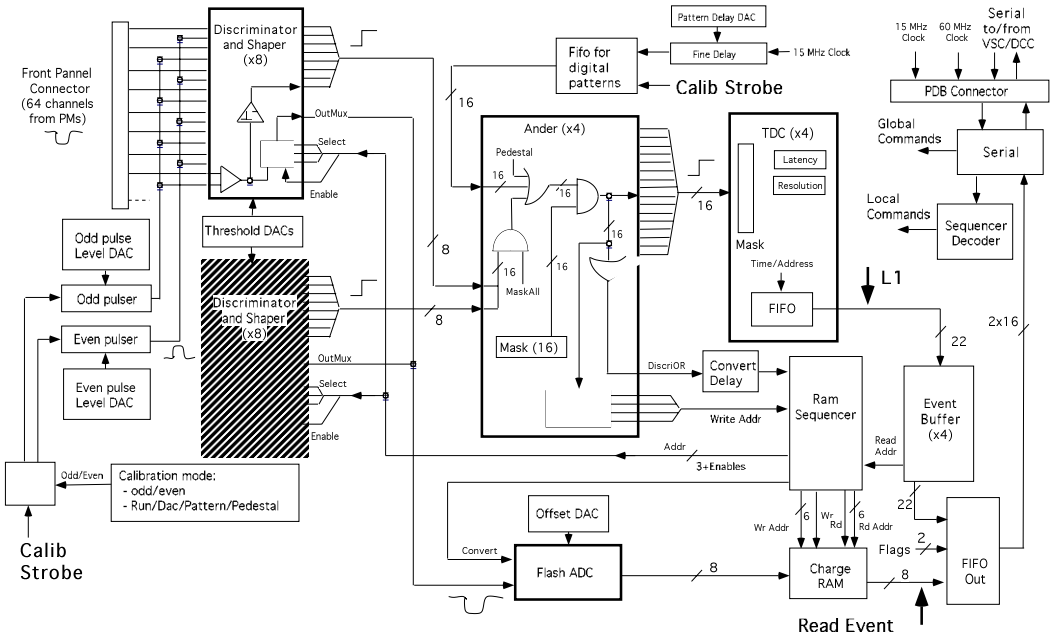

Figure 43. Schematic diagram of the DIRC Front-end Board.

8.2.1. Analog chip

A custom 8-channel analog chip [75] amplifies and shapes the PMT pulses, and allows a voltage threshold to be applied. Each channel produces an approximately Gaussian pulse, shaped to a 80 ns peaking time, which is required for analog multiplexing to the ADC. A zero-crossing discriminator produces a digital pulse timed to the peak of the input pulse. The maximum operating rate is about 50 MHz on average. The digital pulses are output with a low voltage amplitude, to avoid any crosstalk with the very low noise chip inputs, and then translated to usual digital levels with dedicated Gunning Transceiver Logic (GTL) circuits.

8.2.2. TDC chip

A description of the initial version of the DIRC time-to-digital-converter (TDC1) has been published in [76]. A new version (TDC2) has been built and installed in 2002 to cope with the level of background expected for the luminosity increase of PEP-II. The new circuit has been manufactured at AMS [77] with a $0.6\,\mu$m triple metal technology. Like TDC1, it is a self-calibrating 16-channel microchip which performs three major functions: digitization of the input signal time with 520 ps binning (250 ps resolution rms); and two pulse separation of 33.6 ns; and simultaneous handling of input and output data.

The architecture mixes an analog part that measures the time of the input pulses by means of voltage controlled delay lines and a digital *selective readout* part. The channel rate at which the dead time goes above 1 % is a few MHz. The input signals are selected if they are in time with the L1 trigger after a programmable latency between 64 ns and 16 μs, and within a programmable resolution window, which has a width between 64 ns and 2 μs. Under the present running conditions the resolution is set at 600 ns, which produces a reduction factor of about 20 on the size of the data transferred from the frontend. Events whose output would take longer than the required minimum separation time (2 μs) between successive triggers are truncated and flagged. Simpler and improved diagnostics are provided to flag the overloaded channels in real time.

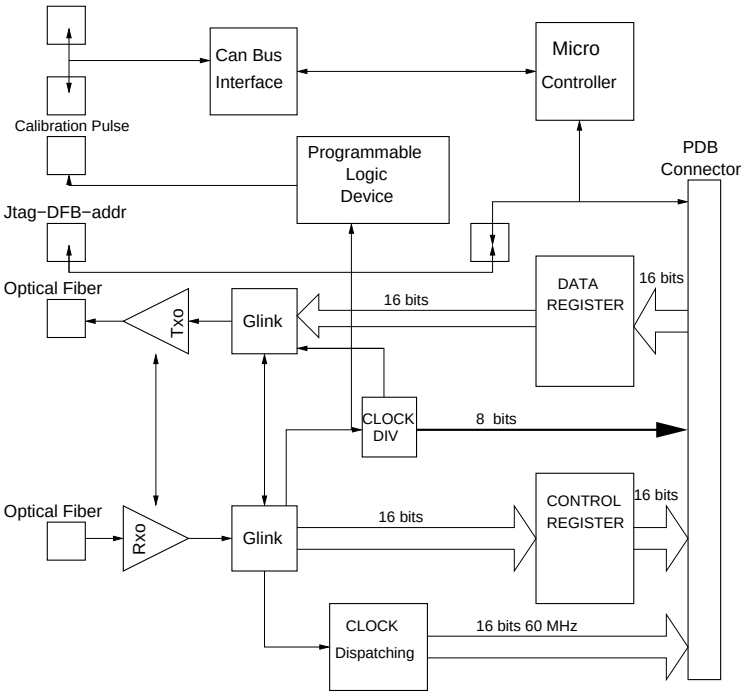

Figure 44. Block diagram of the DIRC Crate Controller.

8.3. DIRC Crate Controller

Each of the twelve DIRC crates hosts a DCC and a specific PDB for the back-plane. These two boards interface the Giga-Link [78] (G-Link) fiber optics from the six readout modules in the DIRC data acquisition system to the DIRC Front-End crates. The DCC comprises mainly the G-Link section and the monitoring section. A block diagram of the DCC function is shown in Figure 44. All signals in the G-Link section are in differential ECL; these are transmitted on impedance matched lines, equipped with resistive termination. The DCC is equipped with a locating pin to ensure installation in the correct slot.

8.3.1. G-Link section

The optical transmitter/receiver from Finisar [79] converts the optical signal, coming from the control fiber, to an electrical signal. Then, the G-Link receiver demultiplexes this 1.2 GHz control stream into 16 bit/60 MHz control words and recovers the 60 MHz control clock. The control words are clocked, buffered and sent to the PDB. A Programmable Array Logic circuit [80] generates the control and data clocks, necessary for the DCC and the DFBs. Three Roboclocks [81] fan out the clock pulses and filter their jitter before sending them to the PDB. After clock recovery in the receiver chip, the clock jitter is 124 ps rms; this was measured at the end of 30 m fiber and in the presence of data exchange.

The data words, coming from the PDB are clocked at the DCC input. Then, the G-Link transmitter multiplexes these 16 bit/60 MHz data words and the 60 MHz data clock to a 1.2 GHz data stream. The optical transmitter/receiver converts electrical signal to optical signals, sent in the data fiber. Both G-Link chips perform error detection, link control and resynchronization.

8.3.2. Monitoring section

The DCC monitors the FEE efficiency. The link with the DETector CONtrol (DETCON) is done via CANbus [82], at 250 kb/s. A microcontroller [73] converts the low voltages (5 per DCC, 7 per DFB) and temperatures (1 per DCC,

1 per DFB), reads the optical link status, counts the serial link errors and sends the monitored values through the CANbus. For the external sensor's signal conditioning (3 temperature sensors), the DCC uses an Electrically Programmable Analog Circuit (EPAC) [83].

A state machine, implemented in a programmable MACH231 circuit [84], decodes the commands transmitted on the G-Link controls. This circuit generates a 16 ns wide digital pulse when a "calibration" command occurs. This pulse triggers the light pulser for the DIRC calibration. A programmable delay line [85], set by the "delay vernier" command, adjusts a delay from 0 ns to 250 ns with 0.5 ns steps.

8.3.3. Protocol Distribution Board

The PDB distributes the control word, data word and one bit control clock, to each of its 16 DFB connectors. It also distributes the one bit data clock to two of its 16 DFB connectors.

To guarantee time synchronization for all DFBs in the crate, all lines have the same length, with less than 1 mm difference. For this back-plane, that transports fast signals (edges <1 ns) over long distances ($\approx$ 40 cm), comparison tests between multiwire and stripline technologies were made. As no major differences in terms of crosstalk or signal integrity were found, the standard, and less expensive, stripline technology was chosen.

The PDB is equipped with a four-bit coding-wheel that provides the DCC connector with the crate address. Each DFB connector contains its own, hard-wired, four-bit address (from 0 to 15).

The PDB also distributes all the power lines needed by the DFBs.

9. Online readout and control

9.1. DIRC detector control

The primary function of the DIRC Detector Control system is to provide efficient control of the detector operating parameters, such as HV, LV and gas systems, and real-time monitoring of environmental conditions, such as temperature, humidity and pressure, to ensure safe and reliable operation. However, the control system also plays an important role in ensuring the quality of data by providing the rest of the Online system with information on the status of the detector, and by providing PEP-II with information on the nature and level of the machine backgrounds in the vicinity of *BABAR*.

The Experimental Physics and Industrial Control System (EPICS) [86] is used to control and monitor the detector, environmental conditions, and accelerator parameters. EPICS is a freely distributed software package that includes a real-time kernel running under the VxWorks [87] operating system, drivers for commonly used hardware components (*e.g.,* CAEN, CANbus), and a suite of user applications for control, monitoring, and data analysis. The source code language is C and is available for customization by the user. The EPICS architecture is distributed, with the Input/Output Controller (IOC), the primary component being a Motorola mv177 cpu embedded in a standard VME module, as the fundamental component. The DIRC system employs a network of three IOCs containing roughly three thousand hardware and software channels that record the status of the detector.

9.1.1. Design and implementation

The control system is divided into three logical entities: The HV System; the Front End Electronics system (FEE); and the Utilities System. One IOC is dedicated to each entity for added flexibility and customization. Each section has its own communication bus, between the IOC and the actual hardware, that varies depending on the case. The central *BABAR* Detector Control system is responsible for storing the accumulated data in an Objectivity database [88].

High Voltage System: This part of the system controls and monitors the six daisy-chained CAEN SY-527 HV mainframes through a special protocol (CAENET) provided by the manufacturer. The current, voltage, trip and status of each HV channel are monitored at a rate of 0.1 Hz. In total, 2688 variables are logged into the dedicated IOC. Custom machine code provides automatic DC voltage ramp up and down as well as global ON/OFF for the whole system.

The process of keeping track of all active chan-

nels available for monitoring is automated, using the Perl scripting language, which is also responsible for generating all EPICS related code (databases, display screens and alarms). User intervention is kept to a minimum and the whole system is easily configurable.

Front End Electronics System: Two dedicated CANbus lines are used to monitor the FEE Wiener crates [89] and the FEE boards. The first bus line is responsible for remote switching ON/OFF all crates and monitor the basic functional parameters: low voltage, current, temperature, and fan rates. The second bus controls and monitors all 12 daisy-chain FEE sectors. The status of the low voltages (7/board), the Finisar (optical link) transmitter status, and the temperatures of all DFBs and DCCs are available at a rate of 1 Hz. In total, 1456 parameters are logged to the dedicated IOC.

Utilities System: The last part of the monitoring system concerns the dry nitrogen and water circulation and purification tasks. A dedicated CANbus line is used to communicate with the hardware through a custom made board. Various pressure and flow gauges, at the input and output pipes of the twelve bar boxes, are monitored and the level of humidity is measured for the early detection of water leaks. For the water purification system: the water level inside the SOB is closely monitored; resistivity and pH measurements on both the entrance and exit of the circulation system are set to provide an early indication of impurities in the water.

9.2. Online platform

The acquisition of data from the DIRC FEE is done by six PowerPC based ROMs. Each ROM consists of an i960RP based PMC Card (I960PMC), a triggered personality card, and a controller card. The main purpose of a ROM is to gather event oriented data from its managed FEEs. This task is done by executing the code that extracts, transforms, reduces and monitors output data (feature extraction), then forwarding the results to the next stage in the *BABAR* data acquisition system. In addition, software executed in the ROM allows configuration and control of the Front-End elements by setting registers in the FEEs memory. The six ROMs are connected by 1.2 Gbit/s optical fibers to twelve DCCs that form the interface to the DIRC VME front-end crates.

9.3. Feature extraction

Raw data from the FEE comes as a stream of 32-bit words that comprises: DFB header, TDC header, TDC hits, TDC status, DFB status and a trailer. Regardless of whether TDC hits are available, each DFB and the four TDC chips in each DFB output their Header and Status words. This information is processed in the ROMs by a feature extraction algorithm before being transmitted to the higher level of the event building process.

The sequence of words in the raw data stream is ordered: All TDC data, from each DFB, begins with a DFB Header word followed by a DFB Status word. Feature extraction flattens the hierarchical structure of the raw data into arrays of TDC and ADC data where non-zero TDC and ADC outputs from hit PMTs are accompanied by a 16-bit detector address, which provides the reconstruction software with ROM, DFB, TDC chip and channel numbers for each hit PMT, and thus encodes its physical location inside the DIRC.

Application of the feature extraction algorithm reduces the data volume by roughly 50 % under typical background conditions and also checks for about 25 error conditions that correspond to different levels of data corruption. An appropriate flag is inserted into the feature extracted data whenever errors are detected.

After about four years of data-taking, there is no evidence of any major problems related to either the hardware or software components of the DIRC data acquisition system. The status of the feature extraction output for each event is a part of the *BABAR* Data Quality Monitoring and is monitored by one of the personnel operating the experiment.

9.4. Calibration

A special feature of the *BABAR* dataflow system is that each sub-detector can be run independently in a separate partition. In this mode

the *BABAR* detector can take a short global calibration run and update various constants stored in the conditions database. The specific type of online calibrations to be run by each sub-detector is decided during the configuration transition by an identifier. Each identifier is used to determine what configuration data is to be downloaded into the ROMs from the configuration database, and defines the functionality of the online software.

The DIRC uses two independent approaches for calibration of the unknown PMT time response and the delays introduced by the FEE and the fast control system. The first is a conventional pulser calibration. The second uses reconstructed tracks from collision data.

The pulser calibration is performed online by executing software directly in all 6 ROMs simultaneously. This calibration is performed by using a light pulser system to generate precisely timed 1 ns duration light pulses from one blue LED per sector. The LEDs are triggered by the global fast control a calibration strobe command sent to the DCCs. The DCC triggers an individual LED for each sector upon receipt of calibration strobe. Pulses in adjacent sectors are staggered by 50 ns to avoid crosstalk between sectors. The pulser is run at roughly 2 kHz for the time delay calibration. The LED light is transmitted through approximately 47 m-long optical fibers to diffusers mounted on the inner surface of the SOB wall opposite the PMTs. The light produces about 10 % photoelectron occupancy, which is nearly uniform throughout the SOB.

Histograms of TDC times for each PMT are accumulated in parallel in the ROMs, and then fit to an asymmetric peak function.

About 65,000 light pulses are used to determine the mean time delay of each of the PMTs; a fit of a skewed Gaussian to the TDC distribution yields a statistical uncertainty of around 0.1 ns on the mean. The LED pulser is also used to monitor the phototube gains using the ADC readout. As with the TDC calibration, histograms and fits of the ADC spectra are accumulated and fit in the ROM.

At the end of each online calibration run, fit constants obtained for each DIRC channel and a calibration time-stamp are copied into the file system of one of the offline computers (a large cluster of commodity computers, PCs, running the UNIX operating system). Once it is offline, data is converted into a collection of data objects that can be directly stored into the Objectivity database. Before being loaded, the values of constants for each channel are validated against previously stored values. If more than 5 channels in two DIRC sectors fail the validation, the results are discarded, and experts are notified.

The whole calibration sequence, including online histogram accumulation, fits, data transfer, validation and database storage, takes from three to seven minutes, depending on the specific configuration. Typically, online calibrations are run once a day to verify the time delays and also are a sensitive probe of hardware failures.

The data stream calibration uses reconstructed tracks from the colliding beams experimental data. For calibration of the global time delay, the observed, uncalibrated times minus the expected arrival times, Δt_γ, are collected during the online prompt reconstruction processing. To calculate individual channel calibrations, Δt_γ values for each DIRC channel are accumulated until statistics equivalent to 100,000 tracks are collected. The distribution for each channel is fit to extract the global time offset calibration.

The data stream and online pulser calibrations of the electronic delays, and of the PMT time response and gain, yield fully consistent results. The data stream results in 15 % better timing resolution than the pulser calibrations. The time delay values per channel are typically stable to an rms of less than 0.1 ns during a year of running.

10. Detector simulation and event reconstruction

Simulation in *BABAR* is done in two distinct stages. First, particles are created from one of the standard event generators such as Pythia [90] and EvtGen [91]. They are then tracked through *BABAR*, recording information on the interactions between the particles and the elements of the various detectors. For the DIRC in particular, information on position, momentum and time is recorded for intersections of all charged tracks

with the boundaries of the fused silica bars and the water in the SOB, in which Cherenkov radiation may be produced. In the second stage, this information is used to simulate the appropriate responses for the detectors. In the DIRC, Cherenkov photons are generated along each track segment identified in the first stage as being in an active medium, and each of these is traced to the point where it is either detected by one of the PMTs or lost by one of the mechanisms described below. For those that reach a PMT, the expected TDC readout is created and recorded in the same format as real data. Finally, background events from PEP-II beam crossings for which the detector is read out at random intervals, independently of the normal trigger conditions, are overlaid.

The "raw" data from the complete simulation event is passed to a third stage, the *BABAR* event reconstruction program, configured to accept simulated data since there are some structural differences from the detector readout data. The three stages can be performed separately, with intermediate output in the Objectivity [88] database, or performed sequentially within a single program.

10.1. Geant4 material simulation

Particle tracking in the first stage is done using the CERN program Geant4 [92] designed to provide a detailed simulation of interactions, decays, bremsstrahlung and other physical processes related to the passage of particles through matter. Secondary products of these processes (δ-rays, photons, *etc.*) are tracked in the same way until all particles stop or (in the case of photons) are absorbed. Particularly in the DIRC materials, Geant4 is configured to perform an explicit simulation of δ-rays down to a kinetic energy of 150 keV, and to track electrons down to that same energy before allowing them to stop, so that the Cherenkov radiation of low energy electrons can be simulated down to the threshold.

A representation of the most important elements in the geometry of *BABAR* was built using the tools in Geant4. To achieve the goals outlined, the geometry implemented for the DIRC in this stage emphasized three features:

- accurate position, size and shape information for the quartz radiator bars;
- a description of all properties of the physical DIRC good enough to allow an accurate description of the passage of particles through it;
- parametrization of the kind and amount of material such that a consistent model could be built in the *BABAR* reconstruction software.

Geometrical properties for some of the more complex structural elements did not require a precise description, but the distribution and amount of material was carefully inventoried to provide a good representation of the total DIRC material.

Geant4 includes methods for building many standard shapes which can be combined to form most of the DIRC elements. It is also able to attribute to these shapes the properties of most common materials, and allows combinations of properties to represent other materials.

A simplifying assumption made both in simulation and in reconstruction is that the radiator bars and wedges all have the same width. In practice, there are bar to bar differences, and variations of order 1 mm in the total active width of a sector, but dimensions and properties that provided a reasonably accurate average are implemented. A perfect rectangular box shape is used with cross sectional dimensions (determined by the average dimension of the real bars) 3.454 cm $\times$ 1.700 cm and the physical properties of fused silica are used. In Geant4, there is no elemental shape that is completely suitable to describe the SOB detector surface (the PMTs), so each of the 12 sectors in the water volume is defined with its curved end approximated by 8 flat surfaces at equally spaced angles azimuthally with respect to the DIRC axis. Since there are no active detector components behind the DIRC PMTs the fact that these were not modeled in detail has negligible impact on the quality of the simulation.

Structural elements included in the description of the material model are (see Section 2.2.2): the CST with inner and outer skins; tracks that carry the bar boxes (approximated with rectangular cross section); bar boxes of rectangular cross-

section, which contain the fused silica (with some averaging of material); annular bulkheads (plane annuli with rectangular extrusions for bar boxes); axial supports (I-beams); end plate (an annulus at the downstream end of the CST) and a stainless steel SOB outer volume. Some details of the support structure of the bar boxes within the CST are suppressed, though the total amount of material is included in the model.

10.2. Simulation of the DIRC detector response

Simulation of the Cherenkov response of the DIRC is done in a second stage using a separate geometrical model of the detector developed by *BABAR* to facilitate swimming of tracks through the detector using a Kalman filter [93]. The same data are used for this description as for the Geant4 model so that, in particular, the active Cherenkov media (fused silica and water) are consistently located in both models.

The basic input for the Cherenkov photon generation procedure is the history, described above, of the steps of all charged tracks (including δ-rays above threshold) made during the Geant4 simulation stage in the active media.

Although background events from random PEP-II beam crossings are overlaid on Monte Carlo events, the background rates seen in practice are low enough that losses of PMT hits due to background hits close in time to real hits can be neglected so this effect is not simulated.

10.2.1. Cherenkov photon generation and transport simulation

At each track step, a test is made to check that the particle is above Cherenkov threshold in the medium. For this purpose, an average refractive index (1.473 for fused silica) is used within the limits determined by the quantum efficiency of the PMT photocathodes. If it is above threshold, the mean path-length between Cherenkov photons is calculated and the parameters to perform a helical interpolation of the track from one photon emission point to the next are determined.

The Cherenkov photon production and propagation process takes account of dispersion in the medium and the multiple scattering of the charged particle traversing it. Each step length along the helix is generated according to an exponential distribution, until the end of the Geant4 step is reached. The Cherenkov photon energies are generated as a uniform distribution convoluted with the quantum efficiency of the PMT bi-alkali photocathode. After accounting for multiple scattering of the track, the photon is generated uniformly around the Cherenkov cone and transported until detected by a PMT or lost as described below. The polarization of the Cherenkov photons is not included in the simulation because they become effectively unpolarized after multiple reflections in the bars.

The transport of photons assumes "perfect" bar and wedge geometry, but takes into account losses from the effects enumerated below. The time of arrival of each detected photon at a PMT is calculated using the dispersive group velocity in each medium – not the phase velocity (which determines the Cherenkov angle).

Many effects contribute to loss of photons, and losses are simulated as a function of wavelength wherever data is available; in some cases, only sparse data are available and *ad hoc* models are used [94]. In the case of fused silica and water, excellent measurements are available for the refractive index and a function fitted to these data is used in both cases. For timing, the group velocity is computed analytically from the refractive index parametrization.

The following effects are taken into account in the simulation: bulk absorption in both fused silica and water; losses at total internal reflection; imperfect reflection at the forward aluminium mirror; and Fresnel reflection at glue joints and the interface between fused silica and water. Cherenkov photons that are not trapped in the radiator bar are assumed lost, and, to be detected must exit the wedge directly into the window and the SOB water.

Figure 45 shows the optical bandwidth of the DIRC detector for a typical Cherenkov photon emitted by a particle at 90° polar angle in *BABAR*. Contributions to the bandwidth include [94]: bar and water transmission, mirror reflectivity, internal reflection coefficient (assuming 365 bounces), glue transmission and PMT quantum efficiency,

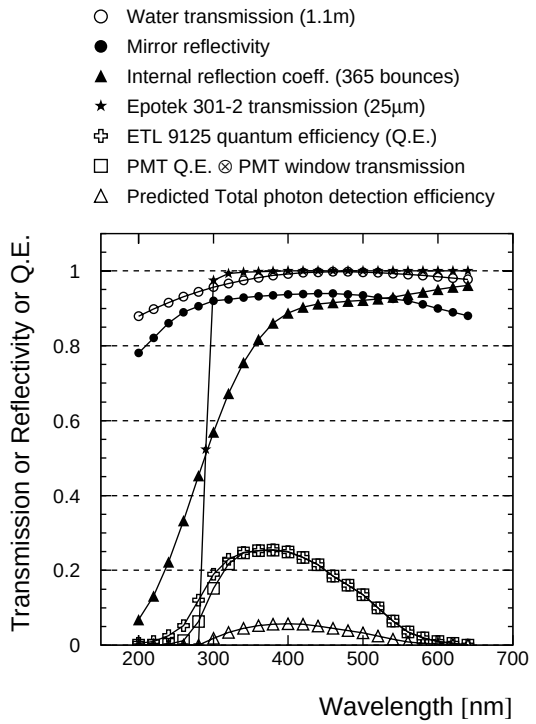

Figure 45. Contributions to the photoelectron detection efficiency for a track perpendicular to the fused silica bar located in the middle of the *BABAR* sensitive area.

and window transmission.

One can see that the lower end of the bandwidth is close to 300 nm, mainly due to the glue transmission properties. Although this reduces the number of photons that are transmitted, the reduction in the chromatic error contributions to the overall Cherenkov angle and timing resolution more than compensates for the increase in statistical error due to the loss of photons. Insensitivity to shorter wavelengths also relaxes construction tolerances such as bar surface smoothness.

10.2.2. Comparison of DIRC performance with data

For di-muon events, the simulated resolutions per Cherenkov photon and per track agree with data at better than the 10 % level. The average number of observed photons as a function of the muon polar angle is also in good agreement, as shown in Figure 46. This average is as low as 17 for some polar angles near 90° but exceeds 50 at the forward and backward edges of the acceptance.

Qualitatively, the shape of this distribution can be understood from the geometry of the DIRC, as follows. The number of Cherenkov photons varies with the path-length of the track in the radiator, which is smallest at perpendicular incidence and increases towards the ends of the bars, with more photons detected in the backward direction than the forward since they have a shorter path length to the PMT's. In addition, the fraction of photons trapped by total internal reflection generally rises with larger values of $|\cos\theta_{\rm track}|$, except close to 90° where a fraction of both forward- and backward-going photons can be trapped, leading to an enhancement of the trapping efficiency. The overall increase in the number of photons for forward going tracks is a good match to the need for better resolution at larger momentum and thus benefits the DIRC performance.

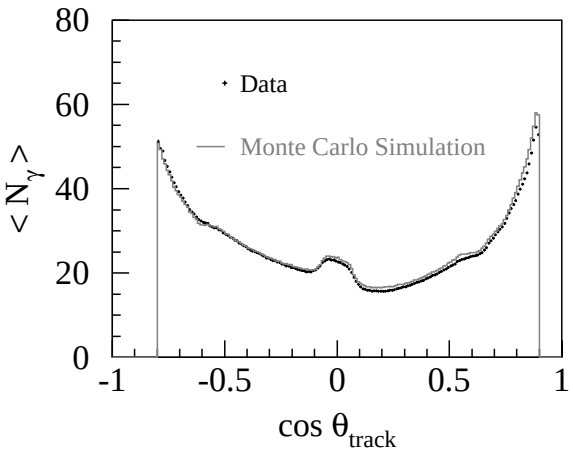

Figure 46. Average number of detected photons versus track polar angle for reconstructed tracks in di-muon events compared with Monte Carlo simulation.

Comparison of multi-track Monte Carlo control samples with real data demonstrates that there

is generally slightly more background in the real detector than our Monte Carlo simulates. Studies show that this extra background, a few percent additional hits, appears to be correlated with tracks, but so far the mechanism has not been identified. In particular, one potential source of inconsistency, the simulation of δ rays, seems to be correct and is not believed to be the source of the discrepancy.

10.2.3. *BABAR* DIRC N_0

The parameter N_0, commonly used to characterize the photon detection efficiency of Cherenkov detectors, is defined by

$$N_0 = \frac{z^2\alpha}{\hbar c}\int_{E_1}^{E_2}\prod_i \epsilon_i(E)\ dE,$$

where the range E_1 to E_2 is the bandwidth of the detector, and the ϵ_i are the individual contributions to the photon detection efficiency, so that $\prod_i \epsilon_i(E)$ gives the overall detector efficiency ϵ. If there are no strong chromatic dependencies for the refractive index and detection efficiencies, the Frank-Tamm equation (Section 2.1.1) can be factored into the simple form

$$N_{pe} \approx N_0 L \sin^2\langle\theta_C\rangle,$$

where $\langle\theta_C\rangle$, is the Cherenkov angle averaged over the bandwidth of the detector.

The value of N_0 extracted from the data and Monte Carlo (Figure 46) for a track entering perpendicularly to the bar is approximately 25 cm^{-1}. An estimate for this parameter may also be derived from a numerical integration [94] of the efficiencies shown in Figure 45. This method yields, for the same track parameters, $N_0 \approx 31$ cm^{-1}. The data, Monte Carlo and the numerical integration are consistent at the level of approximately 20 %.

In practice, a single value for N_0 is not sufficient to fully characterize a complex Cherenkov detector. For example, using the Monte Carlo, the calculated value for N_0 varies from a low of 17 cm^{-1} (for a track polar angle 78°), to 28 cm^{-1} at the forward edge of the DIRC acceptance, to a maximum of 34 cm^{-1} at the backward edge of the DIRC acceptance.

10.3. Reconstruction

Reconstruction in the DIRC uses the charged track information provided by the tracking detectors, along with the position of the PMT hits. The time measurement of these hits is also an important factor, used primarily to reduce ambiguities and suppress backgrounds.

Two different algorithms are used in the reconstruction. The first one gives a measurement of the Cherenkov angle, track by track, while the second uses the information of the whole event globally to perform particle identification. Both are described below in more detail.

10.3.1. Reconstruction of Cherenkov photons

This is the first step of the DIRC reconstruction. The emission angle and the arrival time of the Cherenkov photons are reconstructed from the observed space-time coordinates of the PMT signals, transformed into the Cherenkov coordinate system (θ_C, ϕ_C) in the following way. The known spatial position of the bar through which the track passed, and the PMTs whose signal times lie within the readout window of $\pm$ 300 ns from the trigger, are used to calculate the three-dimensional vector pointing from the center of the bar end to the center of each tube. This vector is then extrapolated into the radiator bar using Snell's law. Together with the track direction, this procedure defines the angles θ_C and ϕ_C of a photon, up to a 16-fold ambiguity that are determined by: the last vertical reflection from the top or bottom of the bar; the last horizontal reflection from the left or right side of the bar; the last reflection from the top side of the wedge or not; and by reflection from the forward mirror or not.

The resolution on the measurement of the photon $\Delta\theta_{C,\gamma}$ is illustrated in Figure 47(a). There is a broad background of less than 10 % relative height under the peak, that originates mostly from track-associated sources, such as δ rays, and combinatorial background. The width of the peak translates to a resolution of about 9.6 mrad, in good agreement with the expected value.

The DIRC time measurement represents the third dimension of the photomultiplier hit re-

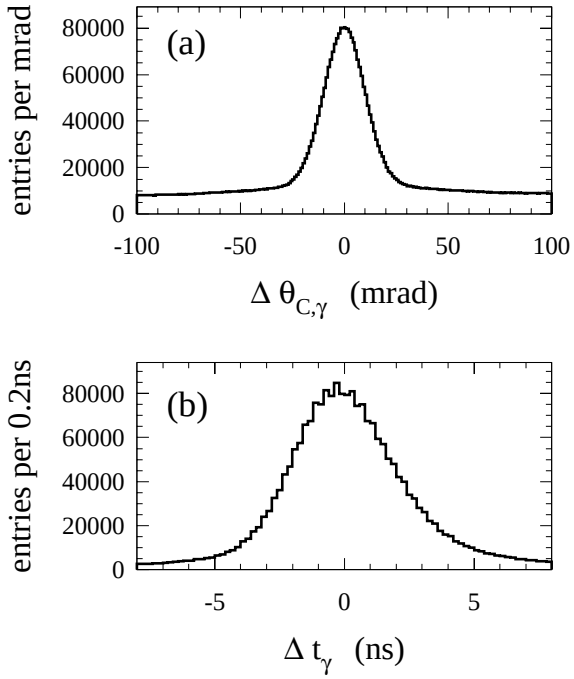

Figure 47. The difference between (a) the measured and expected Cherenkov angle for single photons, $\Delta\theta_{C,\gamma}$, and (b) the measured and expected photon arrival time, for single muons in $\mu^+\mu^-$ events.

construction. Though the timing resolution is not competitive with the position information for Cherenkov angle reconstruction, timing information is used to suppress background hits from the beam induced background and, more importantly, exclude other tracks in the same event as the source of the photon. The information is also used to resolve the forward-backward and wedge ambiguities in the hit-to-track association.

The relevant observable to distinguish between signal and background photons is the difference, Δt_γ, between the measured and expected photon arrival time, shown in Figure 47(b). The expected photon arrival time is calculated for each photon using the track time-of-flight assuming it to be a charged pion, and the photon propagation time within the bar, the wedge and the water-filled SOB. The measured photon arrival time is obtained from the recorded time of the candidate signal in the PMT, after calibration using the online channel-by-channel calibration described in the previous section and a global offset determined run-by-run by a data stream calibration. Note that in this way the measured photon time is referenced to the DIRC mean event time, which gives greater precision than that available from the trigger or tracking system. The timing distribution Figure 47(b) is well described by a double Gaussian; the width σ of the dominant Gaussian is 1.7 ns, which is close to the 1.5 ns intrinsic transit time spread of the PMTs.

After making use of the timing information and excluding unphysical photon propagation paths the number of ambiguities is reduced from 16 to typically 3.

10.3.2. Track maximum likelihood fit

The first algorithm currently used in the DIRC reconstruction performs a Maximum Likelihood fit to the value of the Cherenkov angle, θ_C, for every track above Cherenkov threshold if it has at least one associated photon. The relatively large number of about 30 photons detected in the DIRC and distributed on at least half a Cherenkov cone makes it possible to fit not only for the opening angle with respect to the track direction, the Cherenkov angle θ_C, but also simultaneously for the number of signal and background photons. Using also the error of the Cherenkov angle found by the fit, particle identification selectors are then used to convert that information into a set of five *a posteriori* track likelihoods, L_j ($j = e, \mu, \pi, K$ and p), by calculating the Gaussian and Poissonian probability density functions for each hypothesis to agree with the combination of the Cherenkov angle and the number of photons found for that track.

Ring fitting algorithms, such as this maximum likelihood fit, are most effective when a ring is present and a Cherenkov angle measurement is needed, *i.e.,* for detector performance or alignment studies. In the region of the Cherenkov threshold, where none or very few Cherenkov photons are found, a "veto mode" algorithm uses the information that some particle hypotheses are constrained by the absence of photons when some

are expected. This fitting algorithm is less accurate and is difficult to implement in a consistent likelihood scheme, due to the different response for each of the particle hypotheses above and below threshold. In addition, the algorithm is forced to make a choice of a seed value for θ_C, which can lead to wrong results when the number of photons is small, or the background is high. In such cases, the phase space of background photons tends to bias it towards large θ_C values. When properly optimized, the Global Likelihood algorithm, described below, guarantees a smooth behavior through the thresholds. The main disadvantage of this second strategy is that it does not provide a direct measurement of the Cherenkov ring angle.

10.3.3. Event global likelihood algorithm

The second reconstruction procedure is based on an unbinned maximum likelihood formalism that incorporates all information provided by the space and time measurements from the DIRC for an entire event.

The result of the algorithm is a likelihood value for each of the five stable particle types (e, μ, π, K, p). These likelihoods are calculated in an iterative process at the level of the PMT hits, by maximizing the likelihood value for the entire event while testing different hypotheses for each track. It takes into consideration the machine background as well as all the tracks in an event as backgrounds for each other, and explains all observed photons in the DIRC as the result of either background or Cherenkov signal due to a track with a given particle hypothesis. An "event likelihood" is, by definition, the overall probability of there being N detected photoelectrons and those photoelectrons being distributed in the Cherenkov angle and time space as they were found. The input into the likelihood is the reconstructed Cherenkov angle of each PMT hit and its measured time. The five likelihoods L_j are calculated for each track while holding all other tracks at their current best hypothesis.

The global likelihood algorithm is quite complex, since it needs information from all tracks in the event to calculate the likelihood for any other track (any track is background for any other). A similar algorithm was used successfully in the SLD experiment [95].

The observables used in the calculation of the global likelihood for N_γ associated PMT hits (*photons* in the following) are:

- $\Delta\theta_C^{ij}$, the difference between the measured Cherenkov angle θ_C^i for each photon ($i = 1 \dots N_\gamma$) that is associated with a given track and the expected track Cherenkov angle θ_C^j for any of the five hypotheses ($j = e, \mu, \pi, K$ and p);
- Δt_γ^i, the difference between the measured and expected photon arrival time, calculated for each photon ($i = 1 \dots N_\gamma$) assuming the track to be a charged pion for its time-of-flight.

The signal likelihoods for the five hypotheses are derived for each PMT hit from the $\Delta\theta_C$ and Δt_γ information, assuming Gaussian distributions. The angle and time resolutions are derived from analysis of real data and fixed in the algorithm. The signal likelihood contributions from the ambiguities of each photon are summed.

The background contribution for each photon has two components:

- The machine background, which is modeled as random although the distribution is not truly random in the DIRC;
- the background from other tracks.

The first contribution is calculated event by event, averaged over each sector, summing over all hits which cannot be associated with any track with the current best hypothesis. This is realized with a cut on the minimum value of the likelihood needed for any of the PMT solutions to be categorized as belonging to a Cherenkov ring.

The second contribution is calculated, hit by hit, by summing over the likelihood contributions from all other tracks, using their current best hypothesis.

The PMT hit likelihoods (signal + background) are multiplied together to give each track a total likelihood for each hypothesis. The hypothesis with the highest likelihood is chosen as the best

for that track. If, for any track, the best hypothesis changes after an iteration, the algorithm is repeated on the whole event with the new best hypotheses up to a maximum of three complete iterations, at which point the best hypothesis and the five likelihoods are retained.

If the likelihood for a given PMT hit to be a signal from a specific track exceeds its likelihood to be due to background, it is considered to be a signal photon. The number of signal photons for each track is saved and can be compared to the expected number of photons, assuming a Poisson distribution, for each particle hypothesis, which is found in a look-up table. This so-called "ring dictionary" is based on the simulated response of the DIRC to a particle of type j with the observed momentum, polar angle and charge. In practice (see Section 12), the output of both algorithms is used in PID selectors.

10.3.4. Alignment

In the early data taken by the DIRC one of the main sources of error on the Cherenkov angle θ_C was due to poor alignment of the detector components. Since measurement of the Cherenkov angle requires knowledge of the direction of both the reconstructed track and of the Cherenkov photons with a precision of a few milliradian, the DIRC performance was degraded not only by inaccurate knowledge of the position of the DIRC but also systematic errors in the tracking system. In practice, systematic effects in the Silicon Vertex Tracker dominated, since this represented the major contribution to uncertainty in the measurement of the track polar angle. The internal alignment of the DIRC was divided into two parts: the transverse and longitudinal alignments.

The transverse alignment allowed a more precise determination of the azimuthal angles ϕ_C and the number of Cherenkov photons, but had only a second order effect on the measurement of the photon Cherenkov angle θ_C. Alignment of the bars in the transverse plane, using optical measurements performed during the detector construction, improved the track θ_C resolution by 0.04 mrad.

The longitudinal alignment of the DIRC had a much greater effect. For each radiator bar, the possible misalignments are of two types: either a global translation or rotation of the bar, or mechanical deformations of the bar (for example, a misalignment of any of the four bar segments at the glue joints). The reconstruction code can correct quite easily for global misalignments, but not for deformations, since bars are defined to be perfect solids. Unfortunately, studies of θ_C residuals as a function of the track polar angle demonstrated that global corrections to the bar positions and orientations were not enough to obtain a good alignment.

To solve that problem, a table was constructed that provides the correction amount to be applied to each photon as a function of several parameters: the bar number and the unit vector for the photon direction in the bar frame; whether there is reflection from the mirror; whether there is reflection from the top surface of the wedge; whether there is reflection from the left or right surface of the wedge. This correction table is calculated from a large sample of di-muon events and greatly reduces the bias on track θ_C for all bars and improves the single photon resolution. Using this table reduces the overall θ_C resolution per track by typically 0.2 mrad, to approximately 2.4 mrad.

11. Operational issues

Soon after the DIRC was fully commissioned in late 1999, it achieved performance close to that expected from Monte Carlo simulation and has been running efficiently and reliably. The system has been robust and stable, and, indeed, serves also as a background detector for PEP-II tuning. After over four years of running, nearly 99 % of PMTs and electronic channels are operating with nominal performance.

11.1. Backgrounds

Figure 49 shows a typical di-muon event ($e^+e^- \rightarrow \mu^+\mu^-$). In addition to the signals caused by the Cherenkov light from the two particles, about 500 background signals can be seen in the 600 ns readout window centered about the trigger. This background is due to low energy photons and neutrons from PEP-II hitting the

SOB, and its associated water and metal components.

The TDC chip used in the DIRC data readout through 2002 (see Section 8.2.2) is designed such that a dead time of about 5 % occurs at an input rate of 250 kHz. During data taking some care in machine tuning is required to stay under a limit of 250 kHz/tube.

To monitor the limiting rate, one PMT in each sector is read out via a scaler. Figure 48 shows the maximum scaler rate as a function of the PEP-II luminosity during data taking in 2000 and 2001. In March 2000 the accelerator operated at a peak luminosity of $1\times10^{33}/\mathrm{cm}^2\mathrm{sec}$. Figure 48(a) shows that, at a value that corresponds to only one third of the design luminosity, the PMT rates reached a level that caused noticeable dead times.

Due to those findings, lead shielding was installed in the summer of 2000 around the beam line components near the backward endcap. Initially, localized shielding was added in the form of lead bricks that were stacked around the beam pipe and in front of a large quadrupole magnet. This shielding significantly improved the background situation so that noticeable TDC dead times were reached only at $2.5\times10^{33}/\mathrm{cm}^2\mathrm{sec}$ (Figure 48(b)).

During the shutdown in January 2001, the localized lead brick shielding was replaced by an engineered, homogeneous lead shielding of 5 cm to 8 cm thickness that covers the inside radius of the SOB and is easily removable to facilitate access to the central detector and beam line components. Figure 48(c) shows that at luminosities of $4.2\times10^{33}/(\mathrm{cm}^2\mathrm{sec})$ the maximum scaler rates are well below the level that would cause TDC inefficiencies.

During the shutdown that followed the 2001-2002 run, the TDCs were replaced with a faster version with deeper buffering capable of accepting a 2.5 MHz input rate with less than 5 % dead time. Based on the projected increase in PEP-II luminosity through 2010 the new TDCs are not expected to suffer from any significant dead time due to accelerator induced background during the lifetime of the experiment.

The effect of the accelerator induced background on the DIRC reconstruction can be efficiently reduced using the time information. The requirement that the difference between the measured and expected photon arrival time, $|\Delta t_\gamma|$ (see Section 10.3), be less than 8 ns substantially improves the correct matching of photons with tracks and reduces the number of accelerator induced background signals by approximately a factor 40, as illustrated in Figure 49.

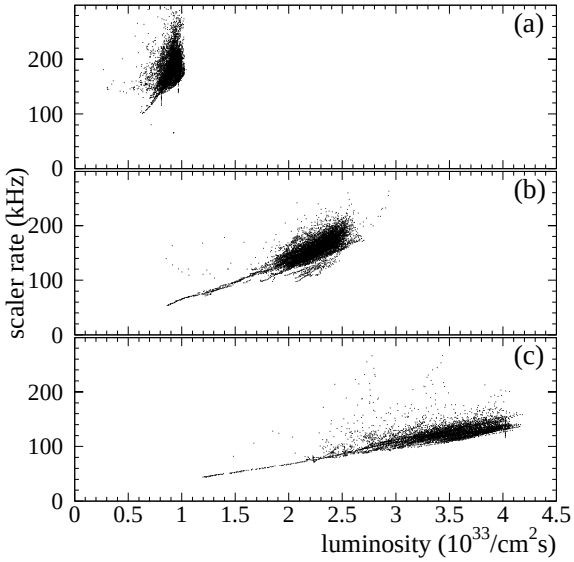

Figure 48. Maximum scaler rates measured for three different accelerator and shielding configurations in March 2000 (a), October 2000 (b) and August 2001 (c).

11.2. Photon yield

Loss of photon detection efficiency can arise from the corrosion of PMT front glass windows, discussed in Section 6, as well as from possible deterioration of the water transparency or pollution of bar or window surfaces. Direct measurements of the number of Cherenkov photons observed in di-muon events as a function of time can be used to determine any degradation of the photon yield. An analysis using di-muon events from late 1999 through November 2003 shows a photon loss of (1.5 ± 0.2) %/year. There is no significant dependence of the loss rate on the radiator bar number or the location of the Cherenkov ring in the PMT

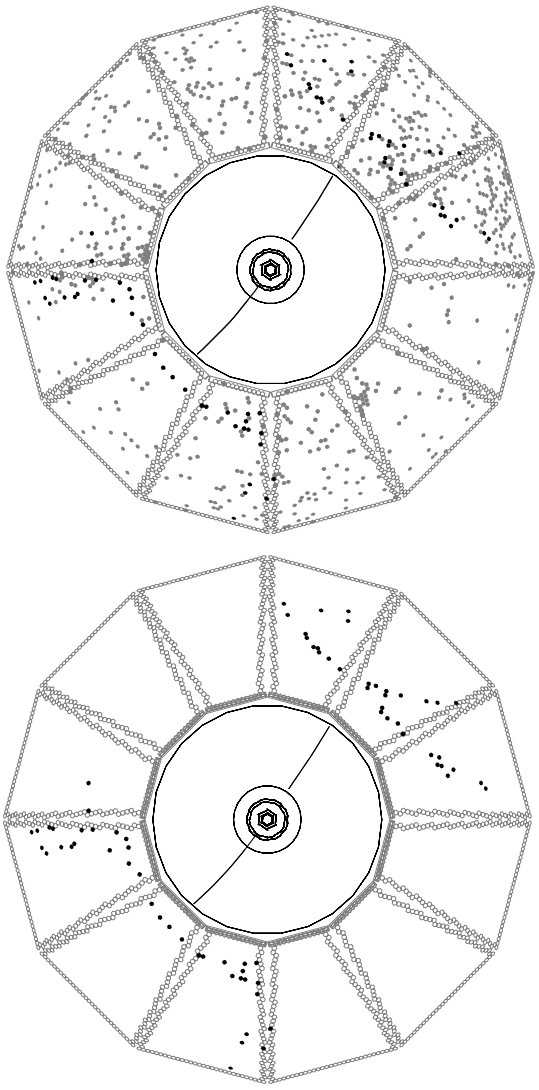

Figure 49. Display of an $e^+e^- \to \mu^+\mu^-$ event reconstructed in *BABAR* with two different time cuts. On the top, all DIRC PMTs with signals within the ± 300 ns trigger window are shown. The dark dots are signals due to the muons; the gray dots are from backgrounds. On the bottom, only those PMTs with signals within 8 ns of the expected Cherenkov photon arrival time are displayed.

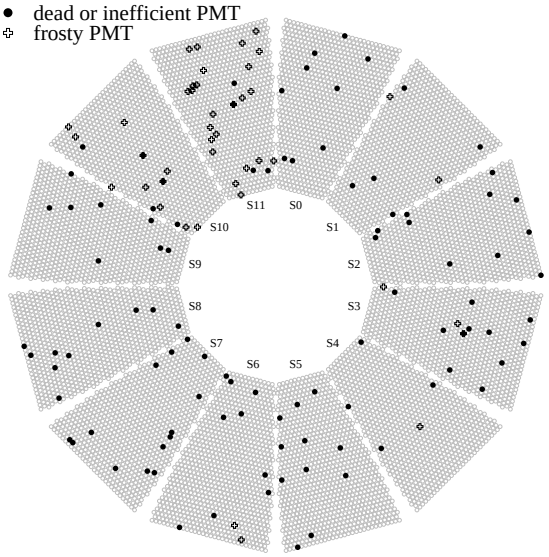

Figure 50. Location of *frosty* PMTs and dead or inefficient electronics channels.

plane.

The reason for the loss in photon yield is not fully understood. The observed PMT glass corrosion, resulting in "frosty" tubes, affects too small a number of them to be a significant effect. Nevertheless, even if the deterioration continues at the rate of 1.5 %/year, the impact on the particle identification power of the DIRC is small. For instance, after 10 years the π/K separation at 3.5 GeV/c momentum would go from the current value of 3.5 standard deviations to 3.2 standard deviations.

11.3. PMT failures

Although detailed tests were performed to verify that the PMTs could withstand the highly corrosive action of ultra-pure water, the operation of the 10,752 PMTs for the 10 year expected lifetime of the DIRC remains a concern, as discussed in Section 6.4. Nevertheless, in the five years since the PMTs were first immersed in the water, only about 150 channels have failed. Figure 50 shows the location of all dead or inefficient PMTs in the PMT plane. The PMT failures appear to be randomly distributed and not correlated with the location of the frosty PMTs. The primary fail-

ure mode of the PMTs is loss of vacuum at the base of the glass envelope, perhaps due to stress cracks, which has no clear connection with the glass corrosion effects discussed earlier.

When a gas or vapor leaks into a PMT, it may be ionized by electrons in transit between dynodes, this may be followed by emission of light causing photoelectron production in that PMT and others nearby. So, when a PMT fails due to a vacuum leak, it may cause counting rates at the MHz level in the failing PMT and several hundred kHz in its close neighbors. The DIRC detector control is configured to reduce automatically the voltage of any group of PMTs that is drawing significantly larger than normal current to prevent deterioration of the DIRC data due to one failing PMT. Since every HV channel controls 16 PMTs, the failure of a single PMT causes the entire group of 16 PMTs to be lost until an access to the detector allows removal of the HV connector to the failed PMT and subsequent restoration of the nominal voltage to the remaining 15 PMTs. This type of failure, however, is a rare process that occurs on average once every two to three months.

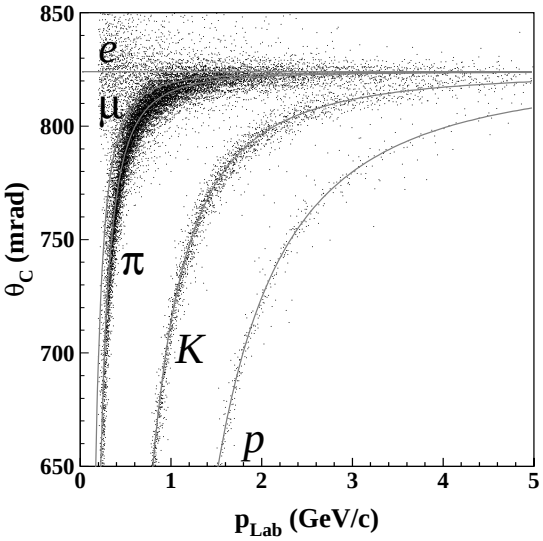

Figure 51. The fitted Cherenkov angle of tracks from an inclusive sample of multi-hadron events plotted against the momentum of the tracks at the entrance to the DIRC bar box. The grey lines are the predicted values of the θ_C for the different particle species.

12. Performance

Since the inclusive branching fraction $B^0 \to K^+ X$ is about 78 % [96], K/π separation is essential for the physics program of *BABAR*. The DIRC plays a central role in final state selection and B meson flavor tagging for *CP* measurements. This section provides an overview of the physics performance followed by examples of physics analyses where the particle identification information from the DIRC is important to the precision of the measurement.

12.1. Overview of performance

In the absence of correlated errors, the resolution ($\sigma_{C,track}$) on the track Cherenkov angle should behave as:

$$\sigma^2_{C,track} = \sigma^2_{C,\gamma}/N_\gamma + \sigma^2_{\rm track} \ ,$$

where N_γ is the number of detected photoelectrons, $\sigma_{C,\gamma}$ is the single photon Cherenkov angle resolution and $\sigma_{\rm track}$ is the uncertainty of the track direction in the DIRC. The average value of N_γ, shown in Figure 46, varies between about 17 for tracks with nearly perpendicular incidence to nearly 60 for polar angles towards the forward and backward regions. The increase in the number of photons for tracks in the forward direction compensates for the reduced average separation in the Cherenkov angle for different particle hypotheses due to the increased track momenta in this region.

Figure 51 shows the fitted Cherenkov angle plotted against momentum for a sample of tracks from multi-hadron events. The momentum is that calculated at the track entrance to the DIRC bar box. The bands corresponding to pions, kaons and protons are well separated below 3 GeV/c, which illustrates qualitatively the powerful hadron identification capabilities of the DIRC.

The Cherenkov angle resolution, $\sigma_{C,track}$, for tracks from di-muon events, $e^+e^- \to \mu^+\mu^-$, is

shown in Figure 52. The width assuming a single Gaussian distribution is 2.5 mrad. The resolution is 14 % larger than the design goal of 2.2 mrad, which was estimated from the extensive study of a variety of prototypes, including a beam test [97].

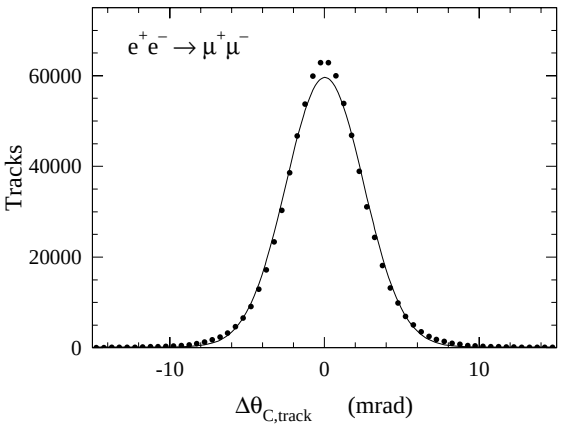

Figure 52. The difference between the measured and expected Cherenkov angle, $\Delta\theta_{C,track}$, for single muons in $\mu^+\mu^-$ events. The curve represents a Gaussian distribution fit to the data with a width of 2.5 mrad.

The $D^{*+} \to \pi^+(D^0 \to K^-\pi^+)$ decay chain[3] is well suited to probe the pion and kaon identification capabilities of the DIRC. It is kinematically well constrained and the momentum spectrum of the charged pions and kaons covers the range accessible by B meson decay products in *BABAR*. Figure 53 shows the $K^-\pi^+$ invariant-mass spectrum from inclusive D^* production. Both tracks are within the DIRC acceptance and at least 10 Cherenkov photons are required for the charged pion hypothesis. The lower peak in Figure 53 shows the same sample after one track is identified as a kaon using the likelihood ratio from the DIRC. The efficiency for correctly identifying a charged kaon that traverses a radiator bar and the probability to wrongly identify a pion as a kaon, integrated over the K and π momentum spectra of the D^* control sample, are about 98 % and less than 2 %, respectively.

[3]Unless explicitly stated, charge conjugate decay modes are assumed throughout this section.

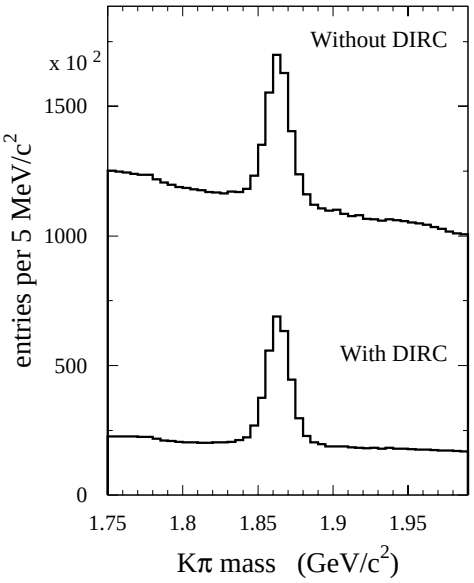

Figure 53. Invariant $K^+\pi^-$ mass spectrum for kinematically reconstructed D^0 mesons in the decay $D^* \to D^0\pi$ as described in the text, without (top) and with (bottom) the use of the DIRC to identify the kaon.

The pion-kaon separation power is defined as the difference of the mean Cherenkov angles for pions and kaons assuming a Gaussian-like distribution, divided by the measured track Cherenkov angle resolution. As shown in Figure 54, the separation between kaons and pions is about 4 σ at 3 GeV/c declining to about 2.5 σ at 4.1 GeV/c.

12.2. Study of inclusive charged pion, kaon, and proton production

An example of an analysis that uses the DIRC event global likelihood algorithm (see Section 10.3.3) is the measurement of the inclusive charged pion, kaon, and proton production cross sections, both on and below the $\Upsilon(4S)$ resonance. The information from the drift chamber (DCH) and DIRC are used to identify clean samples of

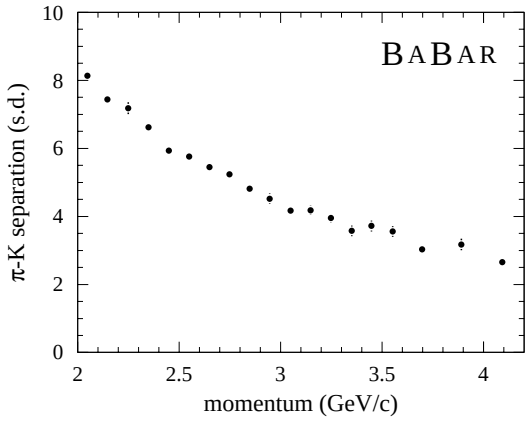

Figure 54. DIRC π-K separation versus track momentum measured in $D^0 \to K^-\pi^+$ decays selected kinematically from inclusive D^* production.

charged pions, kaons, and protons over a wide range of momenta and polar angle in the laboratory frame, corresponding to nearly complete momentum coverage in the e^+e^- center-of-mass system.

The DIRC log-likelihood differences $l_{ij}^{\rm DIRC} = \log(L_i) - \log(L_j)$ with $i,j = (e,\mu,\pi),K$ and p from the global likelihood algorithm give excellent separation for particles with high momenta, but become inefficient for identifying particles near threshold, *i.e.,* protons below 1.5 GeV/c and kaons below 1 GeV/c. The dE/dx measurement from the DCH gives very good separation for low momentum particles, but K-π and p-K separation power drops rapidly above about 0.5 GeV/c and 0.8 GeV/c, respectively. In these intermediate momentum regions the information from the two detectors must be combined to provide optimal performance from the identification algorithms.

To determine the performance in a given momentum range, the 2-dimensional distribution of $l_{K\pi}^{\rm DCH}$ and $l_{K\pi}^{\rm DIRC}$ is plotted. To accommodate tails in both distributions, optimal separation is achieved with a sloped cut in this plane, effectively combining information from the two detectors. To select kaons and reject pions, the line that maximizes the kaon efficiency is found for each momentum bin, subject to the constraint that only 1 % of the pions are incorrectly identified as kaons. This procedure is repeated for the electron and proton backgrounds (the muon signature is essentially identical to that of a pion), and for several misidentification rates. In order to be identified as a kaon, the particle must pass such a linear cut for each of the three background types.

The performance of the detector for identifying tracks passing this selection is quantified in terms of a momentum-dependent identification efficiency matrix $\mathbf{E}$, where each element, E_{ij}, represents the probability that a selected track from a true i-hadron is identified as a j-hadron, with $i,j = \pi,K,p$. Samples of well identified hadrons from $\rm K^0_S \to \pi^+\pi^-$, $\Lambda \to \pi p$, and $D^\star$-tagged $D^0 \to K\pi$ decays are used to crosscheck and calibrate the value of $\mathbf{E}$ obtained from the simulation.

Figure 55 shows the efficiency matrix $\mathbf{E}$ for identifying tracks from simulated $q\bar{q}$ events, within the polar angle region $0.77 < \cos\theta_{\rm track} < 0.88$. The center of the band indicates the efficiencies, and the band half-width is the one standard deviation uncertainty. The efficiencies for correct identification are predicted to be above 99 % in the lowest momentum bins. The ability of dE/dx to separate kaons from pions and protons drops off quickly around 0.5 GeV/c and 0.8 GeV/c, respectively. The effectiveness of the DIRC rises sharply in these regions, because they are just above the relevant Cherenkov thresholds, where both the Cherenkov angles and numbers of photoelectrons detected increase rapidly; the efficiencies reach a plateau of about 95 % well above threshold.

In the intermediate regions, the judicious combination of DCH and DIRC information results in smooth transitions, whereas a sharp dip would be seen if the information from dE/dx to DIRC was simply switched at some value of the momentum. In the plateau regions, the Cherenkov angles differ by much more than the resolution, and the performance is limited by the detection of too few photons at the expected angle because of multiple scattering or poor tracking. The resolution on the measured Cherenkov angle becomes increasingly important at higher momenta, where

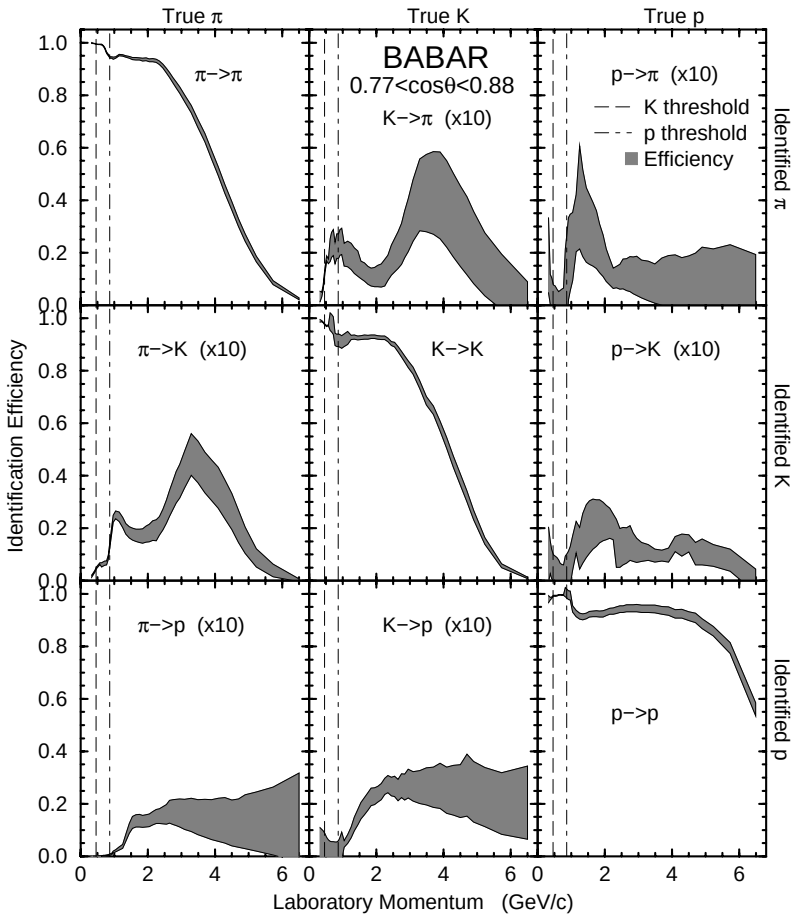

Figure 55. The fully corrected efficiency matrix for the track polar angle bin $0.77 < \cos(\theta) < 0.88$. The width of the bands indicate the uncertainties derived from the control samples.

the Cherenkov angles for different particles converge. The $\pi - K$ separation begins to drop around 2.5 GeV/c, and efficiencies fall below 20 % at $\approx$ 5 GeV/c. Good $K-p$ separation is achieved up to the highest accessible momenta.

The rates for misidentifying a particle as a different type are below the 0.1 % level for the lowest momenta, where $\mathrm{d}E/\mathrm{d}x$ performance is excellent. In the DIRC dominated regions it is typically between 1 % and 2 %; in the intermediate momentum regions there are generally smooth transitions.

12.3. B-flavor tagging with the DIRC

The DIRC makes an important contribution to the flavor tagging in the measurement of the time-dependent CP violating measurements.

The most accurate $\sin 2\beta$ measurement [98,99] uses four B^0 modes to CP=–1 states containing charmonium and a K^0_S: $J/\psi K^0_S$, $J/\psi(2S)K^0_S$, $\chi_{c1}K^0_S$, and $\eta_c K^0_S$. Those tracks not associated with these exclusive decays are used to tag the flavor of the other B meson as a B^0 or a $\overline{B}^0$. Several multivariate algorithms are used to identify the different signatures of B–decays: high center-of-mass momentum electrons or muons from semileptonic B–decays, the charges of iden-

tified kaons in the event, and soft pions from D^{*+} decays. The algorithm that identifies kaons uses the track's momentum and the value of the ratio of the likelihood functions $L_K/(L_\pi + L_K)$ for the SVT, DCH and DIRC as inputs. A neural network, which combines the outputs of the individual B–decay signature algorithms, takes into account the correlations between different sources of flavor information, and provides an estimate of the mistag probability for each event.

Table 8
Efficiencies, ϵ_i, average mistag fractions, ω_i and $Q_i(=\epsilon_i(1-\omega_i)^2)$ values for each tagging category. The combined efficiency and Q values are also given.

Tag	ϵ [%]	ω [%]	Q [%]
`Lepton`	9.1 ± 0.2	3.3 ± 0.6	7.9 ± 0.3
`Kaon I`	16.7 ± 0.2	10.0 ± 0.7	10.7 ± 0.4
`Kaon II`	19.8 ± 0.3	20.9 ± 0.8	6.7 ± 0.4
`Incl.`	20.0 ± 0.3	31.5 ± 0.9	2.7 ± 0.3
Comb.	65.6 ± 0.5		28.1 ± 0.7

Using the outputs of the individual B–decay signature algorithms, and the estimated mistag probability from the neural network, events are assigned to four hierarchical, mutually exclusive tagging categories. The `Lepton` category contains events with an identified lepton and a supporting kaon, if present. The `Kaon I` category contains events with a charged kaon and a soft pion of opposite charge and similar flight direction. The `Kaon II` category also contains the events with a well identified slow pion. Events with only a kaon tag are divided between the `Kaon I` and `Kaon II` category depending on the value of the estimated mistag probability. The remaining events are either assigned to an `Inclusive` category, or rejected from the analysis, based on the estimated mistag probability. Table 8 gives the tagging efficiency, ϵ_i, the mistag probability, ω_i, and the effective tagging efficiency, $Q_i = \epsilon_i(1-\omega_i)^2$, for each of the tagging categories. The statistical error on the measurement of $\sin 2\beta$ is inversely proportional to $\sqrt{\Sigma Q_i}$. Given that the `Kaon I` and `II` have a combined effective efficiency of 17.4±0.6 %, these tagging categories provide 62 % of the statistical power.

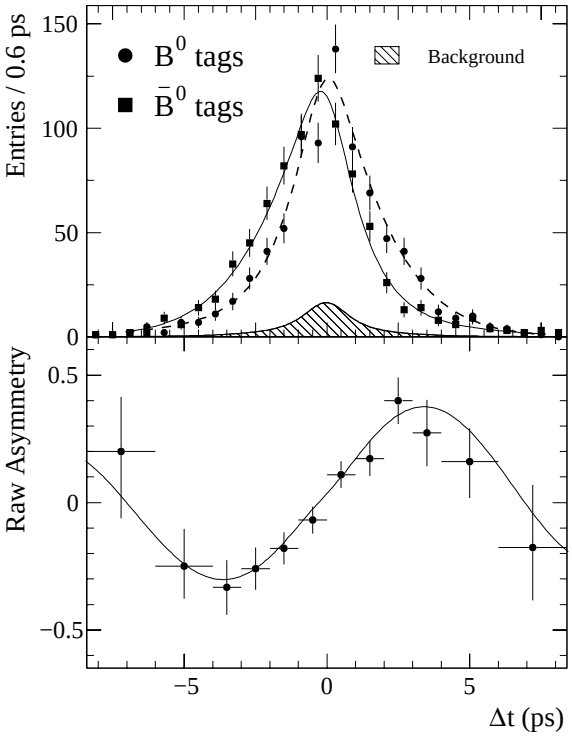

Figure 56. The upper plot shows the two distributions of the Δt for B^0 and $\bar{B}^0$ tagged events decaying to CP=–1 final states. The lower plot is the raw asymmetry between the two distributions as a function of Δt.

Figure 56 shows the decay time difference, Δt, between the two neutral B mesons separately for B^0 and $\overline{B}^0$ tagged decays to the CP=–1 eigenstates. A sample of 88 million $\Upsilon(4S) \to B\overline{B}$ decays were used. The lower plot in Figure 56 shows raw asymmetry in the number of B^0 and $\overline{B}^0$ decaying, $(N_{B^0} - N_{\overline{B}^0})/(N_{B^0} + N_{\overline{B}^0})$, as a function of Δt; a clear CP–asymmetry can be observed. The value of $\sin 2\beta$ extracted from these data is $\sin 2\beta = 0.76 \pm 0.07$, where the error is purely statistical.

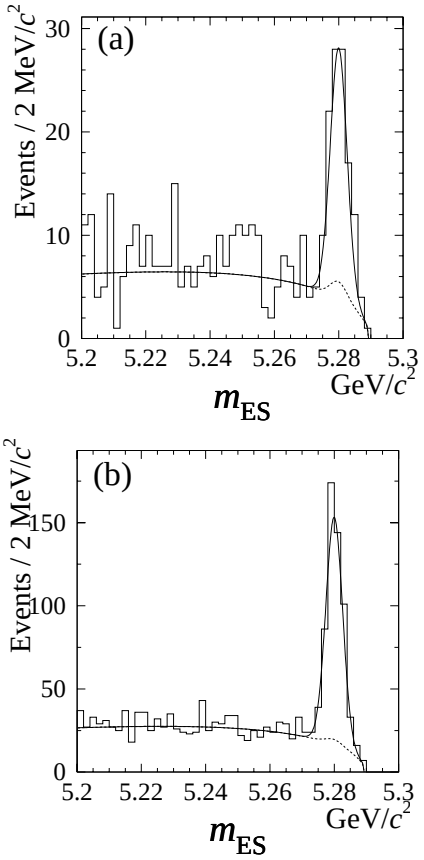

Figure 57. Distributions of m_{ES} for events enhanced in signal (a) $B^0 \to \pi^+\pi^-$ and (b) $B^0 \to K^+\pi^-$ decays. Solid curves represent projections of the maximum likelihood fit, dashed curves represent the sum of $q\bar{q}$ and $\pi\pi \leftrightarrow K\pi$ cross-feed backgrounds.

12.4. Study of $B \to h^+h'^-$ decays

The *CP*-asymmetry in the tree level contribution to the decay $B^0 \to \pi^+\pi^-$ is related to the angle α of the unitarity triangle. However, interference with the $b \to dg$ penguin process leads to a large theoretical uncertainty in the extraction of α from this final state. The theoretical uncertainties can be reduced using an isospin analysis of the $B^0 \to \pi^+\pi^-$, $B^+ \to \pi^+\pi^0$ and $B^0 \to \pi^0\pi^0$ branching fractions [100]. Furthermore, the ratios of B branching fractions to various $\pi\pi$ and πK final states are sensitive to the angle γ of the unitarity triangle. *BABAR* has made measurements of the branching fractions and *CP*-violating asymmetries in $B \to \pi^+\pi^-$, $K^+\pi^-$ and K^+K^- decays [101].

The particles from these two–body decays are in the momentum range $1.75 < p < 4.25$ GeV/c, where there is little discrimination using $\mathrm{d}E/\mathrm{d}x$ for particle identification. In this analysis, the Cherenkov angle measurement provides $\pi - K$ separation, shown in Figure 54, below 5 σ within much of this momentum range. Therefore, to exploit fully the DIRC information, the Cherenkov angle measurement is used on an event-by-event basis in the maximum likelihood fit; this determines the event yields in the three modes simultaneously. The probability density function (PDF) for the Cherenkov angle is constructed from the difference between measured and expected values of θ_c for the pion or kaon hypothesis, normalized by the error, σ_{θ_C}. The parameters of the PDFs are measured in a sample of $D^{*+} \to D^0\pi^+$, $D^0 \to K^-\pi^+$ decays in data.

Figure 57 shows distributions of beam energy substituted mass, m_{ES} [102], for the events enhanced in signal purity by a cut on the probability ratio from the maximum likelihood fit. The fit projections have been corrected for the efficiency of this additional selection. The data shown are selected from 88 million $\Upsilon(4S) \to B\bar{B}$ decays.

12.5. Search for the radiative decays $B \to \rho\gamma$ and $B^0 \to \omega\gamma$

An example of the selection of pions with a high rejection of kaon background is the reconstruction of the rare decays $B \to \rho\gamma$ and $B^0 \to \omega\gamma$ [103]. These decays take place via a $b \to d\gamma$ penguin process. The expected branching fraction for these processes can be modified by the presence of non-Standard Model particles within the penguin loop. The rate of these decays is related to the absolute value of the CKM-matrix element V_{td}, which measures the length of one side of the unitarity triangle.

The $B^0 \to \rho^0\gamma$ final state has a topology identical to $B^0 \to K^{*0}\gamma$ decay, which has a branching fraction approximately 20 times greater than that expected for the signal. Given that the mass difference between the ρ^0 and the K^{*0}

is 122 MeV/c^2, and the width of the ρ is 149 MeV [96], the only means to reject the $B^0 \to K^{*0}\gamma$ background is through the positive identification of pions. The majority of pions from $B^0 \to \rho^0\gamma$ decays have a momentum below 3 GeV/c where the separation between the pion and kaon hypotheses is above 4 σ; with such good pion and kaon separation there is little benefit to adding Cherenkov angle PDFs to the signal yield fit as in the $B^0 \to h^+h'^-$ analysis. Therefore, pions are identified by a cut on the inverse of a kaon selection algorithm, based on likelihood ratios, which was been optimized for pion rejection. To increase the kaon rejection further, consistency between the number of observed and expected photoelectrons in the DIRC is required.

The pion identification efficiency and kaon misidentification rates, as a function of momentum in the laboratory, and the algorithm used in the analysis, are given in Figure 58. The kaon misidentification rate is well below 1 % for much of the momentum range, while a pion selection efficiency around 85 % is maintained.

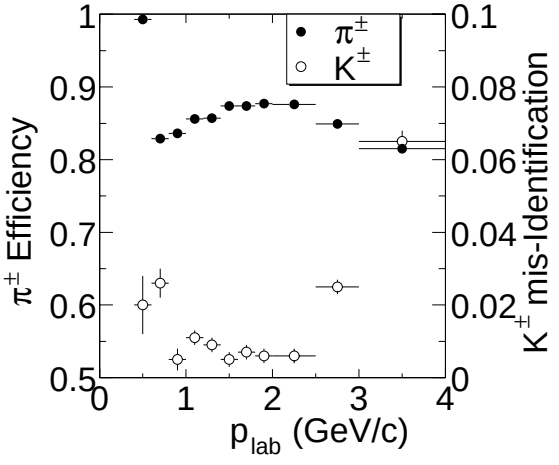

Figure 58. The pion efficiency and kaon misidentification rate, as a function of momentum in the laboratory frame, for the charged pion selection used in the search for $B \to \rho\gamma$ and $B \to \omega\gamma$.

A sample of 84 million $\Upsilon(4S) \to B\bar{B}$ decays is used to obtain upper limits of 1.9×10^{-6} and 1.0×10^{-6}, with 90 % confidence, on the $B \to \rho\gamma$ and $B^0 \to \omega\gamma$ branching fractions, respectively.

13. Conclusion

The DIRC is a novel ring-imaging Cherenkov detector that is very well-matched to the hadronic particle identification requirements of *BABAR*. The detector performance achieved is excellent and close to that predicted by the Monte Carlo simulations. The DIRC is robust, stable, and easy to operate. After more than four years of colliding beam data taking, about 99 % of all PMTs and electronic channels are still operating with nominal performance. Additional shielding in the SOB tunnel region was required to reduce the sensitivity to beam-induced backgrounds. To allow operation at luminosities up to $2 \times 10^{34}/\mathrm{cm}^2\mathrm{sec}$ ($\approx$ 7 times the original PEP-II design luminosity) that may occur during the next few years, faster front-end cards and faster TDCs with deeper buffering have been installed.

14. Acknowledgments

We are grateful to our *BABAR* colleagues for their help and support during the design, fabrication, and operation of the DIRC and to the PEP-II team for providing the excellent luminosity and machine conditions that have allowed this device to demonstrate its capabilities to the fullest. We acknowledge support from the Commissariat à l'Energie Atomique and Institut National de Physique Nucléaire et de Physique des Particules (France), Ministry of Science and Technology of the Russian Federation, the Department of Energy (US), and the National Science Foundation (US). In addition, individual support has been received from the European Community's Human Resources and Mobility Activity. The visiting groups wish to thank SLAC for the support and kind hospitality extended to them.

REFERENCES

1. *BABAR* Collaboration, B. Aubert *et al.,* "The *BABAR* Detector," Nucl. Instr. Methods **A479** (2002) 1 [arXiv:hep-ex/0105044.]
2. "PEP-II: An Asymmetric B Factory, Conceptual Design Report," SLAC-418, LBL-5379, 1993.
3. P.F. Harrison, H.R. Quinn (Eds.), "The *BABAR* Physics Book, Physics at an Asymmetric B Factory," SLAC-R-504, 1998.
4. *BABAR* Collaboration, B. Aubert *et al.,* "Measurement of CP Violating Asymmetries in B^0 Decays to CP eigenstates," Phys. Rev. Lett. **86**, 2515 (2001) [arXiv:hep-ex/0102030.]
5. *BABAR* Collaboration, B. Aubert *et al.,* "Observation of CP Violation in the B^0 Meson System," Phys. Rev. Lett. **87**, 091801 (2001) [arXiv:hep-ex/0107013.]
6. J. Seguinot and T. Ypsilantis, "Evolution of the RICH Technique," Nucl. Instr. Methods **A433** (1999) 1.
7. B. N. Ratcliff, "The DIRC Counter: A Particle Identification Device for the B Factory," SLAC-PUB-5946(1992), and "The DIRC Counter: A New Type of Particle Identification Device for B Factories," SLAC-PUB-6047(1993).
   P. Coyle *et al.,* "The DIRC counter: A New type of Particle Identification Device for B Factories," Nucl. Instr. Methods **A343** (1994) 292.
8. B. N. Ratcliff, "Imaging Rings in Ring Imaging Cherenkov Counters," Nucl. Instr. Methods **A502** (2003) 211.
9. I. Frank and I. Tamm, *Dokl. Akad. Nauk SSSR* **14** (1937) 109.
10. F. A. Jenkins, H. E. White,"Fundamentals of Optics 4th. Ed.," McGraw-Hill, Inc. (1976).
11. J. Cohen-Tanugi, M. C. Convery, B. N. Ratcliff, X. Sarazin, J. Schwiening, J. Va'vra, "Optical Properties of the DIRC Fused Silica Cherenkov Radiator," Nucl. Instr. Methods **A515** (2003) 680 [arXiv:hep-ex/0305001].
12. Boeing Optical Fabrication, 2511 C Broadbend Parkway NE, Albuquerque, New Mexico 87107.
13. "FEA Analysis of the DIRC Structure," MCR Associates, Inc., 111 W. Evelyn Ave, Sunnyvale, CA 94086, 10/15/96.
14. Hysol EA 9359.3, Hysol Aerospace Products, 2850 Willow Pass Road, Pittsburg, CA 94565.
15. Hysol EA 9360 [14].
16. Araldite 2011, Ciba-Geigy, 4917 Dawn Ave., East Lansing, MI 48823.
17. GIROD SISA, 3 rue Saint-Eloi, BP 342, F-73103 Aix-les-Bains, France.
18. E. Antokhin *et al.,* "Simulation and Measurement of the Fringe Field of the 1.5-Tesla *BABAR* Solenoid," Nucl. Instr. Methods **A432** (1999) 24.
19. A.Buzykaev *et al.,* "User Manual for DIRC Magnetic Field Measurement System," DIRC *note*[4] *101* (1998).
20. Vitreosil natural fused silica material and Spectrosil are trademarks of TSL Group PLC, Wallsend, Tyne on Wear, NE28 6DG, England; Sold in the USA by Quartz Products Co., 160 W. Lee Street, Louisville, Kentucky 40201.
21. Heraeus Amersil Inc., 3473 Satellite Blvd. 300, Duluth, Georgia 30136.
22. EPO-TEK 301-2, Epoxy Technology Inc., 14 Fortune Drive, Billerica, MA 01821.
23. Cosmo Optics, Inc., 238 Watking Avenue, Middletown, New York 10940.
24. United Lens Company, Inc., 259 Worcester Street, Southbridge, Massachusetts 01550.
25. Custom Optical Elements, Inc., 51 N. Pecos #105, Las Vegas, Nevada 89101.
26. Zygo Corporation, Laurel Brook Road, Middlefield, Connecticut 06455.
27. *BABAR*-DIRC Collaboration, I. Adam *et al.,* IEEE Trans. Nucl. Sci. **45** (1998) 657 [arXiv:hep-ex/9712001]; *BABAR*-DIRC Collaboration, I. Adam *et al., ibid* 450.
28. For an introduction to the scalar theory for scattering from optical surfaces, see *e.g.,*
    J. M. Elson, H. E. Bennet and J. M. Bennet, "Scattering from Optical Surfaces,"
    in "Applied Optics and Optical Engineering," Vol. VII, edited by Rudolf Kingslake, Robert

[4]For access to DIRC internal notes referenced in this paper, contact: B. Ratcliff, Stanford Linear Accelerator Center, 2575 Sand Hill Road Menlo Park, CA 94025.

R. Shannon and James C. Wyant, Academic Press, 1979.
29. TSL Group PLC, Wallsend, Tyne on Wear, NE28 6DG, England.
30. Ideal Quartz Machining, 17990 Ideal Parkway, Manteca, California 95336.
31. A. Yarritu, S. Spanier, and J. Va'vra, IEEE Trans. Nucl. Sci. **49** (2002) 1704.
32. Scotch Weld DP-190, 3M Industial Specialties Division, St. Paul, MN 55144.
33. Rubbercraft, 15627 S. Broadway Ave, Gardena, CA 90248. The material is EPDM, their type 60 SDH R/C8358/ post cured. The seals were stewed in 80 °C de-ionized water for approximately one month to remove contaminants (the water was frequently replaced until it remained clear).
34. UV curing adhesive, type 63, Norland Products, 695 Joyce Kilmer Ave, New Brunswick, NJ 08901.
35. Hysol 1C-LV [14].
36. Araldite AV 1580 GB and hardner HV 1580 GB, Ciba-Geigy, 4917 Dawn Ave., East Lansing, MI 48823.
37. Electron Tubes Limited, Bury Street, Ruislip, Middlesex HA4 7TA, England. Also, http://www.electron-tubes.co.uk. Electron Tubes Limited was previously known as Thorn-EMI.
38. Ph. Bourgeois, G. Vasseur *et al.,* "Test of Photomultiplier Tubes for the DIRC," DIRC *note 8* (1995).
39. Ph. Bourgeois *et al.,* "Further Measurements of Photomultipler Tubes," DIRC *note 26* (1996).
40. Ph. Bourgeois, G. Vasseur *et al.,* "Systematic Tests of DIRC Phototubes," DIRC *note 105* (1998).
41. Ph. Bourgeois, M. Karolak, J-P. Mouly, "The Light Generator Crate of the DIRC Calibration System," DIRC *note 118* (1999).
42. BP 150 CWB1K-040, LEDtronics, Inc. 23105 Kashiwa Ct, Torrance, CA, 90505.
43. Ph. Bourgeois, G. Vasseur *et al.,* "PMTs in a Magnetic Field: Use of Mu-metal and Effect of a Longitudinal Field," DIRC *note 106* (1998).
44. Ph. Bourgeois, G. Vasseur *et al.,* "Measurements on Photomultiplier Tubes in a Magnetic Field," DIRC *note 53* (1996).
45. "Photomultiplier Tube: Principle to Application," Hamamatsu Photonics K.K. (1994) Cat. No. TOTH9001E01.
46. Ph. Bourgeois, M. Karolak and G. Vasseur, "Effect of Helium on Phototubes," DIRC *note 112* (1998).
47. Ph. Bourgeois and J. Va'vra, "Corrosion of Glass Windows in DIRC PMTs," ICFA Instrumentation Bulletin, SLAC-J-ICFA-22, Spring issue, 2001, http://www.slac.stanford.edu/pubs/icfa/spring01.html.
48. CERN Courier, **42** (2001) 5.
49. S. Mine, K2K experiment, KEK, Japan, private communication.
50. E. Flyckt, private communication. Photonis, Avenue Roger Roncier, Z.I. Beauregard, B.P. 520, 19106 BRIVE Cedex, France.
51. DIRC Electronics Group, "PMT Specifications and EMI 9125," DIRC *note 32*(1996).
52. Saclay Group, "BaBar DIRC Electronics Front-End Chain," DIRC *note 91* (1997).
53. CAEN S.p.A, Via Vetraia, 11 - 55049 Viareggio, Italy.
54. KD Components, Inc. 2151 Challenger Way, Carson City, NV 89706.
55. Longmont Plastic, Inc. 1025 Delaware Ave., Longmont, CO 80501.
56. Ticona, Inc. 90 Morris Ave., Summit, NJ 07901.
57. Mill-Max P/N1053-2-17-15-34-14-02-0. Mill-Max Manufacturing, 190 Pine Holow Road, Oyster Bay, NY 11771.
58. Test Connections, Inc. P/N HPA-74T65. TCI. 1146 W. 9th Street, Upland, CA 91786.
59. ATI Inc. Part Number MicroMin 100 B679 C06.
60. Mill-Max P/N 3603-0-07-15-00-00-08-0.
61. Eccobond 45LV. Emerson & Cuming, Inc. 55 Hayden Ave., Lexington, MA 02173.
62. Circle Circuits, Inc. 307 S. Cleveland Ave., Loveland, CO 80537.
63. Dow Corning 1-2577. Dow Corning Corporation, Midland, MI 48686.
64. Data collection software written in the LabView graphical development environment.

National Instruments Corporation, 11500 N Mopac Expwy Austin, TX 78759-3504.
65. Alpha Wire P/N 5821 Green. Alpha Wire Corp., Elizabeth, NJ 07297.
AWG or American Wire Gauge is also referred to as the "Brown and Sharpe (B & S)" wire gauge. FEP is fluoro ethylene propylene.
66. Rowe Industries P/N RCB10081-2-1. Rowe Industries, Inc., 6225 Benore Rd., Toledo, OH 43612.
67. M. Benkebil *et al.,* "Water Resistant Rhodium Plated Reflectors for Use in the DIRC Babar Cherenkov Detector," Nucl. Instr. Methods **A442** (2000) 364.
68. An amorphous thermoplastic polyetherimide. Manufactured by GE Plastics. http://www.geplastics.com/.
69. ICMC, 75 rue Robert Schuman, Z.I. des Uselles, 77350 Le Mee sur Seince, France.
70. DuPont High Performance Materials, P.O. Box 89, Route 23 South and DuPont Road, Circleville, OH 43113.
71. ATOFINA Chemicals, Inc. 2000 Market Street, Philadelphia, PA. 19103-3222
72. Air Liquide - Balazs Analytical Services, 46409 landing Parkway, Fremont, CA 94538.
73. MC68HC05x32, Motorola Inc., 1301 E. Algonquin Road, Schaumburg, IL 60196, USA.
74. *BABAR* Collaboration, P. Bailly *et al.,* "The Dirc Front-End Electronics Chain For Babar," IEEE Trans. Nucl. Sci. **47**, 2106 (2000); Nucl. Instrum. Meth. A **433**, 450 (1999).
75. A. Ardelean *et al.,* Proc. of the 7th Pisa meeting on advanced detectors. Livorno, Italy, May 1997.
76. P. Bailly, J. Chauveau, J. F. Genat, J. F. Huppert, H. Lebbolo, L. Roos and B. Zhang, "A 16-channel Digital TDC Chip with Internal Buffering and Selective Readout for the DIRC Cherenkov Counter of the *BABAR* Experiment," Nucl. Instr. Methods **A432** (1999) 157 [arXiv:hep-ex/9902015.]
77. Austria Mikro Systeme foundry through Europractice, IC Service Office, IMEC, Kapeldreef 75, B-3001 Leuven, Belgium. Also, http://www.europractice.imec.be.
78. HDMP 1012, HDMP 1014, Agilent Technologies / Hewlett Packard, 395 Page Mill Rd., Palo Alto, CA 94306.
79. Finisar Corporation 1308 Moffett Park Drive Sunnyvale, CA 94089-1133.
80. PALCE22V10H-5JC/5, Vantis/Advanced Micro Devices (AMD), One AMD Place, P.O. Box 3453, Sunnyvale, California 94088-3453.
81. CY7B991-5JC. Cypress Semiconductor, 198 Champion Ct. San Jose, CA 95134.
82. CANbus v1.0, Bosch.
See http://www.canbus.us/.
83. IMP50E10. IMP, Inc., 166 Baypointe Parkway, San Jose, CA 95134-1621.
84. MACH231-7JC, Vantis/Advanced Micro Devices (AMD).
85. PDU16F-0.5. Data Delay Devices, Inc., 3 Mt. Prospect Avenue, Clifton, NJ 07013.
86. L. R. Dalesio *et al.,* "The Experimental Physics and Industrial Control System Architecture: Past, Present, and Future," Nucl. Instr. Methods **A352** (1994) 179. Also, http://www.aps.anl.gov/epics/about.php
87. Wind River, 500 Wind River Way Alameda, CA 94501
88. Objectivity, Inc., 640 West California Avenue Ste. 210, Mountain View, CA 94086-2486, USA.
89. W-IE-NE-R, Plein & Baus GmbH, Mullersbaum 20, D-51399 Burscheid, Germany.
90. T. Sjostrand *et al., Comput. Phys. Commun.* **82** (1994) 74.
91. A. Ryd and D. Lange. http://charm.physics.ucsb.edu/people/lange/EvtGen/
92. The Geant4 Collaboration, "GEANT4: A Simulation Toolkit," Nucl. Instr. Methods **A506** (2003) 250.
93. R. Kalman, "A New Approach to Linear Filtering and Prediction Problems," Trans. ASME – Journal of Basic Engineering, **82D**(1960) 35.
94. J. Va'vra, "Quartz Absolute Internal Reflection Coefficient, Water Transmission, Mirror Reflectivity, Mean Wavelength Response, Mean Refraction Index, and Their Effect on the Expected Number of Photoelectrons and N_0," DIRC *note 129*, April 2000; and "Measurement of EPO-TEK 301-2 Optical Glue

Refraction Index and Reflectivity from EPO-TEK 301-2/Fused Silica Interface," DIRC *note 140*, July 2001; and references therein, see also Nucl. Instr. Methods **A453** (2000) 262.

95. SLD Collaboration, K. Abe *et al.,* "Obtaining Physics Results from the SLD CRID," Nucl. Instr. Methods **A371**, (1996) 195.
96. Particle Data Group, K. Hagiwara *et al.,* Phys.Rev. D**66**, 010001-1 (2002).
97. H. Staengle *et al.,* "Test of a Large Scale Prototype of the DIRC, a Cherenkov Imaging Detector Based on Total Internal Reflection for BaBar at PEP-II," Nucl. Instr. Methods **A397** (1997) 261.
98. *BABAR* Collaboration, B. Aubert *et al.,*"A Study of Time Dependent CP-violating Asymmetries and Flavor Oscillations in Neutral B Decays at the $\Upsilon(4S)$," Phys. Rev. D**66**, 032003 (2002) [arXiv:hep-ex/0201020].
99. *BABAR* Collaboration, B. Aubert *et al.,* "Measurement of the CP-violating Asymmetry Amplitude sin 2β," Phys. Rev. Lett. **89**, 201802 (2002) [arXiv:hep-ex/0207042].
100. M. Gronau and D. London, "Isospin Analysis of CP Asymmetries in B Decays," Phys. Rev. Lett. **65**, 3381, (1990).
101. *BABAR* Collaboration, B. Aubert *et al.,* "Measurements of Branching Fractions and CP-violating Asymmetries in $B^0 \to \pi^+\pi^-$, $K^+\pi^-$, K^+K^- Decays," Phys. Rev. Lett. **89** 281802 (2002) [arXiv:hep-ex/0207055].
102. $m_{ES} = \sqrt{(s/2 + \mathbf{p}_i.\mathbf{p}_B)^2/E_i^2 - \mathbf{p}_B^2}$, where $\sqrt{s}$ is the total center-of-mass energy, $\mathbf{p}_B$ is the momentum of the B candidate, and $(E_i, \mathbf{p}_i)$ is the four-momentum of the initial state. The signal distribution of m_{ES} is a Gaussian centred on the B meson mass. The combinatorial background distribution does not peak and extends down to values well below the B meson mass.
103. *BABAR* Collaboration, B. Aubert *et al.,* "Search for the Radiative Decays $B \to \rho\gamma$ and $B^0 \to \omega\gamma$," Phys. Rev. Lett. **92**, 111801 (2004) [arXiv:hep-ex/0306038.]